Timescale coupling phenomena with hydrodynamic phase field crystal models: The atomic scale shuffle

Duncan Burns, Department of Physics

McGill University, Montreal

August, 2023

A thesis submitted to McGill University in partial fulfillment of the requirements of the degree of Doctor of Philosophy

Doctorate in Physics

Abstract

This thesis is focused on describing phenomena that are emergent from a competition of timescales. The main results are distributed into several chapters, preceded by a generalized introduction. A discussion section follows, which describes the relevancy, interconnections, challenges, and future directions of our contributions.

In chapter 2, we describe an extension to the two time-scale modified phase-field crystal model (MPFC) for the examination of crystal plasticity. Two non-linear density dependent functions are constructed to effectively represent hydrostatic strain and dislocation density. The functions are then used to develop a new MPFC model, which accounts for strain and strain-rate couplings on density dynamics. A short-wavelength dampening is also introduced to account for phonon scattering and thermoelastic dissipation. Finally, a novel semi-implicit numeric scheme for efficient simulations of this model is presented.

In chapter 3, we present an investigation of phonon relaxation of two-dimensional polycrystals. We first measure the phonon spectrum averaged over different polycrystalline configurations, using thermal fluctuations to capture rapid processes. It is shown that polycrystals have a phonon caging regime, a signature of amorphous materials. Subsequently, we report on a mechanism of grain-boundary melting resulting from the accumulation of phonon scattering. We find this behaviour exhibited in both rapid temperature annealing of polycrystalline samples and from input of kinetic energy representative of rapid laser heating or hot-rolling. In the latter case, we theorize a rate relation for the maximally achieved liquid fraction as a function of the initial kinetic energy, defining a metastable activation energy that can be measured in experiments. We expect that the scattering mechanisms investigated underpin grain-boundary melting and recrystallization

processes encountered in rapid solidification experiments.

In chapter 4, a new temperature field crystal (TFC) framework is developed, which permits the study of coupled density, vacancy and temperature field dynamics at the length scale of atomic ordering. Following a derivation of the new thermo-density coupled MPFC model, several physical properties of the model are demonstrated. We reproduce the thermo-density interface profiles encountered in the steady state solidification growth limit. We further illustrate the existence of a vacancy concentration inherent in the phase field crystal amplitude. We illustrate that in the isochoric limit of the TFC model, it incorporates effects of thermal expansion through the change of amplitude with respect to temperature, rather than by increasing the equilibrium lattice length. The model is then applied to the study of select solidification processes. It is shown that the release of latent heat during recalescence is accompanied by a change in the average thermal pressure. Moreover, we illustrate that modulations of the recalescence curve can be indicative of plastic deformation, dislocation activity, and phonon scattering. Notably, the temperature evolution may be used as a marker for the grain distribution attained following grain impingement.

The linear hydrodynamic extensions to the phase field crystal models may be utilized to provide clues and mechanisms that result from the continual transport of energy. Our studies illustrate the difficulty in studying structural transformations due to the many competing time scales. Our work highlights that time scale competition can give rise to numerous mechanisms that lie at the heart of a significant number of challenges in current material processing. We infer from our investigations that the focus for this class of behaviours is tied to shuffle of innumerable atoms, which communicate through energy interchange.

Abrégé

Cette thèse explore les phénomènes émergents résultant de la compétition entre échelles de temps. Les principales découvertes sont présentées dans des chapitres suivant une introduction générale. Une section de discussion met en évidence la pertinence, les interconnexions, les défis et les orientations futures.

Le chapitre 2 étend le modèle cristallin en champ de phase modifié (MPFC) pour étudier la plasticité cristalline sur deux échelles de temps. Des fonctions non linéaires dépendantes de la densité modélisent la déformation et les dislocations. Cela conduit à un nouveau modèle MPFC tenant compte du couplage de la déformation et des effets de vitesse sur la dynamique de la densité, incorporant un amortissement à courte longueur d'onde pour la diffusion des phonons et la dissipation thermoélastique.

Le chapitre 3 explore la relaxation des phonons dans les polycristaux bidimensionnels, capturant les processus rapides via des fluctuations thermiques. Les polycristaux présentent un régime de cage de phonons, similaire aux matériaux amorphes. Un mécanisme de fusion intergranulaire est observé lors du recuit thermique rapide et de l'apport énergétique.

Le chapitre 4 introduit le cadre cristallin couplé champ de température (TFC) pour la densité à l'échelle atomique, les lacunes et la dynamique de la température. Les propriétés du modèle incluent les profils d'interface lors de la solidification et la concentration inhérente de lacunes. Le modèle TFC intègre les effets de dilatation thermique via un changement d'amplitude. Il est appliqué à l'étude de la solidification, révélant les impacts du dégagement de chaleur latente et les modulations des courbes de recalescence indiquant la déformation plastique, l'activité de dislocation et la diffusion des phonons.

Les extensions hydrodynamiques linéaires des modèles cristallins en champ de phase fournissent des aperçus sur le transport continu de l'énergie, soulignant les défis liés aux échelles de temps concurrentes. En résumé, ce travail met en évidence divers mécanismes au cœur des défis liés au traitement des matériaux, en mettant l'accent sur les interactions entre les atomes et les échanges d'énergie.

Acknowledgements

A dissertation represents a monumental achievement on expression of physical understanding. Through verbalization we are painting our envisioned landscape within a broader collage. Just as long time behaviours can be influenced by short instances, our perceptions of the world evolve analogously. It is thus a challenging feat to appropriately thank all the people (and furry critters), that have molded my perspective.

I begin with a most heartfelt expression of thanks to my supervisors Prof. Martin Grant and Prof. Nikolas Provatas. Both have shown me enormous support, by providing me with their time, guidance, and encouragement, despite the many demands of their own. Their willingness to hear many crazy, unhoned ideas with non-judgemental feedback has been invaluable. I am immensely appreciative of the encouragement, humor, and patience that they have given me, which has subsequently allowed me to overcome hurdles and thoroughly enjoy the roller-coaster that is life.

Additional thanks is necessary to the graduate students, post-docs, and former students I have had the pleasure of meeting along my journey: Prof. Fallah, Prof. Ofori-Opoku, Prof. Greenwood, Niloufar, Yoni, Alex, Paul, Salvador, Daniel, Matt, Sam, Damien, Jaarli, and Rebecca. I am in continual amazement at all of your abilities, advice, encouragement. It has been my serendipity at having the opportunity to learn and grow by hearing your perspectives, in the form of ideas, humor, and fanatical banter.

I send further appreciation and thanks to the numerable fantastic professors at McGill University and University of New Brunswick. In particular, I would like to thank Prof. Mark Sutton, Prof. Bradley Siwick, Prof. Dominic Ryan, Prof. Hong Guo, Prof. David Cooke, and Prof. Mohsen Mohammadi, all of whom have shared their time with me in many stimulating discussions. Fur-

thermore, I thank others in the Physics Department that have aided me throughout my studies: Diane Koziol, Louise Decelles, and Lauren Kay.

To my family: Mom, Dad, and Ichi, thank you so much for believing in me, letting me craft my own story, and sail across the stars. Just your voice alone has encouraged me in the completion of this manuscript. It is only through your constant unwavering support that I have been able to live life in constant amazement at the world around. Isabelle, thank you for your continued support and understanding, even when life can get you down. Your trust and faith in me can always bring a smile and home to my weary soul.

Lastly, I thank you, the readers of this thesis, for your attempt at delving into my painting and my journey.

This research was additionally supported by funding from the Natural Sciences and Engineering Research Council of Canada (NSERC), and computing resources provided by the Digital Alliance of Canada.

Statement of Originality

The original contributions intrinsic to this thesis are captured in chapters 2-4. I certify that the contents described herein are results of my own work. Supervision of the projects was provided by Prof. Martin Grant and Prof. Nikolas Provatas. Chapter 2 is as published in Ref. [1]. I constructed the mathematical formulations. I further wrote the numeric algorithm and performed the simulations. I wrote the manuscript and my supervisors, Prof. Martin Grant and Prof. Nikolas Provatas, helped with editing. Chapter 3 is as published in Ref. [2]. I constructed the mathematical formulations. I further wrote the numeric algorithm and performed the simulations. I wrote the manuscript and my supervisors, Prof. Martin Grant and Prof. Nikolas Provatas, helped with editing. Chapter 4 is as submitted to *Physical Review Materials*. I constructed the mathematical formulations. I further wrote the numerical algorithm and performed the simulations. I wrote the manuscript and my supervisors, Prof. Martin Grant and Prof. Nikolas Provatas, helped with editing.

Table of Contents

List of Figures

List of Tables

Chapter 1

Introduction

Innovation is driven by a desire to utilize the technology available. At times, the knowledge may seem arcane and empirical measurements guide subsequent progress. These incremental achievements slowly unlock mysteries and allow civilizations to evolve. However as novel approaches and techniques are brought to light, new unanswerable questions remain. Such is the spiral of technological progress that I see and the years of confusion that it has brought me; seeming to always be brought back into the play.

The fabrication of metals and alloys is an example of this dynamic. The fruits of which have churned industry for thousands of years, progressively allowing access to more applications. Many forms of metals exist, often hard, brittle, or malleable and ductile. When heated to extreme temperatures, their properties change, like the rare structured snowflake which lands on your hand only to melt away in shapeless form. Harnessing the molten-liquid behaviour, has allowed metals to be cast into the stereotypical tool. Ages past, such tools had a proclivity to fracture; potentially caused by subtle changes in the environment, at a scale locked by their technology. Great artisans, could detect these minute fluctuations by listening to the shadows dancing on their molten work. Just as a stew's flavour is developed, blacksmiths would add flux and other ingredients to enhance desired material properties. The incorporation of coal into iron during the industrial revolution is marked as a societal shift, whence steel could be harnessed to support infrastructure (buildings, skyscrapers, trains, and more). Yet when a bridge, or aircraft break, we ask the question: "What

are the fundamental causes of such a response and how can we exploit it to enhance the world we live in?".

In this thesis I aim to explore the layered perception of the solid-liquid transition. In particular, how for example, from the addition of flux, a class of physical phenomena emerge. As the time and length scales of energy transportation become coupled, a vast set of interactions and physical consequences may ensue. Our work here is by no means exhaustive, just the tip of an iceberg. As we depart on our grand adventure, we first return to past understanding, which will serve as our guide through rabbit holes of unknown depths.

1.1 Thermodynamics

A paradigm of investigation began with attempt to catalogue properties associated with a given material. At work beyond our visibility, is the dance of innumerable atoms with typical scales on the order of 10^{-10} m. Motions of the atoms then define their collective state and phase. When subjected to external stimuli, such as temperature or pressure, the behaviours characteristic to that material may alter. In a sense, the responding material may be viewed as transitioning between one state to another. In certain situations, the state properties vary drastically, *e.g.* the structured ice cube becoming formless upon heating. Regimes where material response is uniform are subsequently denoted as thermodynamic phases. To exploit a given phase throughout its state space and understand how a material would respond, guiding equations of state are developed. Conventional phases include gases, liquids, and solids. What differentiates these class of phases is the dominate interaction length scales. In gases, atoms meander, remaining unimpeded for large distances (typical scale 10^{-7} m) relative to their size. Meanwhile in liquids, the typical mean free path is of order 10^{-9} m. This approaches the scale of individual atoms. Nonetheless, they remain free to explore, veering around short range interactions. As the length scale further approaches the interaction scale, atoms become bound together in ordered lattices, solids. We note that the interactions can have certain favourable orientations. Thus many types of solids exist with differing lattice structures. The confining movement of atoms is not only an indicator of phase, but also a

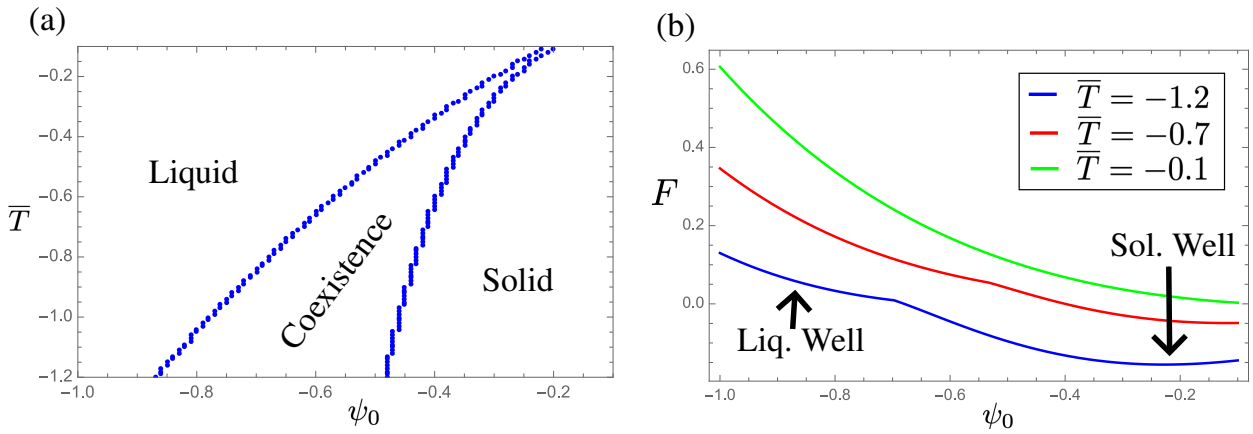

Figure 1.1: (a) Illustrated is an example phase field crystal phase diagram between liquid and solid. $\overline{T}$ denotes an effective dimensionless temperature, while ψ_0 denotes the dimensionless density deviation from a reference value. (b) Illustrates the free energy landscape, and the gradual increase in solid well upon increasing temperature.

cause for the substantial difference in material properties. We tabulate the preferred phase through phase diagrams, such as that presented in subpanel (a) of figure 1.1. The lines indicate threshold boundaries across which, a phase transformation may ensue. Specific to first-order transitions, like solid-liquid, a density jump occurs accompanied by a loss of long-range structural symmetry. In subpanel (b) of figure 1.1, a solid-liquid energy landscape is demonstrated. The energy minima may be viewed as the equilibrium states to which we assign pressures and temperatures. Given enough energy to explore phase space, the system will tend towards the global minimizing state.

It has been the attempt for many decades to make a set of governing equation that describe the state of a given phase. That is to say, what the temperature, pressure, and volume are at any given point on figure 1.1. A classic example of gaseous equations of state is the ideal gas law, where no interactions are assumed. Weak incorporation of the interaction effects has led to more generalized variants [3, 4], which can be applied to the liquid-state. Solids meanwhile can be intimidating, and thermodynamic descriptors are generally found by treating the lattice as woven together with dash-pots and springs [5]. The Mie-Gruneisen equation of state encircles another class of solid-state theories [6–8]. Here the emphasize is on making connection of the macroscopic variables through the phonon dispersion spectrum. The use of solid-state equations has lied predominantly

in describing high pressure environments such as tectonic plate shifts [8–10]. However, the atomic interactions act over short distances, synonymous with a high pressure. This allows application to not only rheology, but also the metallic alloys in aircraft. These models constitute the basis for widely utilized thermodynamic databases [11, 12].

1.2 Kinetic theory

In many cases, we need to wait infinitely long for a material to explore its phase space. Only upon skiing down numerous energy barriers will the material reach an energy minimizing state. This journey can lead to undesirable material characteristics, like fracture or metastable phases. Alternatively, the system can become frustrated, perhaps in the writing of a thesis, trapped in a local minimum configuration. Thus it is imperative to understand the pathway followed. In particular, it is important to consider the modes of energy transport, with which the system can relax.

The interaction picture style of study is tantamount to molecular dynamics (MD) methods, which have a widespread use in literature [13–16]. The focus is on propagation of the position ($\overrightarrow{r}_i$) and momentum ($\overrightarrow{g}_i$) of every particle of mass m_i through,

$$\frac{\partial \overrightarrow{\chi}}{\partial t} = \left[\overrightarrow{\chi}, H\right]_{\text{Poisson}}, \tag{1.1}$$

which is the Poisson bracket formulation of Newtonian mechanics. This form is written in terms of a vector $\overrightarrow{\chi} = \langle \overrightarrow{r}_i, \overrightarrow{g}_i \rangle$, propelled by Hamiltonian, $H = \sum_i \left(\frac{|\overrightarrow{g}_i|}{2m_i}\right) + \sum_{i,j} \left(V_{i,j}\right)$, where $V_{i,j}$ are individual atomic interactions. Here interaction potentials are posited from both on quantum mechanical measurements [17], and emergent behaviours [18]. Molecular dynamics has seen use in studying biological polymers [14], solid-state fluctuations [15] and dislocation evolution [16] to name a few. The simulations technique allows access to fine scale transients, hence the plethora of behaviour cataloging. As we have argued, the properties characterizing a material are a result of the collective response of fine scale interactions. As a consequence, there has been substantial investment in simulating the complete interatomic potential for large numbers of atoms. However,

a rough estimate of the number atoms in a cubic meter of aluminum is on the order of 10^{28} atoms. Thus explicit atomic tracking for macroscale phenomena becomes intractable. Recent efforts in the theoretical framework direction have been on bridging scales to allow for larger studies [19].

To compensate, coarse-grained theories (Langevin, Fokker-Planck, ...) emerged [20]. Herein symmetry variables, order parameters, (conservation laws, orientation symmetries, ...) set the fundamental time and length scales. This permits study of emergent phenomena associated with a particular symmetry, or energy mode. A connection to the interaction picture, can be found through projection operator formalism, pioneered by Zwanzig [21] and Mori [22]. The essence of this technique is a separation of rapid fluctuations from the symmetry variables associated to the system. By projection onto the plane of slow variables, we can arrive at a memory function recasting of Eq. 1.1,

$$\frac{\partial\overline{\chi(t)}}{\partial t} = i\Omega\overline{\chi(t)} + \int_0^t dt' \Big(\langle f(0) f(t-t') \rangle \overline{\chi(t')} \Big) + f(t). \tag{1.2}$$

Here $\overline{\chi(t)}$ describes the set of slow modes and Ω denotes the frequency matrix thereto associated. Meanwhile, $f(t)$ represents the rapid noise fluctuations, and $\langle f(0) f(t-t') \rangle$ is a memory kernel of the interaction between rapid and slow variables. Eq. 1.2 is formally exact to Eq. 1.1. The main postulate arises in the form of the memory kernel and statistics of $f(t)$. For simplicity one often assumes a self-averaging background, $\langle f \rangle = 0$, and $\langle f(t) f(t') \rangle = 2D\delta(t-t')$, where D is diffusion operator. Reexpanding the memory Eq. 1.2 results in,

$$\frac{\partial\overline{\chi(t)}}{\partial t} = -D\Big[\overline{\chi(t)}\Big] + f(t). \tag{1.3}$$

Thus we have arrived at a coarse-grained description of our complex system. More complex non-linear forms can be arrived at through additional constraints and alternative noise statistics. For what follows we shall consider mainly the macroscale density field, thus the association of $\overline{\chi(t)}$ with $\rho(r,t)$. With Eq. 1.3, the study of emergent phenomena for our hypothetical cubic meter of aluminum can be analyzed. In summary, the coarse-grained theories should be considered fundamental to a scale set by the scale separation.

1.3 Hydrodynamic Formalism

The framework provided by Eq. 1.3 sets the basis for more complex multi-component theories [23–27], such as hydrodynamics. When applied to large scale phenomena the additional fluctuations from $f(t)$ are assumed negligible. It is within this concept that I believe Boon and Yip were amazed by the potential of hydrodynamic approaches to study molecular liquids [28]. For this application, conservation laws associated with symmetry variables enter in the form,

$$\frac{\partial \chi}{\partial t} = -\nabla \cdot J_{\chi}, \tag{1.4}$$

where J_{χ} represents the current associated with field χ, flowing through a local volume element. In this sense, the conservation evolution equation is local. However, we note that in biological systems, the mixture of scales and energy modes often requires non-localized variants [29]. Additional advection terms may be added, as is necessary in description of weather patterns. We are most interested in linear classical solid-liquid hydrodynamics description for which thermodynamic consistency relations are employed to express the current.

So to begin, we list the symmetry variables associated with our solid-liquid system. Since mass cannot be created nor destroyed at the energy scales pertinent to this work, the density, ρ must be a conserved quantity. In addition, for a reversible process, energy, E, and momentum, g, are conserved as required by Noether's theorem in accordance with spatial and time reversal invariance. The five modes described by ρ, E, and g constitute a minimal description of liquids. As in the case of the anti-ferromagnet, order parameters associated with the continuously broken symmetry need be additionally introduced. Hence for crystals, we must add an additional equation for the global spatial symmetry in the form of a lattice. The relevant variables are distortions of the lattice denoted by $\delta\overrightarrow{x}$ which carry energy as they propagate through the solid. These propagation are often denoted as phonons. This consideration adds an extra three modes in the description of solids. We note that the phonons motion can be viewed as conserved when interpreted in terms of strain, $\delta u_{i,j} = \frac{-1}{2}\left(\frac{\partial x_i}{\partial r_j} + \frac{\partial x_j}{\partial r_i}\right)$. We further highlight that certain phonon oscillations are known to propagated in the liquid phase, but dampen out rapidly [30, 31]. In this context, we note that there

exists other classes of phases, such as liquid crystals that require only parts of the strain tensor. (*i.e.* nematics and smectics) [24]. In summary, solids and liquids may be described through,

$$\frac{\partial \rho}{\partial t} = -\nabla \cdot g, \tag{1.5a}$$

$$\frac{\partial g}{\partial t} = -\nabla \cdot \sigma, \tag{1.5b}$$

$$\frac{\partial \varepsilon}{\partial t} = -\nabla \cdot q, \tag{1.5c}$$

and

$$\frac{\partial \overleftrightarrow{u}}{\partial t} = -\nabla \cdot J_u, \tag{1.5d}$$

where it remains to interpret the currents.

We turn our attention to the first and second laws of thermodynamics to understand how Eqs. 1.5 relate to different transportation modes. Namely, how the energy is decomposed, and that no work may be extracted from a reversible process. It is customary to posit the solid thermodynamics,

$$\mathrm{d}\varepsilon = T\mathrm{d}(\rho s) + \mu \mathrm{d}\rho + v\mathrm{d}g + ..., \tag{1.6}$$

which relates energy fluctuations ($\mathrm{d}\varepsilon$) to entropic energy ($T\mathrm{d}(\rho s)$), chemical energy ($\mu \mathrm{d}\rho$), kinetic energy ($v\mathrm{d}g$), and other forms. We note that s stands for the entropy density, while μ, the chemical potential which are interrelated via the Legendre transformation definition,

$$F = \varepsilon - T\rho s = -P + \mu\rho. \tag{1.7}$$

This relation arises from the Legendre transformation definition between the grand potential, $\mathscr{G}$ and energy, E.

The intensive quantities of the theory are coupled through the Gibbs-Duhem closing relation,

$$\rho \mathrm{d}\mu = -\rho s \mathrm{d}T + \mathrm{d}P - g \cdot \mathrm{d}v + ... \tag{1.8}$$

Subsequently by the second law of thermodynamics, we require,

$$T\frac{\mathrm{d}}{\mathrm{d}t}\int dr\Big(\rho s\Big)=0, \tag{1.9}$$

for any reversible process. When integrating Eq. 1.9 by parts and substitution of Eqs. 1.5-1.8, we may relate current densities to gradients of our variables. To maintain analyticity, it is standard to only consider the linear contributions. Non-linear additions, such as advection can tacitly added in accordance with experimental observation.

1.4 Experimental Connection

When exploring the murky depths, it is important we not lose sight of reality. The theories that we have described are only validated by direct evidence. We shall mention in passing some direct connections between experimental measurements and correlations determinable from the coarse-grained theories, such as Eq. 1.3. Although we mention this in passing, a more complete picture may be garnered from scattering theory, describe in texts such as [28], or [32].

The main observable in scattering theories are correlation functions, similarities at different spatial and/or temporal points. In the context of density fields, we denote $C_{\rho,\rho}=\langle\rho(r,t)\rho(r',t')\rangle$ the density correlation function. Here $\langle\cdot\rangle$ represents the thermal average associated with rapid fluctuations. As we shall see, $C_{\rho,\rho}$ can be imaged through coherent neutron scattering. Meanwhile, the self-correlation, $S_{self}=\langle\rho(r,t)\rho(r,t')\rangle$, provides information about the self-similarity in time. This metric is the focus of incoherent neutron scattering experiments.

First it necessary to mention that thermal noise fluctuations captured by $f(t)$ are readily detectable with measured statistics. Perhaps one of the most famous examples is in regards to Brownian motion. It was shown that a scalar constant noise diffusion, D, can be connected with the velocity and the mobility, $\mathscr{M}$, of macroscopic pollen grains. This fluctuation-dissipation association was later expounded upon by Kubo through interrelating real and imaginary components of

susceptibilities [33]. The tenants follow from,

$$\mathscr{M} k_b T \equiv \int_0^\infty dt \Big(\langle \overline{\chi(0)\chi(t)} \rangle e^{-i\omega t} \Big) = \int_0^\infty dt \Big(\langle f(0) f(t) \rangle e^{-i\omega t} \Big) \approx D, \tag{1.10}$$

where the fluctuation memory is directly connected to the correlations of $\mathscr{F}[\chi(t)]$.

Particular to scattering or diffraction experiments, the resultant spread of energy is focus. A metric for which, is the differential cross section, $\frac{\mathrm{d}^2\sigma}{\mathrm{d}\Omega \mathrm{d}E'}$, measured for incident wavevector, k',

$$\frac{\mathrm{d}^2\sigma}{\mathrm{d}\Omega \mathrm{d}E'} = \frac{k'}{2\pi\hbar k} \int dt \Big(e^{i\omega(t-t')} \langle \sum_{a,a'} \big[b_a b_{a'} e^{ik(x'-x)} \big] \rangle \Big). \tag{1.11}$$

This form adopts the notation of Chaikin and Lubensky [32], where b_a ($b_{a'}$) is the magnitude of interaction potential associated with particle a (a'). Further simplification can be made by decomposition of the sum into coherent ($a = a'$) and incoherent ($a \neq a'$) components. In turn this provides a connection between the statistical density correlations and the two scattering types:

$$\frac{d^2\sigma}{d\Omega dE'}\Big|_{\text{coherent}} \propto C_{nn}(k,\omega), \tag{1.12}$$

and

$$\frac{d^2\sigma}{d\Omega dE'}\Big|_{\text{incoherent}} \propto S_{\text{self}}(k,\omega). \tag{1.13}$$

In essence, we have illustrated the correlations represent fundamental metrics to compare out-of-equilibrium theories to experiments. We have presented in figure 1.2 subpanel (a) an example time and length scale map of commonly used measurements techniques. Scales larger than illustrated are fundamental to astrophysics. Meanwhile smaller scales are focus to quantum mechanical phenomena. Subpanel (b) of the same figure additionally illustrates some model techniques that can be used at different scales. Increase in scattering power, and scale allows us to make observation beyond our inherent vision. In turn, this permits further construction of theoretical frameworks.

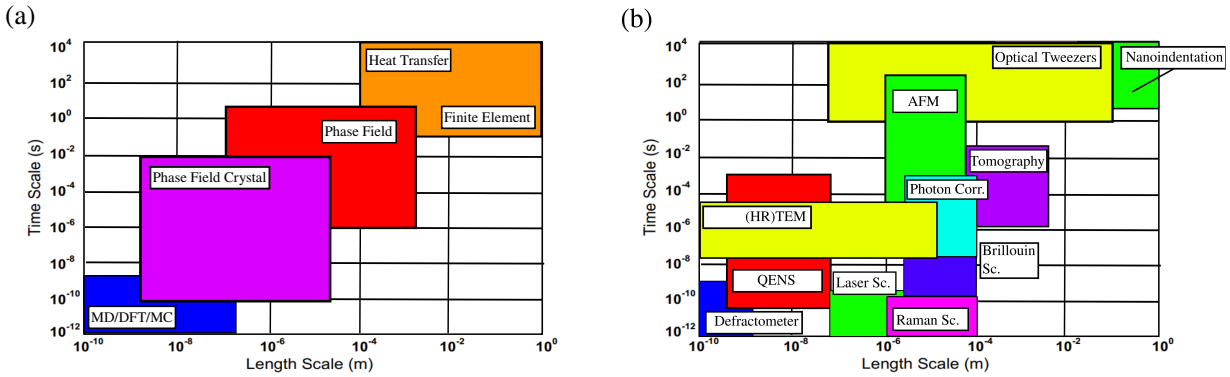

Figure 1.2: Illustrated are typical time and length scale regimes for common simulation techniques (subpanel (a)) and experimental methods (subpanel (b)). Scales ranges from nanoscale to mesoscopic systems.

1.5 Phase Field Crystal

The reduction of time and length scales is particularly relevant for the study of solidification. One example of the reason is the impact that short time fluctuations and atomistic defects can have on the global microstructure. There have been numerous attempts at describing the complete interaction picture of the growth process. However, as we have argued, coarse-grained theories can be used to overcome computational constraints of N-body simulations. Fundamental to a new scale, coarse-grained theories can still provide analysis of emergent topological and interface instabilities. Phase field models propagate an order parameter, in accordance with the symmetry. The order parameter is then driven by thermodynamic gradients as in hydrodynamics to recover expected correlation temporal scaling [34]. These methods, allow study of species transport through and across an interface. At the cost however, of specifying interface fluctuation depths and interface anisotropy, inherent to the vibration and preferred orientation of the atoms. Provided sufficient constraints in a given range of parameter space, phase field methods can be used to probe interface instabilities, *e.g.* Taylor-Saffman [35], Mullins-Sekerka [36], and Asaro-Tiller-Grinfeld [37, 38] to name a few. At the scale of the lattice structure, phase field crystal methods have been widely applied [39], at the cost of shorter and smaller simulations. The scale naturally incorporates topologic instabilities, like dislocations. As we shall show as one result of my work, vacancy

concentrations are buried in the formalism. The scale of plasticity opens a rich wonderland of dislocation interactions and structures.

The phase field crystal construction took inspiration from phase field models. Herein a time averaged continuum density field, ρ, is considered the relevant order parameter for solidification. As we shall see, this follows because the ρ can be viewed as obtaining a spatial symmetry upon solidification. The diffusive evolution of ρ is driven by gradients of the free energy, such as the chemical potential $\mu = \frac{\delta F}{\delta \rho}$. So, it is important to determine a minimal description of the chemical potential in terms ρ. This will require approximation, since in general μ can be a highly complex functional.

1.5.1 Classical Density Functional Theory Derivation

The classic method followed by Elder *et al.* in construction of the phase field crystal free energy lies in reference to classical density functional theory [20]. In the work Ramakrishnan *et al.*, expansion of the free energy around the liquidus, allowed connection to the density field for freezing [40]. This approach is expounded upon by the reviews of Evans [41] and Singh [42]. The starting point is the separation of the free energy, $F = F_{\text{ideal}} + F_{\text{interaction}} + F_{\text{external}}$, into non-interacting, interaction, and external contributions.

The ideal gas component is readily obtainable by considering the statistics of non-interacting particles. It follows,

$$F_{\text{ideal}} = k_b T \int dr \Big(\rho \big[\log(\Lambda \rho) - 1 \big] \Big) \tag{1.14}$$

where $\Lambda = (\frac{2\pi\hbar^2}{m k_b T})^{3/2}$ is the thermal de Broglie wavelength. One often writes $\rho = \rho_{\text{reference}}(1+\psi)$, to express fluctuations of the density away from a reference by the dimensionless parameter ψ. Due to the computational complexities associated with logarithms, small perturbations of ψ are considered. In this limiting case, the ideal energy can be expanded,

$$F_{\text{ideal}} = F_{\text{ideal}}[\rho_{\text{reference}}] + k_b T \rho_{\text{reference}} \int dr \Big(\psi \log(\Lambda \rho_{\text{reference}}) + \frac{\psi^2}{2} - \frac{\psi^3}{6} + \frac{\psi^4}{12} + ... \Big). \tag{1.15}$$

The minimal expansion necessary to capture a free energy well associated with the idealized state

consists of truncating the expansion at $\mathscr{O}(\psi^4)$. The minimal truncation has proven resilient in describing a uniform density phase energy minimum, but has challenges when large density jumps are considered [43].

Just as an apple falls under gravitational attraction, a monolayer of graphene can be influenced by sandwiching layers. In this way, energy may enter the statistics of an isolated system in terms of an external potential energy, $V_{\text{reference}}$. In terms of a free energy,

$$F_{\text{external}} = k_b T \rho_{\text{reference}} \int dr \Big((1+\psi) V_{\text{external}} \Big), \tag{1.16}$$

Often the external potential is assumed vanishing. In such cases, we consider a fully isolated system. We note that with appropriate choice of V_{external}, this may be a means to induce stress onto a system.

The final energy ingredient is associated to interactions. Following a functional series expansion of the interaction energy,

$$F_{\text{interaction}} = F_{\text{interaction}}[\rho_{\text{reference}}] + \sum_{n=1}^{\infty} \frac{1}{n} \int \prod_{i=1}^{n} [\mathrm{d}r_i \delta\rho(r_i)] \Big(\frac{\delta^n F_{\text{interaction}}}{\prod_j^n [\delta\rho(r_j)]} \Big). \tag{1.17}$$

Following the description of Evans, the interaction energy may be viewed as the generating functional of the n-point correlation function [41]. Thus it follows that,

$$C_n(|r_1 - r_2|, |r_1 - r_3|, ...) = -(k_b T)^{-1} \frac{\delta^n F_{\text{interaction}}}{\prod_j^n [\delta\rho(r_j)]}, \tag{1.18}$$

written in terms of separation distance, $|r_i - r_j|$, due to spatial reflection and isotropy symmetry requirements. We note that the zeroth and first order term enter as constants, with a latter the result of translational invariance. Ramakrishnan *et al.* demonstrated that the two-point correlation function was the minimal ingredient necessary to describe the freezing transition for a number of materials with simple crystal structures [40]. As a result of the expansion around the liquid density, the higher order correlations become necessary to describe the material deep within the solid phase. The Taylor series expansion methodology represents only one method to approximate

the interaction energies.

Combining the free energies components discussed thus far yields,

$$F = F_0 + k_b T \rho_{\text{reference}} \int dr \Big(\psi \log(\Lambda \rho_{\text{reference}}) + \frac{\psi^2}{2} - \frac{\psi^3}{6} + \frac{\psi^4}{12} - \frac{\psi}{2} C_2 * \psi \Big). \tag{1.19}$$

This equation thus represents the minimal description of solidification statistics, where $*$ represents the correlation operation.

Further assumption is necessary, since the two-point correlation is not a simple function. Short-range features can be captured through postulated forms such as Percus-Yevick [44] or Tarazona [45]. Recent progress in density functional theory has been in fundamental measure theory, in which an interaction scale expansion of the correlation is used [46]. Phase field crystal models adopt a long-range perspective, building a polynomial representation of the Fourier space correlation,

$$\mathscr{F}_k[C_2] = (1 - B_l + 2B_x k^2 - B_x k^4). \tag{1.20}$$

As we shall see, the parameters B_l and B_x can be fit to the first peak of the static liquid state structure. Oettle *et al.* showed that Eq. 1.20 was sufficient in capturing the ordering transition, but required additional smoothing to connect with real space density functional theory correlations [47]. Higher order polynomials have been developed to describe more complex crystal geometries [48–51]. Alternatively, structural phase field crystal correlation function exists that introduce Gaussians centered at the lattice wavevector magnitude [52].

The correlation in Eq. 1.20 permits the coexistence of an ordered and disorder phase. Depending on the value of B_l and B_x, a certain phase may dominate the system. In figure 1.3 subpanel (a), we have provided an example image of the density field, for the faceted growth of the solid phase. Subpanel (b) shows the one-dimensional line profile of subpanel (a) cut along the indicated red line. As illustrated in the solid phase, atoms are treated as coarse-grained around their local lattice site positions. Meanwhile, the liquid phase is assumed uniform, where coarse-graining removes any liquid-state structure.

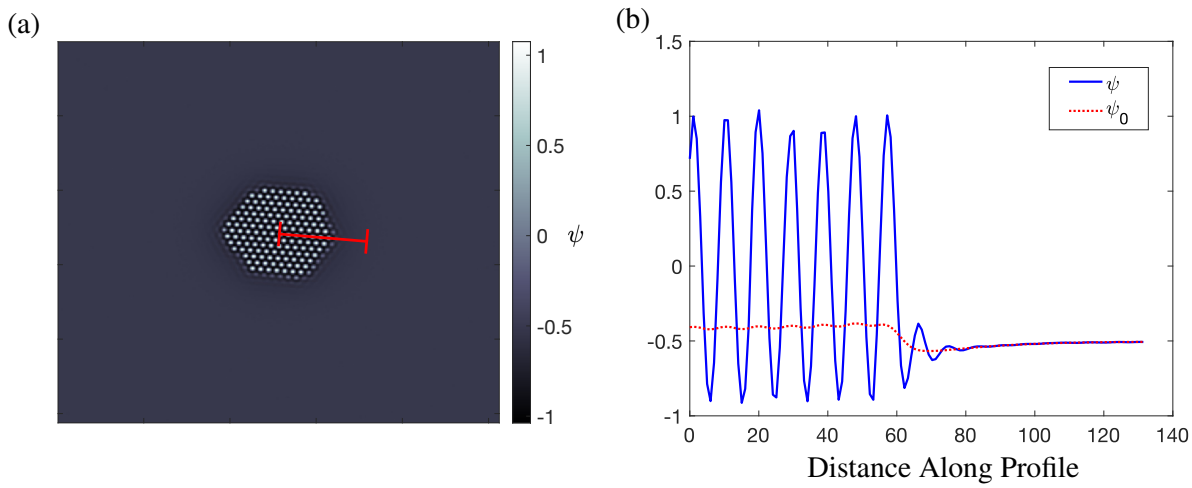

Figure 1.3: An example faceted solidification simulation is provided in subpanel (a). The associated red line cuts the density profile shown in subpanel (b). By averaging over a unit cell, the average density can be obtained. This has been superimposed onto the line profile in subpanel (b). A density jump shown is characteristic of the first order transition.

1.5.2 Thermodynamics

The form of the free energy appearing in Eq. 1.19 can now be interpreted in terms of the macroscopic variables discussed earlier. To understand the phase energetics, it customary to make the mode-expansion ansatz. In doing so,

$$\rho(r) = \overline{\rho} + \Sigma_{G_j} A_{|G_j|} e^{iG_j \cdot r}, \tag{1.21}$$

where the sum is over reciprocal lattice vectors, G_j. The parameter $\overline{\rho} = \rho_{\text{ref}}(1+\psi_0)$ represents the uniform average density adopted by the system. The liquid phase is preferred when $A_{G_j} = 0$ minimizes the free energy. Meanwhile, the ordered phase is the equilibrium configuration when the minimizing amplitude is non-zero.

We note the existence of additional lower dimensional phases such as the stripe phases. The different phase energetics can be found through substitution of Eq. 1.21 into the free energy in 1.19. Subsequent integration over a unit cell will approximate the bulk phase free energies. Keeping only

the first crystallographic mode results in,

$$\begin{aligned}\frac{\overline{F}}{k_b T \rho_{\text{ref}}} &= A(T) + \lambda(T)\psi_0 + (B_l(T))\frac{\psi_0^2}{2} - \frac{\psi_0^3}{6} + \frac{\psi_0^4}{12} \\ &+ 120A_{|G|}^4 + (32\psi_0 - 16)A_{|G|}^3 \\ &+ (12 - 12\psi_0 + 12\psi_0^2 - 12(1 + B_x + B_l(T)))A_{|G|}^2.\end{aligned} \tag{1.22}$$

In reference to our fixed volume numeric grid, we are keeping the total number of lattice sites conserved. When considering more exotic configurations that lack an analytic representation, the free energy and thermodynamic potentials may be extracted numerically.

To investigate what parameter range will favor a specific bulk phase, we build the associated phase diagram. Here we solve the condition of phase coexistence:

$$\mu_1 = \mu_2 \tag{1.23a}$$

$$f_1 - \overline{\rho_1}\mu_1 = f_2 - \overline{\rho_2}\mu_2. \tag{1.23b}$$

Here $\mu_i = \frac{\delta F}{\delta \rho}$ is the chemical potential and $\overline{\rho_i}$ coexistence density associated to phase i. The chemical potential may be extracted analogously to the free energy of Eq. 1.22,

$$\begin{aligned}\frac{\overline{\mu}}{k_b T \rho_{\text{ref}}} &= \lambda(T) + \psi_0 B_l(T) - \frac{\psi_0^2}{2} + \frac{\psi_0^3}{3} \\ &+ (-12 + 24\psi_0)A_{|G|}^2 + 32A_{|G|}^3,\end{aligned} \tag{1.24}$$

with A_G found through minimization of the free energy in Eq. 1.22 at a given average density and temperature. Although explicit calculation of the coexistence relations is possible, one can also make use of a convex hull algorithm of the free energy as detailed by Seymour *et al.* in their thesis [53]. Repeating the calculation at different temperatures and average densities results in a phase diagram as illustrated in figure 1.1. All coexistence lines need be determined when multiple phases are considered.

Past work on fitting the phase field crystal model parameters to experimental measures, has been restricted to the thermodynamics along the density plane [54, 55]. Such consideration is

sufficient when working under an isothermal approximation, though limiting the permissible temperature range of phase diagrams. The closest attempt at addressing the temperature thermodynamics has been done by Mellenthin *et al.* when fitting the phase field crystal amplitude heights to molecular dynamics simulations [56]. As part of this thesis, we shall form a connection to the Grueneisen equation of state for extension of the theory to the non-isothermal case.

1.5.3 Density Diffusion

In combination with the length scale captured in free energy of Eq. 1.19, phase field crystal models perform a time scale cutoff. By connection with hydrodynamics of global mass conservation,

$$\frac{\partial \rho}{\partial t} = \nabla \cdot D \nabla \frac{\delta F}{\delta \rho} + \nabla \cdot J_{\eta}. \tag{1.25}$$

The dynamics capture the local diffusion of mass and ordering, driven by gradients of the chemical potential, $\mu = \frac{\delta F}{\delta \rho} = k_b T \rho_{\text{reference}} \left[\log\left(\overline{\Lambda}\right) + (1 - C_2) * \psi \right]$. The vector field J_{η} denotes a noise current representative of fast processes on the order the atomic vibrations and which have been averaged out in the free energy functional. The noise current is assumed to obey, $\langle J_{\eta,i} \rangle = 0$ and $\langle J_{\eta,i} J_{\eta,j} \rangle = k_b T D \delta_{ij} \delta(t - t') \delta(r - r')$, where δ_{ij} is the Kronecker delta between vector directions i and j. This relation is of order the thermal scale in accordance with the fluctuation-dissipation theorem. The diffusion factor, D is often treated as a constant to allow for a linear description. In dynamic density functional theory, $D = D_0 + D_1 \rho$, since the lack of density cannot diffuse. This addition may be important in the study of vapour phases, which represent more complex phase field crystal variants [57, 58]. The constant diffusion assumption is expected valid for a sufficient density range. We note that Eq. 1.25 may alternatively be recast through, $\delta \rho = \rho_{\text{reference}} \delta \psi$, in terms of the dimensionless perturbation from our reference. The density field is generally propagated numeric in accordance with Eq. 1.25. This can be achieved through Euler time stepping or the pseudospectral methods that we outline in the following chapter [1].

Phase field crystal models captured by Eqs. 1.19 and 1.25 can be related to the liquid state structure factor, $S(q,t) = \langle |\delta \rho|^2 \rangle = \rho^2_{\text{reference}} \langle |\delta \psi|^2 \rangle$. As a result of spatial inversion symmetry,

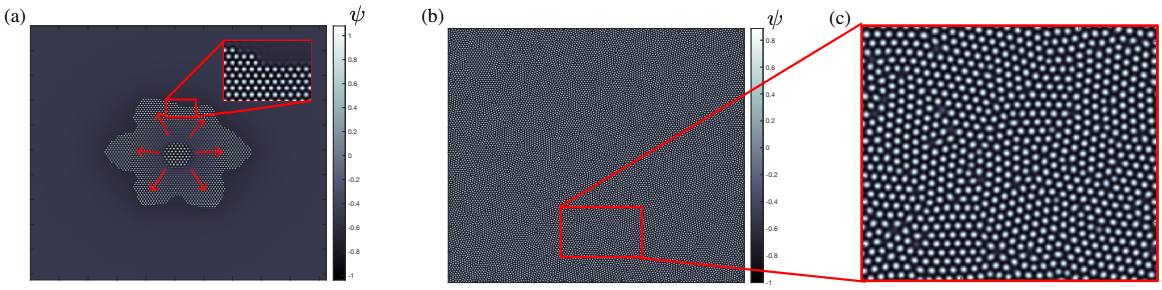

Figure 1.4: (a) An example simulation of the dendritic growth of an initial circular seed placed in an undercooled liquid melt. An inset is provided highlighting the faceted morphology at the solid-liquid interface. (b) Impingement patterning obtained after rapid crystallization. (c) An enhanced image of the grain structure and constituent dislocations.

the liquid state structure factor can in turn be related to the scattering functions described earlier. To start, Eq. 1.25 can be linearized,

$$\frac{\partial \mathscr{F}_k[\psi]}{\partial t} + Dk^2\left(1-\tilde{C}_2\right)\mathscr{F}_k[\psi] = \nabla \cdot J_\eta, \tag{1.26}$$

where the ideal free energy is truncated at second order. Recasting via an integrating factor,

$$\mathscr{F}_k[\psi](t) = e^{-Dk^2(1-\tilde{C}_2)t}\mathscr{F}_k[\psi](0) + \int_0^t dt' \left[\nabla \cdot J_\eta e^{Dk^2(1-\tilde{C}_2)(t'-t)}\right]. \tag{1.27}$$

Using the statistical properties of J_η, allows,

$$S(k,t) = \langle |\mathscr{F}_k[\psi](t)|^2 \rangle = e^{-2Dk^2(1-\tilde{C}_2)t}S(k,0) + \frac{k_bT}{2(1-\tilde{C}_2)}\left(1-e^{2Dk^2(1-\tilde{C}_2)t}\right). \tag{1.28}$$

In the seminal work of Elder *et al.*, the liquid static structure factor, $S(k,\infty)$, was shown a function of the parameters of entering $\tilde{C}_2$ [39]. The parameters were subsequently fit to the structure factor of liquid argon at $85K$. We note that the linearized structure factor computed in Eq. 1.28, has exponential decay character. In highly coupled systems, it is often the goal to find the stretched exponential exponent of time. This exponent can be indicative of alternative relaxation pathways.

Phase field techniques require specification of the anisotropic growth behaviour of an interface.

Meanwhile, the phase field crystal formulation explicitly includes the atomistic plasticity. As a result, solidification into an undercooled melt can result in the Mullins-Sekerka interface instability, akin to snowflake formation [36, 59]. Given an initial planar surface perturbation, a competition of lateral and longitudinal driving force results in the selection of a growth wavelength. The wavelength can grow stably for a select solidification velocity range, and is the center of intense study for microstructure selection [60–64]. Starting from a circular seed, symmetry of the snowflake arises as a result of the lattice structure of the solidifying phase. An example dendritic pattern is provided in subpanel (a) of figure 1.4 for a hexagonal lattice highlighting the resultant sixfold symmetry.

Nucleation statistics has been another area of study, because of the near infinite grain orientations captured in phase field crystal models [65–69]. This phenomenon lies at the start of solidification, when an activation barrier exists between the parent and daughter phases. Subpanel (b) of figure 1.4 illustrates the process, with a impinged grain boundary magnified in subpanel (c). The differing lattice orientations results in a grain boundary, comprised of a series of dislocations. The dislocations can be viewed as deformation of the lattice structure, where local spatial symmetry is broken. During impingement grain interactions can induce large stresses that can rotate a grains and introduce additional dislocations [70].

Dislocation formation and motion lie at the heart of the structural rigidity of a metal. Ideal lattices are prone to fracture along a given axis. By the addition of dislocations, energy can be contained in the dislocation dynamics. Such consideration is tantamount to time-temperature-transformation diagrams often used by metallurgists. Depending on the available energy, dislocations may climb or gliding along lattice planes. Nonetheless, sufficiently energy can still induce fracture, and in certain conditions, recrystallization of the underlying lattice. Dislocations and grain boundary dynamics have been the study of phase field crystal models for numerous years [71–73] and notably, the substantial work done by Berry *et al.* [74, 75].

As a result of the diffusive dynamics, dislocations instantaneously interact. To alleviate this behaviour, Stefanovic *et al.* introduced a wavelike extension of the density diffusion dynamics of Eq. 1.25, termed the modified phase field crystal model [76]. Further derived from hydrodynamics,

Majaniemi *et al.* showed that the second order time scale introduces propagating stress waves that carry information about nearby stress sources [77]. The modified phase field crystal model was shown capable in observing grain slip mechanisms for polycrystalline samples under imposed shear. Unfortunately, Berry *et al.* illustrated that the dislocation climb and glide timescale were inseparable [75]. Our recent work constructs a framework linking the second time scale to vacancy diffusion, which may allow the separation of climb and glide time scales [1]. A similar factor was added afterwards by Kun *et al.* to illustrate the time scale separation for amplitude phase field crystal variants [78].

1.6 Coupled Kinetics

Recent experiments in high energy solidification (rapid solidification [79, 80], laser melting [81–83], shock strengthening [84–86]) have found evidence of phases far off the expected phase diagram. In certain scenarios, amorphous patterns (lacking long-range crystal structure) can form [87]. Although characters of the amorphous phase can be garnered from caging dynamics in the time dependence of the correlation decay, no clear understanding of the amorphous phase is known. The high energy systems discussed here becoming increasingly common with the ability to rapidly cast, 3d print, and deform materials for desired structure. Thus it is necessary to study how the system will behave and what class of phenomena the dynamics fall under. The tenants of this thesis are in part built on the hypothesis that high energies can shift the local phase diagram, limiting energy relaxation.

The phase field crystal models that we have discussed thus far are highly idealized environments pertaining to a single solidifying species. In general, materials can be made out of multiple components, with competing lattice structures. As a result of the additional elements, phase space can become complex. In fact, the statistics associated with high entropy alloys (usually three or more species) remains a subject of intense debate [88, 89]. Luckily there exists a natural extension of the phase field crystal model to describe substitutional binary alloys [71]. In such systems, the free energy is supplemented by additional interaction correlation functions and entropic mixing

factors. This is then accompanied by diffusion equations for each species. Ofori-Opoku *et al.* have since developed a framework to describe multi-component substitutional alloys in the dilute limit [90]. We mention that at present intermetallic phases remain intractable.

With use of the binary phase field crystal variant, Berry *et al.* demonstrated that during solidification species competition can result in caging, observable in the auto-correlation function [91]. As a result of fluctuations, the system is capable of frustrating itself, unable to escape the local configuration. Later work by Fallah *et al.* documented the deviation from ideal Oswald-ripening due to the presence of dislocations [92, 93]. In particular, the dislocation agglomerates, which represent sites of high energy, drew in solute. The high local solute concentration, was shown sufficient to precipitate phases far from the global thermodynamics. Both studies are testament to our hypothesis of species limited energy relaxation. When solving the diffusion of a coarse-grained density field, the additional hydrodynamic Eqs. 1.5 are assumed instantaneously satisfied. It begs the question: "What limiting and caging behaviours arise from the added variables, and how may this feature explain a new class of emergent phenomena?" So we depart for the new territory of coupled dynamics, that describe the energetic dance of atoms, the atomic scale shuffle.

Chapter 2

Quasi-Phonons in Phase Field Crystal Models

Topological plasticity has been illustrated fundamental to the scale of atomic ordering, and the focus of phase field crystal models. Purely diffusive motion however, assumes instantaneous and local dislocation interactions. Wave-like density dynamics have been proposed to relax the free energy by density propagations, which emanate from stress sources, such as dislocations. The additional temporal time scale introduces *quasi-phonons* that propagate across a lattice. As phonon fluctuations move across the lattice, they can scatter of dislocations and grain-boundaries. This observation is then indicative of the interaction between short time ballistics and density diffusion. We thus begin investigation of our hypothesis on coupled and competing dynamics, in terms of lattice deformations and dislocation behaviours during solidification, which is central to the phase field crystal methodology. The following chapter pertains to our exploration and extension of the two timescale phase field crystal models, ensuring realistic couplings between phononic and mass diffusion [1]. In addition, we highlight a novel iteration scheme for rapid simulation that used throughout this thesis.

Time-scale Investigation with Modified Phase Field Crystal Method

Duncan Burns, Nikolas Provatas, Martin Grant

Abstract

This paper extends the two time-scale modified phase-field crystal model to examine crystal plasticity. Two non-linear density dependent functions are constructed to effectively represent hydrostatic strain and dislocation density. The functions are then used to develop a new modified phase field crystal model, which accounts for strain and strain-rate couplings on density dynamics. The non-linear additions provide tunable parameters for controlling dislocation climb versus glide, as well as phonon softening mechanisms. A short-wavelength dampening is also introduced to account for phonon scattering and thermoelastic dissipation processes. Finally, a novel semi-implicit numeric scheme for efficient simulations of this model is presented, which also serves as a generalization of the commonly used Fourier pseudo-spectral method. The technique gives rise to unconditionally stable dynamics with simple numeric implementation requirements.

2.1 Introduction

There has been increasing interest in the exploration of material microstructure evolution. Underlying structure can be an indicator of beneficial material properties for industrial applications, from bridge-design to nano-fabrication. As an example, a structure's fatigue resistance has been found to be correlated with the average grain size and disorder within a crystal [2.1]. Although much has been learned, microstructure growth remains a challenging and active area of current research due to the many competing time and length scales involved. First-principal methods, such as hydrodynamics, allow study of equilibrium structures. General materials can however be far out-of-equilibrium. Examples include martensitic steels, dislocation hardened metals, or multi-constituent alloys. To explore the growth of structures out-of equilibrium, effective simulation models and techniques are needed to probe the physics governing their formation and evolution.

Molecular dynamics methods are often employed which track the individual motions of atoms, generally solving Newton's equations. Therein atoms evolve in time by means of the working statistical ensemble. A specially chosen potential is used to describe atomic interactions. For example, Van der Waals forces can be included with the use of the Lennard-Jones type potentials. Hansen *et al.* [2.2] showed that such potentials enabled the study of structural phase transitions. In solving Newton's equations, molecular dynamics naturally incorporates multi-time scale events which can affect the resultant material structure. Unfortunately, computational requirements for molecular dynamics can restrict simulations to fast time scales on the order of nano-seconds and system sizes on the order of 100 atoms. The limitations can therefore involve the use of fictitious strain rates for example, and late stage morphologies can be difficult to observe experimentally.

Major advances in microstructure characterization have been made with the use of continuum phase-field methods, which allow for the description of order to disorder transitions by coupling thermodynamics fields to an order parameter. In particular, the effect of competing time scales may be studied by tracking the properties of the transition interface as a function time. However, phase-fields lack the granularity to treat atomistic motion and require substantial modifications to treat elasticity. To overcome the computational barrier of molecular dynamics while permitting

atomistic resolution, the phase field crystal (PFC) model was developed for the study of solidification [2.3]. PFC operates on diffusional time scales, set by vacancy diffusion, with a probability-like distribution representation of the density field [2.4]. Extensive studies have been conducted with the use of PFC to observe grain boundary dynamics [2.5] and varying nucleation events [2.6, 2.7]. PFC has proven to be a powerful methodology for micro-structure and material defect characterization near equilibrium, and for late-time conditions.

Out-of-equilibrium microstructure evolution often requires the coupling of diffusive and inertial time scales. As an example, phonons, elastic excitations within a material, can scatter and contribute to grain boundary screening [2.8], dislocation nucleation and destruction [2.9, 2.10], and induce varying types of phase transitions [2.11]. The study of such behaviours requires additional reactive modes to be included alongside diffusive dynamics. To incorporate effective phononic currents in phase field crystal models, Stefanovic *et al.* [2.12] proposed a phenomenological two-time scale damped wave equation termed the modified phase field crystal (MPFC) for the observation of dislocation diffusion through and along grain boundaries; a simplistic derivation of which will be examined here to understand the various contributions and effects one may expect. Using the MPFC approach, material elasticity and plasticity have been explored near the ideal solid state for a variety of crystalline symmetries [2.13, 2.14]. Further work done by Berry *et al.* used the MPFC variant to investigate the glass transition exhibited by two component metals [2.15] and found good agreement with experiments, illustrating caging.

The damped wave equation can thus be used to describe elastic waves, and its simple and natural form easily allow for two-time scales to be modelled. Majaniemi *et al.* derived the modified phase field crystal (MPFC) equation from linearized hydrodynamics and showed that under certain conditions the MPFC model incorporates phonon oscillations [2.16]. In particular, MPFC follows from hydrodynamics when strain diffusion dominates and viscous dissipation is negligible. While valid near the ideal crystal limit, the conditions break down in polycrystals and pseudo-liquid structures. Extensions to the MPFC model are thus required to describe fracture and higher frequency responses. As an example, phonon boundary scattering and softening can lead to the inability of phonons to jump across a grain boundary, leading to potential dislocation nucleation [2.17], ma-

terial failure [2.18] and lower thermal conductivity [2.19]. Multi-time scale PFC-hydrodynamic models have been developed to include the vibrational modes to study these systems at the cost of additional dynamic variables that can complicated the numerics [2.20]. Furthermore, plasticity couplings with the amplitude variant of phase field crystal model [2.21] have also been proposed [2.22].

This paper introduces two novel modifications to the existing MPFC modelling approach. The first is an alternative derivation of the MPFC model which self-consistently incorporates momentum dissipation. The second is a convolutional filtering procedure that extracts dislocation density and hydrostatic strain from the PFC density. Beyond providing a simple procedure for efficiently tracking dislocation and strain maps in time, this convolution on the density field is shown to correspond to a higher-order non-linear addition to the excess free energy, which also enters the MPFC dynamics. This non-linear addition to the dynamics allows for strain and strain rate couplings on vacancy dynamics, which can result in interesting out-of-equilibrium growth processes. A third contribution of this work is the derivation and application of a simple unconditionally stable (linear) numerical time-stepping algorithm based on exponential time integration [2.23]. This algorithm is shown to offer substantial numerical efficiency compared to the Euler time stepping algorithms used previously [2.13, 2.14]. The algorithm is applied to the new MPFC model, demonstrating its robustness on recovering late-stage Mullins-Sekerka instabilities of solid-liquid interfaces [2.24], and numerous rapid crystallization morphologies [2.25, 2.26]. It is expected that the MPFC model modification and the numerical approach introduced in this paper will permit the further exploration into time-scale couplings and quantification with the phase field crystal technique.

2.1.1 Phase Field Crystal

To begin a brief review of the phase-field crystal (PFC) technique is described [2.3]. PFC was first developed as an extension to phase field methods and complement to dynamic density functional theory. PFC operates by the time, t, evolution of a continuum coarse-grained density field, ρ,

acting as an order parameter through conserved Cahn-Hilliard type dynamics,

$$\frac{\partial \rho}{\partial t} = D\nabla^2 \mu + \nabla \cdot \eta_i. \tag{2.1}$$

Here D can be matched to the vacancy diffusion constant, and a thermodynamic current is introduced through the chemical potential, $\mu = \frac{\delta F}{\delta \rho}$, where F is the free energy. Processes that occur faster than the natural material diffusion contribute to the noise, η_i, which satisfies the usual fluctuation-dissipation theorem: $\langle \eta_i \rangle = 0$ and $\langle \eta_i \eta_j \rangle \propto k_B T \delta_{ij}$, where $k_B T$ is the thermal energy-scale. The system evolves along a path that minimizes the free energy. Construction of the free energy can be done by an expansion in correlations of the density functional free energy of freezing, as was proposed by Ramakrishnan *et al.* [2.27]:

$$\begin{aligned} F &= F_{\text{ideal gas}} + F_{\text{excess}} \\ &= \int_\Omega d\mathbf{r} \Big[\frac{\rho^2}{2} - \frac{\rho^3}{6} + \frac{\rho^4}{12} - \frac{\rho}{2}(C_2 * \rho) + ... \Big], \end{aligned} \tag{2.2}$$

where $\mathbf{r}$ denotes spatial position defined in a volume Ω. $C_2 * \rho$ represents the convolution of the density field with the two-point correlation function. Higher correlation functions can also appear in the theory, but for the sake of simplicity, this study will drop the higher order contributions. The distinguishing feature of phase-field crystals models is that their correlation function is built as an expansion in Fourier space, which can in some cases be taken back to real space. For this work, the two-point correlation function is taken to be the standard form,

$$C_2(\nabla^2) = -(B_l - 1) - 2B_x R^2 \nabla^2 - B_x R^4 \nabla^4, \tag{2.3}$$

where B_l is inversely proportional to the liquid state isothermal compressibility, B_x is related to the material elastic constants, and R, the unit cell size as described by Provatas *et al.* [2.4]. To eliminate the divergence of the correlation for large k, a smooth cut off may be taken to mimic the liquid state structure factor, found through $S(k)\ (1 - C_2(k))^{-1}$ [2.28]. Such a contribution may be

necessary in order to incorporate short length scale effects.

Equilibrium configurations arise as minima of the free energy and can be approximated by means of a one-mode expansion of the continuum density field:

$$\rho(\mathbf{r}) = \bar{\rho} + \rho_{\text{solid}} = \bar{\rho} + \sum_{\{\mathbf{G}\}} A_{\mathbf{G}} e^{i\mathbf{G}\cdot\mathbf{r}}, \tag{2.4}$$

where the sum is computed over reciprocal lattice vectors, $\mathbf{G}$, with long-range order being introduced through their complex amplitudes, $A_{\mathbf{G}}$. The correlation may thus be viewed as an interaction energy which assigns a cost between the disordered liquid, $\bar{\rho}$ and the ordered solid structure, ρ_{solid}. The preferred phase can be modulated through the effective temperature, $dB = B_l - B_x$. This difference affects the depth of the free-energy wells. Modifications of the correlation can be made to include different thermodynamic phases [2.29] and crystalline structures [2.30, 2.31].

The PFC model described through the equations (2.1-2.2) allows for the study of crystallization. Notably, topological defects such as dislocations and grain boundaries are naturally incorporated into the framework. In figure 2.1(A), a polycrystalline sample simulated with the PFC model is shown (Subpanels B-E are discussed in section 2.2). In the presence of dislocations the ideal lattice shifts by a deformation, $\mathbf{r} \rightarrow \mathbf{r} + \mathbf{u}$. Instead of delta sharp Bragg peaks, the strain broadens and shifts the Bragg peak profiles. The evolution of u is associated with phonon dynamics. In what follows the phase field crystal model is extended to include quasi-phononic behaviour. The local hydrostatic strain and dislocation density will be shown extractable through convolutional filters that are exploited to extend the single-field modified PFC formulation.

2.2 Modified Phase Field Crystal Model

As discussed above, Stefanovic *et al.* [2.12] made a phenomenological theory to incorporated the additional elastic excitations compared to the diffusive form of equation (2.1). This extension led

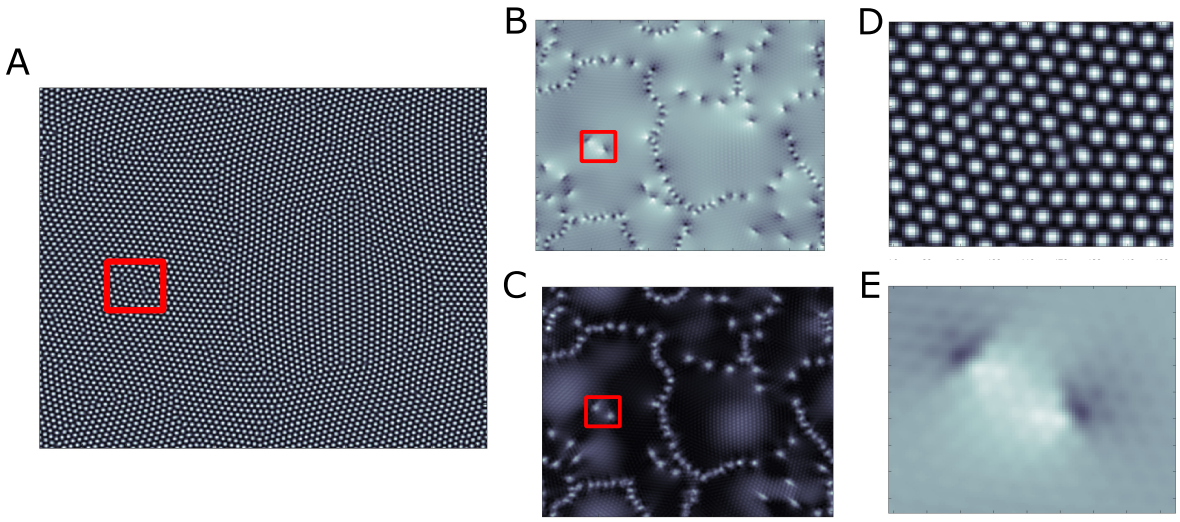

Figure 2.1: Illustrated in (A) is a polycrystalline sample simulated with the phase field crystal model. The system was prepared through seeded grain growth until impingement occurred on a 512×512 numeric grid. The grid spacing was selected to ensure a lattice length of roughly 10 grid points. Subpanel (B) highlights the dislocations present within the bulk and grain boundaries, constructed using equation (2.24). Subpanel (C) represents the effective hydrostatic strain field arising from the dislocations using equation (2.23). The gradient highlights the direction perpendicular to the slip plane and subsequently perpendicular to the Burger's vector. $\sigma_1 = 0.2$ and $\sigma_0 = 0.2$ were used for the filters. (D) and (E) show a zoom in of the density field and strain field respectively corresponding to the red square in panel (A). Figure adapted from [2.32].

to the modified phase field crystal with a dissipative wave equation,

$$\frac{\partial^2 \rho}{\partial t^2} + \beta \frac{\partial \rho}{\partial t} = D\nabla^2 \mu. \tag{2.5}$$

A central topic of discussion in this work will be how the parameter β introduces an inertial relaxation time of propagating modes. Treating β as a constant, Stefanovic *et al.* investigated plastic deformation, and found experimental agreement with reverse Hall-Petch weakening [2.33]. Likewise, Berry *et al.* explored dislocation dynamics described by the MPFC equation, finding dislocation creep, glide, and dislocation nucleation from pinned (and stressed) dislocation pairs [2.15]. However, the timescale for dislocation glide and climb were shown inseparable. Thus

further modifications to the MPFC are required to make the model more quantifiable.

2.2.1 Derivation

To discuss the various parameters entering in equation (2.5) a simplistic derivation is presented (a complete form can be found arising from linearized hydrodynamics [2.16]). The starting consideration is a volume of material under local mass and momentum conservation,

$$\frac{\partial \rho}{\partial t} = -\nabla \cdot \mathbf{g}, \tag{2.6}$$

and,

$$\frac{\partial \mathbf{g}}{\partial t} = -\nabla \cdot \sigma. \tag{2.7}$$

The above equations reflect the temporal evolution of the mass and momentum in response to the currents given by the momentum, $\mathbf{g}$, and stress, σ, respectively. The conservation laws hold as global constraints even in the coarse-grained limit ($t \gg 1$ and $k \ll 1$). Depending on the response length scales, the control volume may need to be sufficiently large. The two equations can be combined by taking a time derivative of the mass conservation equation,

$$\frac{\partial^2 \rho}{\partial t^2} = \nabla \cdot \nabla \sigma = \nabla \cdot (\nabla \sigma^R + \nabla \chi + \nabla \sigma^{\text{diss}}). \tag{2.8}$$

Here the stress tensor has been decomposed into reversible, σ_R, dissipative, σ_{diss}, and conditionally reversible stress contributions, χ. The reversible stress χ accounts for elastic material response when the distortion evolves slowly in time and gradually in space. The dissipative stress is to be interpreted as a memory dependent response. The conditionally reversible stress arises as a result of plastic deformation and motion, which should vanish near equilibrium. Defect dynamics such as vacancies and dislocations have been shown by Fleming *et al.* in the context of hydrodynamics to reduce the stress of the material [2.34]. Recently, Kim *et al.* showed that dislocation dynamics can result in stress reduction drops as a result of the bond breaking [2.35]. With sufficient kinetic energy, defects can also trigger dislocation nucleation [2.36], twinning [2.37], voiding [2.18], and

out-of-equilibrium phase transitions [2.38].

The constraints imposed by equation (2.8) are accompanied by the strain, u_{ij}, which represents the symmetry variables reflecting distortion from an ideal lattice [2.34, 2.39]. In particular, fluctuations of the density away from an ideal crystal can be related to pressure disturbances through,

$$\delta\rho \propto -\nabla \cdot \delta\mathbf{u}. \tag{2.9}$$

In the coarse-grained limit defect concentration will also affect the relation (2.9). Through a projection-operator formalism, Walz *et al.* [2.40], and separately Majaniemi *et al.* [2.16], determined a contribution from defects for the study of non-ideal crystals. The aim of projection-operator techniques is to separate slowly evolving variables of a system from faster components. This separation relates how fluctuations of the slow variables are coupled and introduces noise currents to approximate the faster dynamics. Through such a procedure, an additional variable, δc, corresponding to a defect density can be introduced (δc can also include higher strain terms). Relation (2.9) is then modified to account for defects,

$$\delta\rho \approx -\nabla \cdot \overline{\rho}\delta\mathbf{u} - \alpha\delta c, \tag{2.10}$$

where $\overline{\rho}$ is the average density and α is a tunable parameter coupling defects such as dislocations to local density. Density fluctuations are thus driven by a competition of the strain and defect dynamics. Expressing the correction δc in terms of strain leads to,

$$\delta\rho \approx -\nabla \cdot \overline{\rho}\delta\mathbf{u} - \alpha\nabla \cdot \delta u + \alpha\nabla \cdot \delta c_o. \tag{2.11}$$

The above decomposition may be motivated by recognizing that defects, vacancies and dislocations contribute to the strain in a material. Here the additional term $\nabla \cdot c_o$ can include higher order contributions to the strain and density. For simplicity let $\delta c_0 \to 0$, which is also valid in the low strain limit.

The non-dissipative stress can be determined through the thermodynamic identity,

$$\sigma_R + \chi \approx \frac{\delta E}{\delta u_{ij}}, \tag{2.12}$$

which relates the stress arising from variations in the system's total energy, E, to variations in strain, u_{ij}. The total energy is comprised of the kinetic energy and interaction energy. With the use of equation (2.11), the non-dissipative components of the stress may be determined via the chain rule for functionals,

$$\sigma_R + \chi = \int \frac{\delta E}{\delta \rho} \frac{\delta \rho}{\delta u_{ij}} = \overline{\rho}\mu_\rho - \alpha\mu_c, \tag{2.13}$$

in which the replacements $\frac{\delta E}{\delta \rho} = \mu_\rho$ and $\frac{\delta E}{\delta c} = \mu_c$ have been used. The total energy equation (2.13) shows that stress is generated from fluctuations of the mass and defect densities. The plastic, time dependent stress, can in general include higher order couplings between the density and defect fluctuations. Such effects can however be subsumed into a noise current when determining the relation (2.11), which has been set to 0 here for simplicity. Substitution of the equation (2.13) into equation (2.8) results in,

$$\frac{\partial^2 \rho}{\partial t^2} = \nabla^2(\overline{\rho}\mu) - \nabla^2(\alpha\mu_c) + \nabla \cdot \nabla \sigma^{\text{diss}}, \tag{2.14}$$

which shows that inertial density dynamics are thus impeded by the presence of defects within the crystal.

In the late time limit, diffusion is the dominant mode of the defect dynamics. Thus $\frac{\partial c}{\partial t} \approx \eta \nabla^2(\mu_c)$, where an appropriate diffusion constant, η, is introduced. One can further simplify equation (2.14) by noting that a time derivative of the equation (2.10) permits the substitution, $\frac{\partial \rho}{\partial t} \approx \alpha \frac{\partial c}{\partial t} + \overline{\rho} \nabla \cdot \frac{\partial \mathbf{u}}{\partial t}$. The strain contribution here reflects pressure wave disturbances, such as might occur from vacancies nucleating and moving through the bulk; for example, dislocation velocity can be reduced by the local phonon density, an effect termed dislocation drag [2.41]. The

above consideration reduce equation (2.14) to,

$$\frac{\partial^2 \rho}{\partial t^2} + \frac{1}{\eta}\frac{\partial \rho}{\partial t} - \frac{\overline{\rho}}{\eta}\nabla \cdot \frac{\partial \mathbf{u}}{\partial t} = \nabla^2(\overline{\rho}\mu_\rho) + \nabla \cdot \nabla \sigma^{\text{diss}}. \tag{2.15}$$

The aforementioned competition between density and defect dynamics results in a damped wave equation. Here, the vacancy diffusion constant η sets the scale of the dampening; however vacancy transport can also be assisted by a propagating strain field, thereby reducing the dampening factor. It is noted that the above strain dependence of the stress follows an empirical form also established in other studies of plastic deformation [2.42]. Such a term would not appear in an ideal solid, where the distortion field evolves slowly and gradually in space.

To proceed further, the parameter $\mu_\rho = \frac{\delta E}{\delta \rho}$ that emerges in equation (2.13) needs to be related to the chemical potential, $\mu = \frac{\delta F}{\delta \rho}$. To achieve this, the total energy can be related to the liquid-solid free energy, F, appearing in equation (2.2) by

$$E = F + \int \frac{|\mathbf{g}^2|}{2\overline{\rho}} - \gamma_o \int \delta c \nabla \cdot \mathbf{u}, \tag{2.16}$$

where the second term on the RHS represents the kinetic energy contribution. The parameter γ_o enters as a phenomenological constant scaling the third term, which has appeared previously in the study of two dimensional melting by Zippelius *et al.* [2.43] as the lowest order permissible coupling of the defect density and strain fields. Using the fluctuation relationship of equation (2.10) gives,

$$\frac{\delta}{\delta \rho}\int_\Omega d\mathbf{r}\, \delta c \nabla \cdot \mathbf{u} \approx \frac{-1}{\alpha}\nabla \cdot \mathbf{u}, \tag{2.17}$$

where the lowest order strain coupling is retained. The parameter μ_ρ may thus be related to the chemical potential through, $\mu_\rho = \mu + \frac{\gamma_o}{\alpha}\nabla \cdot \mathbf{u}$. Using this to replace μ_ρ in equation (2.15) gives,

$$\frac{\partial^2 \rho}{\partial t^2} + \frac{1}{\eta}\frac{\partial \rho}{\partial t} = \nabla^2(\overline{\rho}\mu) + \frac{\overline{\rho}}{\eta}\nabla \cdot \frac{\partial \mathbf{u}}{\partial t} + \frac{\overline{\rho}\gamma_o}{\alpha}\nabla^2 \nabla \cdot \mathbf{u} + \nabla \cdot \nabla \sigma^{\text{diss}}. \tag{2.18}$$

To avoid potential over-counting γ_o may be tuned [1].

[1]The strain-defect interaction in equation (2.16) can be derived from the free energy as a three point correlation

The second and third terms appearing in equation (2.18) can be identified with the properties of the conditionally reversible stress χ. In particular,

$$\nabla^2\chi = \frac{\overline{\rho}}{\eta}\nabla\cdot\frac{\partial\mathbf{u}}{\partial t} + \frac{\overline{\rho}\gamma_o}{\alpha}\nabla^2\nabla\cdot\mathbf{u}, \tag{2.19}$$

where γ_o enters as a phenomenological constant [2]. The strain-rate component arises from motion of plastic defects. Such a stress-strain-rate coupling has appeared in empirical form for the characterization of stress in plastic deformation [2.42]. The γ_o term is an additional contribution to χ that has been shown to arise from the coupling of the defect density and strain [2.43]. This term has previously appeared in the earlier work by Majaniemi *et al.* [2.16, 2.44] and may be the source of differing sound velocities between hydrodynamic and PFC models. It is noteworthy that in nearly equilibrated crystalline matter (i.e. or at late times in the evolution process) the dilational strain vanishes near equilibrium, i.e., $\nabla\cdot\mathbf{u}\to 0$, which makes the conditionally reversible stress in equation (2.19) vanish, as assumed.

Continuing on with the derivation of the new MPFC model, the dissipative stress components are approximated to recover an appropriate form in the coarse-grained limit. A simplistic and linearized form of the dissipation can be constructed through a viscosity parameter. The viscosity sets the momentum dissipation time, τ_R, through the relation, $\frac{1}{\tau_R}\nabla\sigma^{\text{diss}} = -\mathbf{g}$. Taking the divergence of this equation gives $\nabla^2\sigma^{\text{diss}} \approx -\tau_R\nabla\cdot\mathbf{g}$, which through the mass conservation results in $\nabla^2\sigma^{\text{diss}} = \tau_R\frac{\partial\rho}{\partial t}$. The relaxation time is in general a function of the defect density and is thus a spatial function. However, in our coarse-grained limit, a Taylor series expansion of the dissipation around $k=0$ is performed, with appropriate symmetry constraints. This results in

$$\tau_R \approx \nu_0 + \nu_2\nabla^2 + \nu_4\nabla^4 + \ldots \tag{2.20}$$

component of order $\mathcal{O}(\rho^3)$ using an effective strain field $\nabla\cdot\mathbf{u}_{\text{eff}}$ which is defined in the following section in equation (2.23). Such a coupling is missed using a PFC model expanded solely up two-point correlation in the excess energy as in equation (2.2).

[2] Some plastic stress is already accounted for in the usual PFC free energy, F. The extra components entering through the parameter χ act as higher order strain coupling, which necessarily arise at large deformations experienced in plasticity. The parameter γ_o can thus be tuned to account for possible double counting between these two effects.

In non-equilibrium crystals the vacancy diffusion rate mimics long-range dissipation, as was also assumed above. Due to the lack of long-range dissipation in ideal solids the zeroth order term vanishes, giving $\nu_0 = 0$. The second order term, ν_2 can be interpreted as Akhiezer dampening, resulting from phonon-phonon and phonon-defect scattering [2.45]. Thermoelastic wave-scattering is also incorporated into ν_2 [2.46]. Moriel *et al.* [2.47] demonstrated that in low temperature glasses ($\sim 50K$) the fourth order contribution, ν_4 dominates. They ascribe this feature to boundary scattering, because of the short-range symmetry. Since most of phase field crystal systems are restricted to near the melting point, ν_4 may be set to zero.

Using both equation (2.19) and equation (2.20) reduces equation (2.18) to the following modified MPFC form,

$$\frac{\partial^2 \rho}{\partial t^2} = \overline{\rho}\nabla^2 \mu - \left(\frac{1}{\eta} - \nu_2 \nabla^2\right) \frac{\partial \rho}{\partial t} + \nabla^2 \chi. \tag{2.21}$$

At late times, and close to the melting point, $\chi \to 0$ and the second order dissipation dominates. Under such conditions a traditional MPFC-type model is recovered, i.e.,

$$\frac{\partial^2 \rho}{\partial t^2} + \left(\frac{1}{\eta} - \nu_2 \nabla^2\right) \frac{\partial \rho}{\partial t} = \overline{\rho}\nabla^2 \mu. \tag{2.22}$$

Comparing equation (2.22) with original MPFC model of equation (2.5) reveals that the dissipation parameter has been modified here to account for contributions from the defect dynamics and friction-like dissipation effects, i.e., $\beta \to \left(1/\eta - \nu_2 \nabla^2\right)$.

2.2.2 Hydrostatic strain

Further simplification can be made to the form of equation (2.21) by rewriting χ into a density dependent function. This reconstruction allows for a single-variable field theory which accounts for the plasticity couplings introduced in equation (2.19). First some background will be provided about existing techniques to extract hydrostatic strain and defect density, then a new convolutional filter will be constructed.

Hÿtch *et al.* developed a convolution procedure to extract the small strain tensor from the one mode expansion by applying a Gaussian mask on the Bragg peak maxima positions. The approach is termed Geometric Phase Analysis [2.48] and its simplicity allows experimental determination of strain intensities and Burger's vectors in high resolution electron microscopy [2.49]. The work of Guo *et al.* [2.50] combined the use geometric phase analysis with phase field crystal methods in their study on grain dynamics. Geometric phase analysis has also appeared in the work of Skaugen *et al.* [2.51] and Liu *et al.* [2.52] for the study of dislocation dynamics. The technique, however, requires foreknowledge of the reciprocal lattice vectors, and is thus restricted to amplitude models developed by Elder *et al.* [2.21]. Nonetheless, one can extract some low-strain information based on the size of the Bragg circle, that is in the neighbourhood of $|\mathbf{G}|$ in Fourier space.

Ungár tabulated the structural features correlated with different types of structure factor peak aberrations [2.53]. Notably, dislocations and their strain profiles influence the asymmetry, as was studied by Groma *et al.* [2.54, 2.55]. Microstresses and grain boundaries lead to symmetric broadening of the diffraction peak. Asymmetry thus acts as a measure of the dislocations and strain independent from microstresses and grain boundary interface effects.

The following procedure may be performed to construct an effective hydrostatic strain field, $\nabla \cdot \mathbf{u}_{\text{eff}}$, based on the asymmetry of the structure factor peak,

$$\nabla \cdot \mathbf{u}_{\text{eff}} \approx \gamma_1 \mathscr{F}^{-1}\left[k e^{-\frac{k^2}{\sigma_0}} \mathscr{F}\left[\rho \mathscr{F}^{-1}\left[(k-|\mathbf{G}|) e^{-(k-|\mathbf{G}|)^2/(\sigma_1)} \mathscr{F}[\rho] \right] \right] \right], \tag{2.23}$$

where k denotes the radial wavenumber, and $\mathscr{F}$ is to be understood as a Fourier transform operation and σ_1 a scale to separate the long wavelength contributions to those near $|\mathbf{G}|$. In accordance with the correlation of equation (2.3), $|\mathbf{G}| = \frac{1}{R}$. The constant γ_1 sets the appropriate scale and proportionality. Note that the convolution is real provided the density is real. Shown in figure 2.1(B) is the strain field, computed through equation (2.23), which is generated by dislocations present within a polycrystalline sample. Figure 2.1(B) highlights the strain field produced from dislocations present within a polycrystalline sample. Sub-panel 2.1(E) zooms in on a pair of dislocations. The gradient in color from black to white points in a direction perpendicular to the Burger's vector

of the dislocation. Thus the polarity of a dislocation can be determined, through the nonlinear convolution (2.23). This construction alleviates the need to use peak fitters or foreknowledge of the reciprocal lattice vector direction. To obtain a smooth profile associated to long wavelengths, a Gaussian smoothing filter is applied with scale σ_0. Dislocations may further be separated from their polarities and strain information. By taking an absolute value of the Fourier coefficients near $|\mathbf{G}|$, a dislocation density, ρ_{dis}, may be constructed,

$$\rho_{\text{dis}} \approx \gamma_2 \left| \mathscr{F}^{-1}\left[e^{-(k-|\mathbf{G}|)^2/(\sigma_1)} \mathscr{F}[\rho] \right] \right|, \tag{2.24}$$

where γ_2 enters as a scale parameter. The above equation is in essence the Warren-Averbach method [2.56] used in X-ray diffraction to determine the average microstrain. Thus defects have been correlated as sources of strain within the material. An example of the dislocation density is presented in figure 2.1(C) where a Gaussian smoothing filter has been applied as in equation (2.23). The long range islands present within the grain bulks denote the presence of coherency strain. The coherency strain results from long-range bending of the ideal lattice structure due to the misfit at grain boundaries. Such a filter can track residual strain or dislocation density without the need for a peak-finder.

2.2.3 Modified MPFC model

By substituting the effective strain field $\nabla \cdot \mathbf{u}_{\text{eff}}$ form of equation (2.23) into equation (2.19), the conditionally reversible stress may be related to the density field according to

$$\nabla^2 \chi = \frac{\overline{\rho}}{\eta} \frac{\partial \mathscr{H}(\rho)}{\partial t} + \frac{\overline{\rho}\gamma_o}{\alpha} \nabla^2 \mathscr{H}(\rho), \tag{2.25}$$

where

$$\mathscr{H}(\rho) = \gamma_1 \mathscr{F}^{-1}\left[k e^{\frac{-k^2}{\sigma_0}} \mathscr{F}\left[\rho \mathscr{F}^{-1}\left[(k-|\mathbf{G}|) e^{-(k-|\mathbf{G}|)^2/(\sigma_1)} \mathscr{F}[\rho] \right] \right] \right] \tag{2.26}$$

is the convolutional filter introduced in equation (2.23). The component $\frac{\partial \mathscr{H}(\rho)}{\partial t}$ appearing in equation (2.25) can be further simplified by application of the chain rule,

$$\frac{\partial \mathscr{H}(\rho)}{\partial t} = \gamma_1 \mathscr{F}^{-1}\Bigg[k e^{\frac{-k^2}{\sigma_0}} \mathscr{F}\Big[\frac{\partial \rho}{\partial t}\mathscr{F}^{-1}\big[(k-|\mathbf{G}|)e^{-(k-|\mathbf{G}|)^2/(\sigma_1)}\mathscr{F}[\rho]\big] + \rho\mathscr{F}^{-1}\big[(k-|\mathbf{G}|)e^{-(k-|\mathbf{G}|)^2/(\sigma_1)}\mathscr{F}[\frac{\partial \rho}{\partial t}]\big]\Big]\Bigg] \tag{2.27}$$

Through equation (2.25) the strain dependent wave equation equation (2.21) may be recast into a modified MPFC equation written as a single-field theory in terms of density,

$$\frac{\partial^2 \rho}{\partial t^2} + \left(\frac{1}{\eta} - v_2\nabla^2\right)\frac{\partial \rho}{\partial t} = \overline{\rho}\nabla^2\mu - \gamma\nabla^2\mathscr{H}(\rho) + \phi\frac{\partial \mathscr{H}(\rho)}{\partial t}, \tag{2.28}$$

where $\gamma = \frac{\overline{\rho}\gamma_o}{\alpha}$ and $\phi = \frac{\overline{\rho}}{\eta\alpha}$. The strain-rate parameter ϕ in equation (2.28) introduces effective plastic couplings into the model. Since plastic material response can be highly temperature dependent future studies may entail making connection between ϕ and the lattice temperature. As is illustrated in figure 2.1, the effective hydrostatic strain vanishes along the glide plane of the dislocation. This is due to γ setting differing diffusion rates along the glide plane compared to perpendicular to it. Consequently, The strain-defect coupling, γ, can be used to modify the time scale difference between dislocation glide and climb. This is a new feature of this model not possible in previous PFC models, an innovation that should allow for a quantitative separation of time scales for dislocation glide mediated dynamics versus dislocation creep, which is climb dominated.

To summarize, this section derived a new modified phase field crystal (MPFC) model that incorporates non-equilibrium vacancy strain and strain-rate contributions to the dynamics of the density field. Crucial to the construction of this modified MPFC equation (2.28) was the use of a novel non-linear convolution defined by equation (2.23) to relate these effects in terms of a single density field ρ. The additional strain couplings are expected to allow for a more accurate description of non-equilibrium processes in rapid crystallization phenomena. Future studies will be done that utilize the added vacancy-strain components to study fracture strength and dislocation dynamics. Such an investigation may elucidate the role of vacancies in construction of a defor-

mation mechanism map, which separates diffusional flow, power-law creep, and plastic response regimes. Furthermore, phonon scattering of dislocations can yield measurements of the thermal conductivity of a polycrystal, as well as highlighting the role of grain boundary screening [3].

2.2.4 Memory Formalism Approach

It is noteworthy that with the use of an integrating factor equation (2.28) can be formally inverted into the following form,

$$\dot{\rho} = D\nabla \cdot \int_{-\infty}^{t} ds[M(t-s)K(t,s)(\nabla\mu(s) + \zeta)], \tag{2.29}$$

where the memory function, M is defined by $M(t) = De^{-t\beta}$ and where a noise source ζ has been tacitly added to equation (2.28). The function $K(t,s)$ includes the non-linear components which vanish near equilibrium, where $K(t,s) \to 1$. This type of equation was previously introduced by Galenko *et al.* [2.57] in their investigation of MPFC dynamics in the absence of defect/friction-related dissipation. The representation in equation (2.29) directly shows that the noise current, derivable from generalized Langevin dynamics, has an exponential correlation in time. This has similarly appeared in a subsequent study by Ankudinov *et al.* [2.58]. Equation (2.29) permits comparison to current correlations in models discussed in generalized hydrodynamic texts that include dissipative contributions [2.59] and mode coupling [2.60]. The reconstruction further allows discussion of two distinct limits of the memory function, $\beta \gg 1$ and $\beta \approx 1$.

When $\beta \gg 1$, the system is overdamped and the memory function reduces to $M(t) \to D\delta(t)$. As will be shown explicitly below, propagating modes only occur above a critical wavevector, which needs be tuned. In this limit of the memory function the diffusive dynamics of the original phase field crystal in equation (2.1) are recovered. It should be noted that in order to compare simulations of differing dampening coefficients (MPFC to PFC for example), time needs to be appropriately re-scaled. Following Berry *et al.* [2.15] one can introduce a renormalized time $\tau = \beta t$, where t denotes the iteration time.

[3] Grain boundary screening is also expected to play a role in the mechanics of dislocation pile-up.

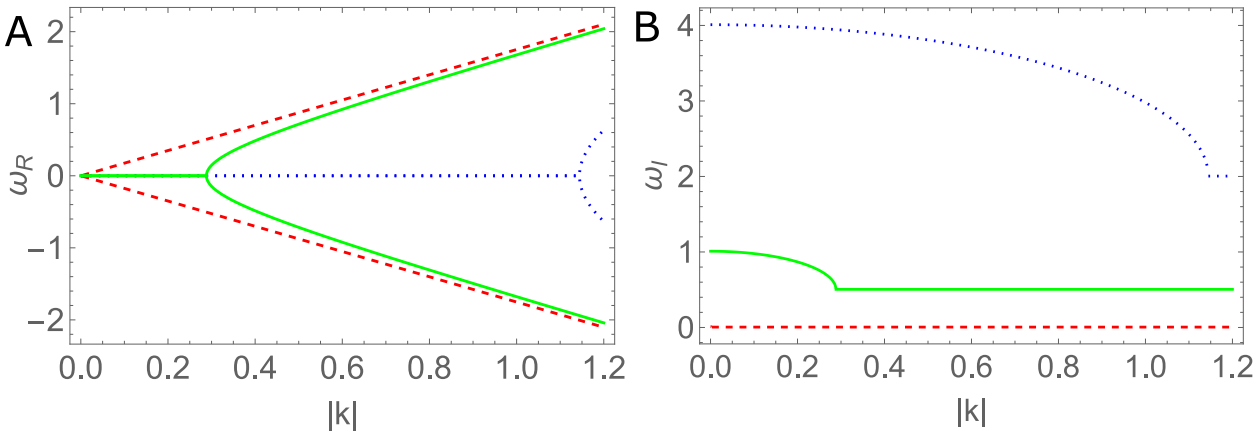

Figure 2.2: Illustrated is the real (A) and imaginary (B) dispersion curve for varying values of the dissipation when the viscous dissipation is set to zero, $\nu \to 0$. The real components represent propagating solutions, while the imaginary components reflect dampening of the wave. The following values for the dissipation were chosen: $\beta_0 = 0$ solid green line, $\beta_0 = 4$ red dashed line, $\beta_0 = 10$ dotted blue line. Other simulation parameter were chosen as follows: $B_x = 1$, $B_l = 0.8$, $\overline{\rho} = 0.1$, and $R = 1$. Figure adapted from [2.32].

When $\beta \approx 1$, the system is underdamped. In such a scenario density perturbations will propagate without dampening for a time, $t_\omega \propto \frac{1}{\beta}$. Low dampening can be used to explore phonon scattering and dislocation nucleation mechanisms from shock wave compression tests. Berry *et al.* [2.13] found that the underdamped limit of the previous MPFC equation can also capture caging behaviour in two-component glasses. It is expected that the additional contributions to the MPFC equation introduced in this work may in future permit the study of single-component metallic glasses.

2.2.5 Floquet Analysis

To better understand the propagation behaviour arising from the dissipation in our MPFC model, one can proceed similarly to Stefanovic *et al.* [2.12] through a Bloch-Floquet analysis applied to equation (2.5), which lends itself to the analysis of linear problems. The following discussion will thus consider the limit of $\chi \to 0$, i.e., on equation (2.22). This analysis considers a perturbation of

the density away from the ideal equilibrium density, which is represented as equation (2.4),

$$\rho(\mathbf{r}) = \rho_{\text{ideal}}(\mathbf{r}) + \sum_{\{\mathbf{G_0}\}} b_{\mathbf{G_0}} e^{i\mathbf{G_0}\cdot\mathbf{r}} e^{i\mathbf{Q}\cdot\mathbf{r}} e^{i\omega t}, \tag{2.30}$$

where $\mathbf{G_0}$ represents the set of reciprocal lattice vectors and the zero vector. In the above, variations of the amplitudes (and liquid) are considered through the fluctuations denoted by $b_{\mathbf{G_0}} e^{i\mathbf{Q}\cdot\mathbf{r}} e^{i\omega t}$. Substituting equation (2.30) into equation (2.5) and integrating over a unit cell will recover the effective dispersion relation. Keeping only linear terms of the fastest growing mode, b_0, the substitution yields,

$$-\omega^2 + i\beta\omega = -DQ^2\left(\overline{\rho}(\overline{\rho}-1) + \frac{3}{8}|A|^2 + \left(1 - C_2(Q)\right)\right), \tag{2.31}$$

where A is taken as the first order amplitude that minimizes the free energy. The effective dispersion relation can then be solved, yielding,

$$\omega(Q) = i\frac{\beta}{2} \pm \sqrt{\frac{-\beta^2}{4} + DQ^2\left(\overline{\rho}(\overline{\rho}-1) + \frac{3}{8}|A|^2 + \left(1 - C_2(Q)\right)\right)}. \tag{2.32}$$

To further explore the dispersion, one can decompose ω into propagating (real) and dissipative (imaginary) modes, i.e., $\omega = \omega_R + \omega_I$. The effective phase velocity can be determine by, $v_p = \omega_R/Q$, with a dissipation time $t_{\text{diss}} \approx \frac{1}{\omega_I}$. The propagating mode ω_R is illustrated in figure 2.2 for typical simulation parameters. Of particular note is the lack of long wavelength propagation as the dampening factor, β, is increased. Stefanovic *et al.* argued that the effect can be removed by forcing the propagation length, $L_{\text{prop}} = v_p t_{\text{diss}} \approx \frac{\omega_R}{Q\omega_I}$, to be larger than the maximum numeric system size. This poses a severe limitation in the ability of the previous MPFC model to capture experimentally relevant observations. Recent experimental [2.61] and theoretical work [2.62] has found that in visco-elastic liquids, long wavelength transverse waves are restricted to specific length scales. It is postulated that the lack of long-range order and the soft breaking of the spatial

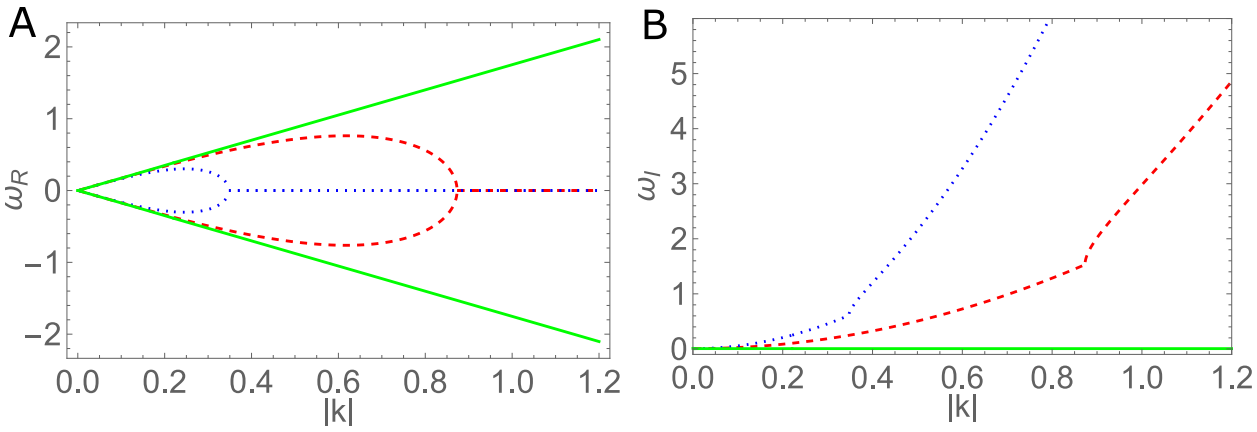

Figure 2.3: The dispersion relation of equation (2.32) is shown when the viscosity, $\beta \rightarrow \beta_0 + k^2\beta_1$ is introduced (A real part, B imaginary part). The following values for the viscosity were chosen: $\beta_2 = 0$ solid green line, $\beta_2 = 4$ red dashed line, $\beta_2 = 10$ dotted blue line. Other simulation parameter were chosen as follows: $B_x = 1$, $B_l = 0.8$, $\overline{\rho} = 0.1$, and $R = 1$. Figure adapted from [2.32].

symmetries results in the development of a k-gap [4]. The k-gap referred to above can be consistently captured by the new MPFC model introduced in this work.

Figure 2.3 illustrates the dispersion relation of equation (2.32) with the effective viscosity function introduced in this work. It is notable that increasing the viscosity results in a (temperature controlled) high $|k|$ cutoff above which propagation is impossible. The traditional MPFC model, with v_2 set to 0, is valid when observing vacancy dynamics near the ideal crystal state. However, in polycrystalline materials thermal/viscous dampening can result in high frequency phonon softening. Phonon softening can subsequently trigger dislocation nucleation [2.63]. It is noted that the k-gap contained in our new MPFC model is also consistent with the hydrodynamic phase field crystal extension of Heinonen *et al.* [2.20]. However, separating the transverse and longitudinal contributions of the propagation can be challenging with the MPFC formalism as they are coupled, and so the framework constructed by Heinonen *et al.* allows for easier separation of the components. On the other hand, the ease of this time scale separation comes with the loss of simplicity of a single variable theory/model. The dissipation of the new formulation facilities the simulation of

[4] As an example, Such a suppression of the long wavelength cutoff may permit the study of high temperature liquid-solid systems near the supercritical transition.

realistic hydrodynamic response with a single field, thereby significantly reducing the complexity.

2.3 Numerical Simulation Scheme

This section derives a generalization of the commonly used semi-implicit pseudo-spectral numerical integration method. This can be used to render efficient numerical simulations of the new MPFC equation introduced in this work, as well as a wide variety of other equations. The simplicity and unconditional stability in the linear source function are shown to be a general result of exponential time integration in both real and Fourier space.

2.3.1 General Form

The starting point is the definition of the density field ρ and its time derivative $\frac{\partial \rho}{\partial t}$ which lie on a numerical grid of size $\Omega = \Omega_x \times \Omega_y \times \Omega_z$. The new model outlined in equation (2.21) can be restructured into a 1st order matrix equation. This is done by introducing the vector $P = \begin{pmatrix} \rho \\ \dot{\rho} \end{pmatrix}$ as highlighted by Hadadifard *et al.* in their study of the generic damped wave equation [2.64]. Namely,

$$\frac{\partial P}{\partial t} = \begin{pmatrix} 0 & \mathbb{I} \\ L & -\beta(\nabla^2) \end{pmatrix} P + \begin{pmatrix} 0 \\ Nl \end{pmatrix}. \tag{2.33}$$

Here $L = D\nabla^2(1 - C_2)$ refers to the linear operations acting on the density field ρ, while $Nl = D\nabla^2(-t\rho^2 + v\rho^3) + \beta_{nl}$ includes the nonlinear contributions. The parameter β_{nl} can include other nonlinear couplings between ρ, $\frac{\partial \rho}{\partial t}$, or boundary conditions. The restriction of a physical density field and free energy enforces the operators L, and β to be real. For simplicity one may denote $F = \begin{pmatrix} 0 \\ Nl \end{pmatrix}$ and $M = \begin{pmatrix} 0 & 1 \\ L & -\beta \end{pmatrix}$. One can then integrate equation (2.33) between the current time point, t, and a numeric time step $t + dt$, which yields

$$P(t+dt) = \exp(Mdt)P(t) + \int_t^{t+dt} \exp\big(M(t+dt-s)\big)F(s)ds. \tag{2.34}$$

The first component on the right side of equation (2.34) captures consistent evolution of ρ and $\frac{\partial \rho}{\partial t}$ in response to the linear driving terms through a matrix exponential. The second component captures the nonlinear response and must be approximated due to the dynamic evolution of $F(t)$. Note that the exponential is a matrix operation and should be treated as short-hand for the corresponding series expansion.

Provided the integration bound is small one may approximate, $F(s) \approx F(t)$, allowing connection to the form of the pseudo-spectral method of Mellenthin *et al.* [2.65],

$$P(t+\delta t) \approx \exp(Mdt)P(t) + \sum_{n=0}^{\infty} M^n \frac{dt^{n+1}}{(n+1)!} F(t). \tag{2.35}$$

The matrix series term of equation (2.35) can be simplified when M is a non-singular matrix through the inverse operation, yielding

$$P(t+dt) \approx \exp(Mdt)P(t) + M^{-1}\big(\exp(Mdt) - 1\big)F(t). \tag{2.36}$$

When M is a circulant matrix [5] one will recognize that for the PFC operators, the $k = 0$ mode is the only singular eigenvalue of the matrix M. The singular component corresponds to a local conservation requirement. This reconstruction is reasonable to treat as an action on the vector $F(t)$ because the eigenvalues of $\big(\exp(Mdt) - 1\big)$ decay faster than M^{-1}. To further enforce density conservation, an auxiliary condition may also be introduced and solved at each time step according to

$$\frac{\partial \rho_{k=0}}{\partial t} = 0, \tag{2.37}$$

$$\rho_{k=0} = \bar{\rho}. \tag{2.38}$$

Equation (2.36) provides a generalized form of the semi-implicit integration scheme. Although equation (2.36) appears simple in form, the matrix exponential, which can be determined through an eigenvalue decomposition, can be notoriously difficult to utilize. In particular, the matrix ex-

[5] i.e., A square matrix that is diagonalized by a discrete fourier transform.

ponential is not guaranteed to be a sparse operation. If using grid sizes above 256^3 substantial computational memory is required to store the full exponential. In such a scenario techniques which avoid the need to store the matrix exponential are necessitated. This is investigated next.

When the matrix exponential is Taylor expanded, $\exp(Mdt) \approx \mathbb{I} + Mdt$, explicit Euler time stepping is recovered:

$$\begin{aligned} \rho(t+dt) &= \rho(t) + dt\frac{\partial \rho}{\partial t}, \\ \frac{\partial \rho(t+dt)}{\partial t} &= Ldt\rho(t) + (1-dt\beta)\frac{\partial \rho(t)}{\partial t} + dtNl(t). \end{aligned} \tag{2.39}$$

The required iteration matrices are reduced in memory cost by destabilizing the dynamics at increasing values of dt. To maintain stability at higher computation cost per iteration, a Padé approximation of the matrix exponential [2.66] can be made in equation (2.36), yielding

$$(\mathbb{I} - dtM)P(t+dt) = (\mathbb{I} + dtM/2)(P(t) + \begin{pmatrix} L^{-1}Nl(t) \\ 0 \end{pmatrix}) + (\mathbb{I} - dtM)\begin{pmatrix} L^{-1}Nl(t) \\ 0 \end{pmatrix}. \tag{2.40}$$

The (*n*,*m*) Padé approximation is a rational series representation with numerator of order n and denominator order m. That is, a function, $f(x)$, may be approximated by $\frac{Q_n(x)}{R_m(x)}$ for polynomials $Q_n(x)$ and $R_m(x)$ with order given by their subscripts. The (1,1) expansion used to construct equation (2.40) is $e^x = \frac{1+x/2}{1-x/2}$. When working with large sparse matrices the action of the inverse matrix, $(\mathbb{I} - dtM)^{-1}$ on a vector can be determined with the use of Gaussian elimination. One can save some computation time by preconditioning by means of an LU decomposition. Instead of rational series approximations, exponential Runge-Kutta can be used [2.66] or the scaling-squaring method of Mohy *et al.* [2.67].

2.3.2 Fourier Space

Adapting the above technique to Fourier space offers the advantage that the matrix exponential is sparse. This is seen by recognizing that the matrix M reduces to $\Omega_x \times \Omega_y \times \Omega_z$ (2x2) block diagonal matrices corresponding to the different Fourier wave vectors, k_i. An exponential of each

(2x2) matrix may then be analytically taken:

$$\exp(M_k dt) = \exp\left(-\frac{dt\beta}{2}\right)\begin{pmatrix} C+\beta S & 2S \\ 2L_k S & C-\beta S \end{pmatrix}, \tag{2.41}$$

where,

$$C = \cosh\left(\sqrt{4L_k+\beta^2}\frac{dt}{2}\right), \tag{2.42}$$

and,

$$S = \frac{\sinh\left(\sqrt{4L_k+\beta^2}\frac{dt}{2}\right)}{\sqrt{4L_k+\beta^2}}. \tag{2.43}$$

By substituting equation (2.41) into equation (2.36) one can arrive at the generalized form of the Fourier space scheme:

$$\rho_k(t+dt) = e^{-\frac{dt\beta}{2}}\left((C+\beta S)\rho_k(t)+2S\dot{\rho}_k(t)\right)+\left(e^{-\frac{dt\beta}{2}}(C+\beta S)-1\right)\frac{Nl}{L_k}, \tag{2.44}$$

and,

$$\dot{\rho}_k(t+dt) = e^{-\frac{dt\beta}{2}}\left((2L_k S)\rho_k(t)+(C-\beta S)\dot{\rho}_k(t)\right)+2Se^{-\frac{dt\beta}{2}}Nl, \tag{2.45}$$

where C and S are as defined in equation (2.41). The scheme of equations (2.44-2.45) provides a method to consistently evolve the density field and the corresponding time derivative.

In the overdamped limit, $\beta \to \infty$, the scheme (2.44-2.45) reduces to the pseudo-spectral form,

$$\rho_k(t+dt) = e^{L_k\frac{dt}{\beta}}\rho_k(t)+(e^{L_k\frac{dt}{\beta}}-1)\frac{Nl(t)}{L_k}. \tag{2.46}$$

Such a form, in this limit, has previously been outlined by Mellenthin *et al.* in their study on premelting [2.65] and is similar to that obtained by Chen *et al.* in their work on Cahn-Hilliard

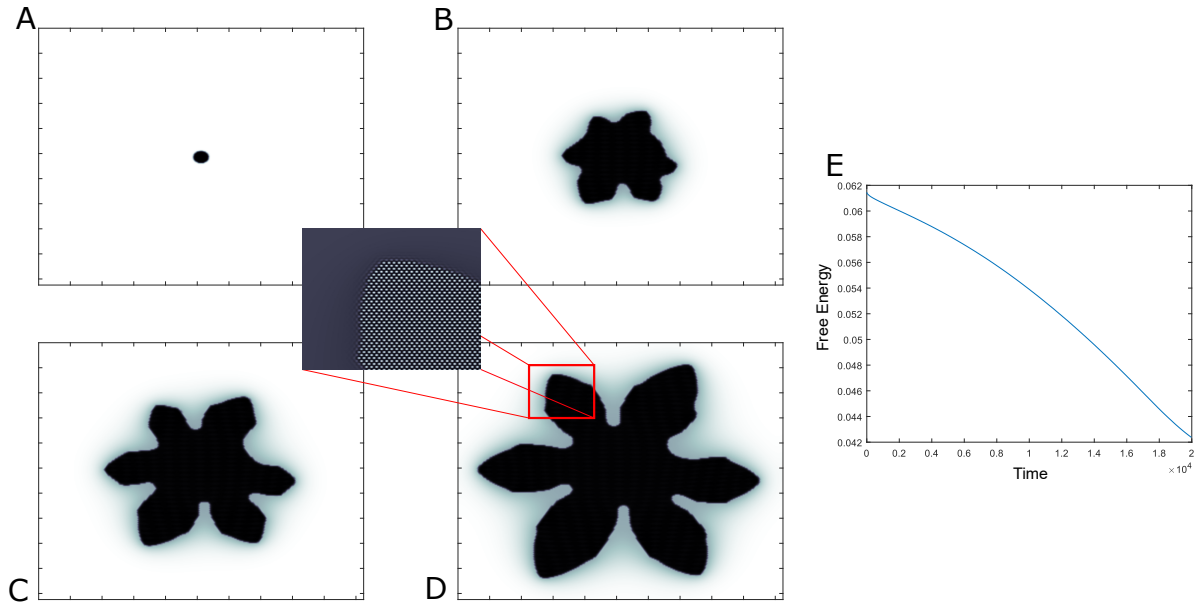

Figure 2.4: Illustrated in sub-figures A-D is the growth of a dendrite in time on a 2048×2048 numerical grid (A: t=0, B: t=50000, C: t=100000, D: t=160000). To remove unwanted Moire resolution effects from the images, a phase-field like filter is applied, $\rho_s = \mathscr{F}^{-1}\left[e^{-\frac{k^2}{0.2}}\mathscr{F}\left[|\rho_s|\right]\right]$, which separates liquid (white) from solid (black). A zoom in of the true density field of a dendrite branch is provided. Sub-figure E shows the free energy computed from equation (2.2) as a function of time. The numerical parameters of the system are as follows: $dx = dy = 1$, $B_l = 1$, $B_x = 1.4$, $dt = 0.1$, $R = \frac{10dx\sqrt{3}}{4\pi}$, $\beta = 60$, $D = 100$, $\overline{\rho} = -0.33$. Figure adapted from [2.32].

dynamics [2.68].

By proceeding through matrix exponentiation the form described by W. Zhou *et al.* [2.69] is recovered with a couple of differences. Notably the k=0 component of the model is solved separately through an auxiliary condition ensuring conservation of density. Furthermore equation (2.36) provides direct comparison to the popular pseudo-spectral method highlighting application in real space (which may be necessary for highly coupled dynamics) with effective boundary conditions that can be incorporated into the nonlinear component.

2.3.3 Convergence

The unconditional linear stability can be shown by noting the augmentation matrix exponential, $\exp(Mdt)$, is bounded in $[-1,1]$. Letting λ_i denote the i^{th} eigenvalue of the matrix M, one can check the stability of the linear contribution of equation (2.36) by ensuring $\lambda_i < 0$ since then $0 < \exp(Mdt) < 1$. Solving for the eigenvalues one finds,

$$\lambda_i = -\frac{\beta_k}{2} \pm \frac{1}{2}\sqrt{\beta_k + 4L_k}. \tag{2.47}$$

It is thus evident that $\lambda_i < 0$ for all k of our system, since $L_k < 0$ and equal only if $k = 0$. The stability requirement of explicit methods for solving the phase field crystal model, $dt \lessapprox dx^6$, can be avoided. The overall stability is however still dependent upon the nonlinear component, $F(t)$, and the approximation used to arrive at equation (2.35). Nonetheless, the stability improvement is observed to yield substantial computation efficiency dependent upon the dt, dx, and β parameters used.

Although stability provides values of the time step size for which the system does not diverge, consistency must also be ensured to obtain meaningful solutions. Consistency may be determined straightforwardly by proving the local truncation error vanishes in the limit dt and dx go to zero. The local truncation error is often defined as the difference of the partial differential equation and the scheme being utilized. Through a Taylor series expansion for small dt on both the $P(t+dt)$ and $\exp(Mdt)$ terms of equation (2.35). The truncation error can be found to be $\mathcal{O}(dt^2)$ arising from the approximation used for the non-linear terms. Note that in order to see the granularity of atoms, dx must be chosen smaller than the atomic lattice length set by R.

2.3.4 Demonstration of new MPFC Equation with Numerical Scheme

To illustrate the versatility of our algorithm at late times, an example of seeded dendrite growth is shown in figure 2.4. Often found in nature, such snowflake-like patterns emerge as a result of the well-known Mullins and Sekerka surface instability [2.24]. Since the solid phase has a preferred crystallographic direction the solid-liquid interface energy has anisotropic character. The

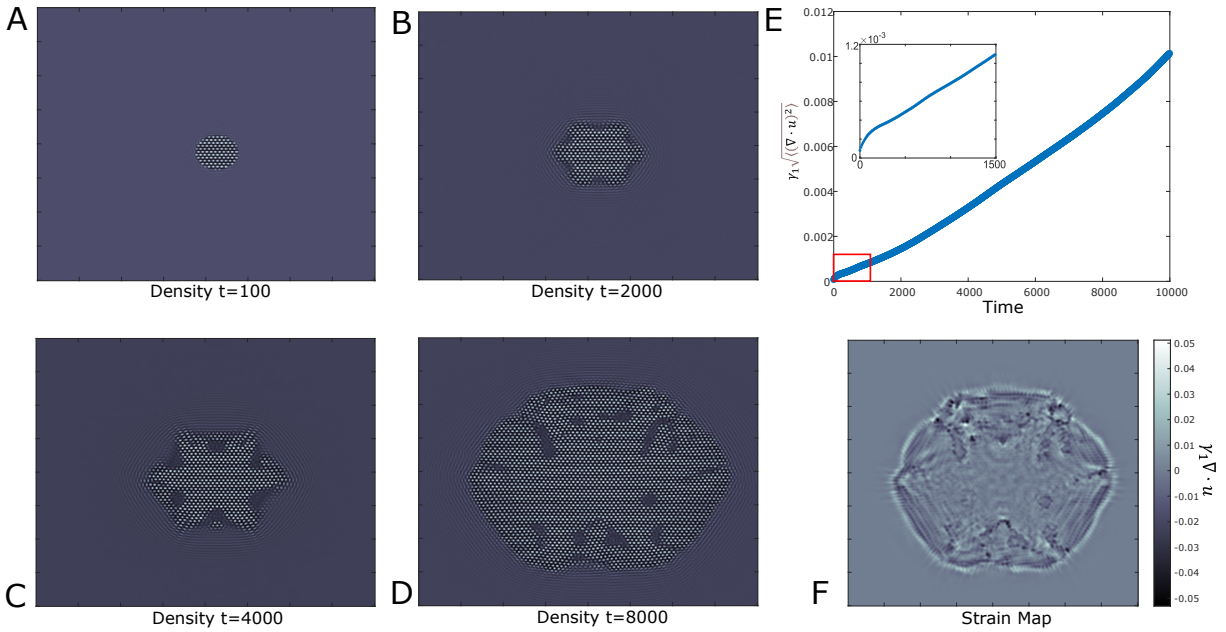

Figure 2.5: Illustrated in sub-figures A-D is the rapid crystallization of a circular seed placed in the center of a 2048x2048 numeric mesh (A: t=100, B: t=2000, C: t=4000, D: t=8000). Each snapshot has been zoomed in to a 800x800 sub-domain to highlight the atomic structure. Using the strain filter introduced in equation (2.23), sub-figure E highlights the root-mean-square hydrostatic strain as a function of simulation time. An inset is provided magnifying the region defined by the red box. Sub-figure F shows the hydrostatic strain map corresponding with sub-figure D (t=8000). A scale bar is provided with scale set by $\gamma_1 = 1$. The numeric parameters of the system are as follows: $dx = dy = 1$, $B_l = 1$, $B_x = 1.4$, $dt = 0.005$, $R = \frac{10dx\sqrt{3}}{4\pi}$, $\beta = 0.1$, $D = 10$, $\overline{\rho} = -0.3$. Figure adapted from [2.32].

anisotropy of the growing interface triggers the formation of a dendrite arm. For a hexagonal crystal, a sixfold symmetric dendrite is to be expected, which is recovered in figure 2.4. The asymmetry visible in subpanels B-C appears as a result of the one-mode-approximation used to initialize the system. As the system continues to grow the asymmetry vanishes. Furthermore, as the dendrites arms grow in size, their interface destabilizes resulting in further sidebranching. This subsequent phenomenon does not occur in the illustration since the chosen parameter set yields faster growth compared to the sidebranch formation time-scale. If the system were prepared in a state closer to the liquidus or the dendrites continued their growth up to a sufficient size, side

branching would occur. Figure 2.4(E) also illustrates a decreasing unitless free energy performed as a sanity check of the dynamics. The decrease is as expected of a system evolving toward equilibrium.

Beyond the standard surface instability leading to interesting growth morphologies in solidification, the growth rate of the solid-liquid interface during rapid crystallization has been shown coupled to strain dynamics that can have a strong impact on the resultant crystal morphology [2.70]. At low velocities, the growth is mediated by density diffusion at the boundary. Since this formation pathway can be understood from mass diffusion, the realm of low interface velocities are more amenable to traditional diffusive dynamics. With increasing velocity, crystallization transitions away from mass diffusion. The interface growth is then dominated by local strain and kinetic attachment effects. The novel contributions of the model introduced in this article become important during such rapid crystallization. Because of the speed of the interface, dislocations, liquid pools, and vacancies can be left behind within the bulk crystal as has been observed by Jreidini *et al.* [2.25] in their study on aluminium.

Figure 2.5 illustrates an example of the rapid crystallization microstructure starting from a circular seed. The presence of dislocations and liquid pools within the forming crystal are observed. Using equation (2.23) the root-mean-square of the hydrostatic strain was measured as a function of the evolution time and plotted in figure 2.5(E). At early times, the strain transitioned from logarithmic to linear dependence. Such behaviour has been reported previously by Jörgenson *et al.* [2.71] for the radius of a circular crystal nucleating and undergoing surface destabilization. It is suspected that at early times the strain is concentrated at the solid-liquid interface, thus scaling like the radius. As the growth progresses, there is evidence of some non-linearity, which may be related to the presence of defect structures entrenched in the bulk crystal. In particular, the solid-liquid interface moves faster than mass diffusion relaxes the lattice strain. As a result, the formation of defects may provide a means to alleviate the deformation build-up that occurs near the interface. The liquid pools and dislocations are shown in figure 2.5(F) to have dipolar-like strain fields, as additionally reported by Jreidini *et al.* [2.25], which form a dendritic-like profile within the bulk crystal. Through the strain distribution analysis of figure 2.5 the new formulation induced a strain-

interface coupling that emerges during rapid solidification. The new MPFC equation is hence an efficient method for exploring non-traditional strain effects in additive manufacturing. In addition to elucidating the role of dislocation dynamics during rapid crystallization, the new modified phase field crystal model can also be used in quantification of rapid crystallization experiments using new ultra-fast or dynamic transmission microscopy, which will be explored in future studies.

2.4 Conclusion

In summary, a novel derivation of the MPFC model was illustrated. Strain and dissipative contributions were added to the evolution equation missing from previous formulations. The strain additions are associated to the vacancy dynamics embedded into the form of the MPFC system. This vacancy-strain coupling relies on a novel convolution, introduced in equation (2.23), from which the hydrostatic strain can be approximated directly from the density field as a non-linear function. As such, the strain does not need to be explicitly tracked in time through an auxiliary dynamic equation, as is done in other hydrodynamic methods. Moreover, the vacancy-strain couplings provide a means to elucidate the time-scale difference between dislocation climb and glide allowing for the construction of deformation mechanism maps. In addition to the strain couplings, dissipative contributions reflecting thermal and phonon-self scattering are incorporated into the dynamics of the proposed formulation. The above effects are captured in the context of a single-variable modified MPFC dynamic equation (2.28). The associated linear propagation behaviour that enters into the new modified phase field crystal equation is examined. Dissipation results in the emergence of a low wavevector gap. Meanwhile, scattering mechanisms can result in a high wavevector cutoff, recovering a feature of previous hydrodynamic phase field crystal models, without however, requiring the complexity of a multi-field approach.

To complement the theoretical analysis, an efficient numerical time stepping algorithm (outlined in equations (2.44) and (2.45)) was also introduced for the efficient simulation of the new modified phase field crystal model introduced in this work. Late time growth forms were shown to be efficiently accessible with our numerical scheme and model. As a demonstration of our numer-

ical algorithm dendritic growth of a pure material was simulated. As the rapidity of crystallization increased, the solidification process was observed to be dominated by dislocation and liquid pool formations. These observations were consistent with past experiments of rapid solidification on aluminium thin-films. This effect of strain diffusion is expected to play a dominant role in microstructure formation mechanisms related to rapid solidification phenomena. The contributions described in this article provide a framework for future study of elasto-plastic response in rapid crystal growth and solid-state dynamics.

2.5 Acknowledgements

This work was supported by the NSERC (Natural Sciences and Engineering Research Council of Canada) and by *le Fonds de recherche du Québec—Nature et technologies*. Compute Canada and Narval are acknowledged for computing resources.

2.6 Bibliography

[2.1] Author Torquato S. and HW. Jr. Haslach. "Random Heterogeneous Materials: Microstructure and Macroscopic Properties". In: *Applied Mechanics Reviews* 55.4 (2002), B62–B63. ISSN: 0003-6900. DOI: 10.1115/1.1483342.

[2.2] J. P. Hansen and L. Verlet. "Phase Transitions of the Lennard-Jones System". In: *Physical Review* 184 (1 1969), pp. 151–161.

[2.3] K. R. Elder and M. Grant. "Modeling elastic and plastic deformations in nonequilibrium processing using phase field crystals". In: *Physical Review E* 70 (5 2004), p. 051605. DOI: 10.1103/PhysRevE.70.051605.

[2.4] "Phase Field Crystal Modeling of Pure Materials". In: *Phase-Field Methods in Materials Science and Engineering*. John Wiley & Sons, Ltd, 2010. Chap. 8, pp. 167–208. ISBN: 9783527631520. DOI: https://doi.org/10.1002/9F783527631520.ch8.

[2.5] A. Yamanaka, K. McReynolds, and P. W. Voorhees. “Phase field crystal simulation of grain boundary motion, grain rotation and dislocation reactions in a BCC bicrystal”. In: *Acta Materialia* 133 (2017), pp. 160–171.

[2.6] G. I. Tóth et al. “Polymorphism, crystal nucleation and growth in the phase-field crystal model in 2D and 3D”. In: *Journal of Physics: Condensed Matter* 22.36 (2010), p. 364101. DOI: 10.1088/0953-8984/22/36/364101.

[2.7] P. Jreidini, G. Kocher, and N. Provatas. “Classical nucleation theory in the phase-field crystal model”. In: *Physical Review E* 97 (4 2018), p. 042802.

[2.8] S. Fujii et al. “Quantitative prediction of grain boundary thermal conductivities from local atomic environments”. In: *Nature Communications* 11.1 (2020), p. 1854.

[2.9] T. Zhu et al. “Temperature and Strain-Rate Dependence of Surface Dislocation Nucleation”. In: *Physical Review Letters* 100 (2 2008), p. 025502.

[2.10] S. Chandra, M. K. Samal, and V.M. Chavan. “Dislocation nucleation from damaged grain boundaries in face centered cubic metals – An atomistic study”. In: *Materialia* 8 (2019), p. 100497.

[2.11] A. M. Lindenberg et al. “Time-Resolved X-Ray Diffraction from Coherent Phonons during a Laser-Induced Phase Transition”. In: *Physical Review Letters* 84 (1 2000), pp. 111–114.

[2.12] P. Stefanovic, M. Haataja, and N. Provatas. “Phase-Field Crystals with Elastic Interactions”. In: *Physical Review Letters* 96 (22 2006), p. 225504. DOI: 10.1103/PhysRevLett.96.225504.

[2.13] J. Berry and M. Grant. “Modeling Multiple Time Scales during Glass Formation with Phase-Field Crystals”. In: *Physical Review Letters* 106 (17 2011), p. 175702. DOI: 10.1103/PhysRevLett.106.175702.

[2.14] J. Berry et al. “Defect stability in phase-field crystal models: Stacking faults and partial dislocations”. In: *Physical Review B* 86 (22 2012), p. 224112. DOI: 10.1103/PhysRevB.86.224112.

[2.15] J. Berry and M. Grant. “Phase-field-crystal modeling of glass-forming liquids: Spanning time scales during vitrification, aging, and deformation”. In: *Physical Review E* 89 (6 2014), p. 062303. DOI: 10.1103/PhysRevE.89.062303.

[2.16] S. Majaniemi and M. Grant. “Dissipative phenomena and acoustic phonons in isothermal crystals: A density-functional theory study”. In: *Physical Review B* 75 (5 2007), p. 054301. DOI: 10.1103/PhysRevB.75.054301.

[2.17] C. L. Kelchner, S. J. Plimpton, and J. C. Hamilton. “Dislocation nucleation and defect structure during surface indentation”. In: *Physical Review B* 58 (17 1998), pp. 11085–11088.

[2.18] R. E. Rudd and J. F. Belak. “Void nucleation and associated plasticity in dynamic fracture of polycrystalline copper: an atomistic simulation”. In: *Computational Materials Science* 24.1 (2002), pp. 148–153.

[2.19] X. Li and S. Lee. “Role of hydrodynamic viscosity on phonon transport in suspended graphene”. In: *Physical Review B* 97 (9 2018), p. 094309.

[2.20] V. Heinonen et al. “Consistent Hydrodynamics for Phase Field Crystals”. In: *Physical Review Letters* 116 (2 2016), p. 024303.

[2.21] K. R. Elder, Z. Huang, and N. Provatas. “Amplitude expansion of the binary phase-field-crystal model”. In: *Physical Review E* 81 (1 2010), p. 011602.

[2.22] A. Skaugen, L. Angheluta, and J. Viñals. “Separation of Elastic and Plastic Timescales in a Phase Field Crystal Model”. In: *Physical Review Letters* 121 (25 2018), p. 255501.

[2.23] S. Chandrasekhar. “Stochastic Problems in Physics and Astronomy”. In: *Review Modern Physics* 15 (1 1943), pp. 1–89.

[2.24] W. W. Mullins and R. F. Sekerka. “Stability of a Planar Interface During Solidification of a Dilute Binary Alloy”. In: *Journal of Applied Physics* 35.2 (1964), pp. 444–451. DOI: 10.1063/1.1713333.

[2.25] P. Jreidini et al. “Orientation Gradients in Rapidly Solidified Pure Aluminum Thin Films: Comparison of Experiments and Phase-Field Crystal Simulations”. In: *Physical Review Letters* 127 (20 2021), p. 205701. DOI: 10.1103/PhysRevLett.127.205701.

[2.26] L. Gránásy et al. “Phase-field modeling of crystal nucleation in undercooled liquids – A review”. In: *Progress in Materials Science* 106 (2019), p. 100569.

[2.27] T. V. Ramakrishnan and M. Yussouff. “First-principles order-parameter theory of freezing”. In: *Physical Review B* 19 (5 1979), pp. 2775–2794. DOI: 10.1103/PhysRevB.19.2775.

[2.28] H. Emmerich et al. “Phase-field-crystal models for condensed matter dynamics on atomic length and diffusive time scales: an overview”. In: *Advances in Physics* 61.6 (2012), pp. 665–743. DOI: 10.1080/00018732.2012.737555.

[2.29] G. Kocher and N. Provatas. “New Density Functional Approach for Solid-Liquid-Vapor Transitions in Pure Materials”. In: *Physical Review Letters* 114 (15 2015), p. 155501.

[2.30] N. Ofori-Opoku et al. “Multicomponent phase-field crystal model for structural transformations in metal alloys”. In: *Physical Review B* 87 (13 2013), p. 134105. DOI: 10.1103/PhysRevB.87.134105.

[2.31] M. Seymour and N. Provatas. “Structural phase field crystal approach for modeling graphene and other two-dimensional structures”. In: *Physical Review B* 93 (3 2016), p. 035447.

[2.32] D. Burns, N. Provatas, and M. Grant. “Time-scale investigation with the modified phase field crystal method”. In: *Modelling Simulation Material Science and Engineering* 30 (6 2022), p. 064001. DOI: 10.1088/1361-651X/ac7c83.

[2.33] P. Stefanovic, M. Haataja, and N. Provatas. “Phase field crystal study of deformation and plasticity in nanocrystalline materials”. In: *Physical Review E* 80 (4 2009), p. 046107. DOI: 10.1103/PhysRevE.80.046107.

[2.34] P. D. Fleming and C. Cohen. “Hydrodynamics of solids”. In: *Physical Review B* 13 (2 1976), pp. 500–516. DOI: 10.1103/PhysRevB.13.500.

[2.35] S. Kim et al. “Phonon scattering during dislocation motion inducing stress-drop in cubic metals”. In: *Acta Materialia* 115 (2016), pp. 143–154.

[2.36] D. Tanguy et al. “Dislocation nucleation induced by a shock wave in a perfect crystal: Molecular dynamics simulations and elastic calculations”. In: *Physical Review B* 68 (14 2003), p. 144111.

[2.37] C. E. Wehrenberg et al. “In situ X-ray diffraction measurement of shock-wave-driven twinning and lattice dynamics”. In: *Nature* 550.7677 (2017), pp. 496–499.

[2.38] G. E. Duvall and R. A. Graham. “Phase transitions under shock-wave loading”. In: *Review Modern Physics* 49 (3 1977), pp. 523–579.

[2.39] P. C. Martin, O. Parodi, and P. S. Pershan. “Unified Hydrodynamic Theory for Crystals, Liquid Crystals, and Normal Fluids”. In: *Physical Review A* 6 (6 1972), pp. 2401–2420. DOI: 10.1103/PhysRevA.6.2401.

[2.40] C. Walz and M. Fuchs. “Displacement field and elastic constants in nonideal crystals”. In: *Physical Review B* 81 (13 2010), p. 134110. DOI: 10.1103/PhysRevB.81.134110.

[2.41] H. Fan et al. “Strain rate dependency of dislocation plasticity”. In: *Nature Communications* 12.1 (2021), p. 1845.

[2.42] C. Zener and J. H. Hollomon. “Effect of Strain Rate Upon Plastic Flow of Steel”. In: *Journal of Applied Physics* 15.1 (2004), pp. 22–32. ISSN: 0021-8979. DOI: 10.1063/1.1707363.

[2.43] A. Zippelius, B. I. Halperin, and D. R. Nelson. “Dynamics of two-dimensional melting”. In: *Physical Review B* 22 (5 1980), pp. 2514–2541.

[2.44] S. Majaniemi, M. Nonomura, and M. Grant. “First-principles and phenomenological theories of hydrodynamics of solids”. In: *The European Physical Journal B* 66.3 (2008), pp. 329–335.

[2.45] A. Akhiezer. “On the Absorption of Sound in Solids”. In: *Journal of Physics (Moscow)* 1.1 (1939), pp. 277–287.

[2.46] W. P. Mason. “Phonon Viscosity and Its Effect on Acoustic Wave Attenuation and Dislocation Motion”. In: *The Journal of the Acoustical Society of America* 32.4 (2005), pp. 458–472. ISSN: 0001-4966. DOI: 10.1121/1.1908099.

[2.47] A. Moriel et al. “Wave attenuation in glasses: Rayleigh and generalized-Rayleigh scattering scaling”. In: *The Journal of Chemical Physics* 151.10 (2019), p. 104503. ISSN: 0021-9606. DOI: 10.1063/1.5111192.

[2.48] M. J. Hÿtch, E. Snoeck, and R. Kilaas. “Quantitative measurement of displacement and strain fields from HREM micrographs”. In: *Ultramicroscopy* 74.3 (1998), pp. 131–146.

[2.49] J.L. Rouvière and E. Sarigiannidou. “Theoretical discussions on the geometrical phase analysis”. In: *Ultramicroscopy* 106.1 (2005), pp. 1–17.

[2.50] Y. Guo et al. “Strain mapping in nanocrystalline grains simulated by phase field crystal model”. In: *Philosophical Magazine* 95.9 (2015), pp. 973–984.

[2.51] A. Skaugen, L. Angheluta, and J. Viñals. “Dislocation dynamics and crystal plasticity in the phase-field crystal model”. In: *Physical Review B* 97 (5 2018), p. 054113.

[2.52] Z.Y. Liu et al. “A nanoscale study of nucleation and propagation of Zener types cracks at dislocations: Phase field crystal model”. In: *Computational Materials Science* 179 (2020), p. 109640.

[2.53] T. Ungár. “Microstructural parameters from X-ray diffraction peak broadening”. In: *Scripta Materialia* 51.8 (2004), pp. 777–781.

[2.54] I. Groma, T. Ungár, and M. Wilkens. “Asymmetric X-ray line broadening of plastically deformed crystals. I. Theory”. In: *Journal of Applied Crystallography* 21.1 (1988), pp. 47–54. DOI: https://doi.org/10.1107/S0021889887009178.

[2.55] I. Groma and G. Monnet. “Analysis of asymmetric broadening of X-ray diffraction peak profiles caused by randomly distributed polarized dislocation dipoles and dislocation walls”. In: *Journal of Applied Crystallography* 35.5 (2002), pp. 589–593. DOI: https://doi.org/10.1107/S0021889802010695.

[2.56] B.E. Warren. “X-ray studies of deformed metals”. In: *Progress in Metal Physics* 8 (1959), pp. 147–202.

[2.57] P. Galenko, D. Danilov, and V. Lebedev. “Phase-field-crystal and Swift-Hohenberg equations with fast dynamics”. In: *Physical Review E* 79 (5 2009), p. 051110.

[2.58] V. Ankudinov et al. “Correlated noise effect on the structure formation in the phase-field crystal model”. In: *Mathematical Methods in the Applied Sciences* 44.16 (2021), pp. 12185–12193. DOI: https://doi.org/10.1002/mma.6887.

[2.59] J. P. Hansen and I. R. McDonald. *Theory of Simple Liquids*. Elsevier Science, 2006. ISBN: 9780080455075.

[2.60] J. P. Boon and S. Yip. *Molecular Hydrodynamics*. Dover books on physics. Dover Publications, 1991. ISBN: 9780486669496.

[2.61] R. M. Khusnutdinoff et al. “Collective modes and gapped momentum states in liquid Ga: Experiment, theory, and simulation”. In: *Physical Review B* 101 (21 2020), p. 214312.

[2.62] M. Baggioli and A. Zaccone. “Unified theory of vibrational spectra in hard amorphous materials”. In: *Physical Review Research* 2 (1 2020), p. 013267. DOI: 10.1103/PhysRevResearch.2.013267.

[2.63] W. W. Pang et al. “Dislocation creation and void nucleation in FCC ductile metals under tensile loading: A general microscopic picture”. In: *Scientific Reports* 4.1 (2014), p. 6981.

[2.64] F. Hadadifard, S. Malhi, and Z. Xiao. “A class of Finite difference Methods for solving inhomogeneous damped wave equations”. In: *arXiv preprint arXiv:2008.08043* (2020).

[2.65] Jesper Mellenthin, Alain Karma, and Mathis Plapp. “Phase-field crystal study of grain-boundary premelting”. In: *Physical Review B* 78 (18 2008), p. 184110. DOI: 10.1103/PhysRevB.78.184110.

[2.66] C. Moler and C. Van Loan. “Nineteen dubious ways to compute the exponential of a matrix, twenty-five years later”. In: *SIAM review* 45.1 (2003), pp. 3–49.

[2.67] A. H. Al-Mohy and N. J. Higham. “Computing the action of the matrix exponential, with an application to exponential integrators”. In: *SIAM journal on scientific computing* 33.2 (2011), pp. 488–511.

[2.68] L. Q. Chen and J. Shen. “Applications of semi-implicit Fourier-spectral method to phase field equations”. In: *Computer Physics Communications* 108.2-3 (1998), pp. 147–158.

[2.69] W. Zhou et al. “Mechanical relaxation and fracture of phase field crystals”. In: *Physical Review E* 99.1 (2019), p. 013302.

[2.70] P. K. Galenko et al. “Thermodynamics of rapid solidification and crystal growth kinetics in glass-forming alloys”. In: *Philosophical Transactions of the Royal Society A: Mathematical, Physical and Engineering Sciences* 377.2143 (2019), p. 20180205.

[2.71] L. Jörgenson et al. “Early-time regime for interfacial instabilities in a kinetic Ising model”. In: *Physical Review E* 48 (6 1993), pp. 4592–4598.

Chapter 3

Phonon Caging

Thus far we have constructed a theoretic and numerical framework to investigate how phonon motion can be coupled to density diffusion. In addition, we have introduced minimal couplings between vacancy and density dynamics, including hydrostatic strain. coupled diffusion observations in rapid solidification. The following chapter applies the formulations developed in the previous chapter to the examination of phonon scattering on polycrystalline materials. In particular we measure the density autocorrelation function, highlighting evidence of dynamic cross-over regime between ballistic and grain boundary diffusion. This behaviour has been measured in past experiments, and thus we provide a thermodynamic view of phonon-grain boundary pile up.

Two-Dimensional Phase Field Crystal Simulation of Laser Induced Recrystallization: A Mechanism of Grain-Boundary Phonon Scattering and Softening

Duncan Burns, Nikolas Provatas, Martin Grant

Abstract

In this article we present the first numerical investigation of phonon relaxation in two-dimensional polycrystalline systems simulated with a multi-timescale phase field crystal model. We first measure the phonon spectrum averaged over different polycrystalline configurations, using thermal fluctuations to capture the rapid processes. We find two main peaks in the spectrum attributable, respectively, to dampening and softening of different wavelength phonons. In particular, it is shown that polycrystals have a phonon caging regime, a signature of amorphous materials. Subsequently, we report on a mechanism of grain-boundary melting resulting from the accumulation of phonon scattering. We find this behaviour exhibited in both rapid temperature annealing of polycrystalline samples and from input of kinetic energy representative of rapid laser heating or hot-rolling. In the latter case, we theorize a rate relation between the maximally achieved liquid fraction as a function of the initial kinetic energy, defining a metastable activation energy that can be measured in experiments. We expect that the scattering mechanisms investigated in this work underpin grain-boundary melting and recrystallization processes encountered in rapid solidification experiments.

3.1 Introduction

Despite significant progress in understanding how the microstructure controls the properties of many materials, the dynamical mechanisms that govern non-equilibrium microstructure formation remain arcane. The challenge is tied to the plethora of interaction pathways between competing time and length scales. In this sense, the behaviour of a metal is subject to the underlying atomic lattice structure that sets a fundamental length scale. Depending on local available energy, the atoms can break their spatial symmetry to form a melt, void, fracture or nucleate a dislocation. These metastable defect structures are linked to resultant changes in macroscale properties, such as hardness or ductility. In addition to the length scale, vibration of atoms sets a fundamental time-scale. Phonons propagate through a material, transferring energy that can precipitate defects, cause phase transformations, or recrystallization. The scattering of phonons off metastable structures can also alter the transport properties, such as thermal conductivity. To fabricate optimized materials in rapid processes such as additive manufacturing or shock peening, the study of dynamical defect formation and plasticity is ergo imperative.

The preferential recrystallization at sites of high strain energy is well documented [3.1]. This idea is crucial in rolling, where polycrystals are mechanically distorted [3.2]. Recent experiments on stainless steels [3.3, 3.4] have demonstrated that energy input from a laser, or shock front [3.5], can have a similar effect. With lower imparted energies, long-lived melt-pools have been found that emanate from grain boundaries [3.6, 3.7]. Liquid close to the solidification temperature has been measured with incoherent neutron scattering to capture the caging regime of the dynamic structure factor [3.8], a feature that has been recently reported in polycrystals [3.9]. Unfortunately, some of these experiments rely on post-mortem analyses. As a result, the dynamical mechanisms at play remains elusive.

During material processing, phonons scatter and soften, potentially increasing the local energy density through dampening. Many studies have been conducted on the heat transport behaviour in amorphous materials, where the lack of long-range structure allows excessive phonon dampening [3.10, 3.11]. The energy absorption can be seen by frequency peaks in the phonon density of

states, amenable to Raman scattering experiments. Meanwhile, dips in spectrum denote regions of phonon depletion. A large band is often found in the terahertz frequency range, termed the Boson peak. In recent literature, conflicting arguments have been given of the cause of the Boson peak [3.12–3.14]. Starting from a dampening process in the dispersion relation, Bagglioli *et al.* demonstrated the appearance of such a peak feature [3.15, 3.16]. Often associated to glassy materials, polycrystals have been shown to exhibit similar caging properties as in glasses [3.9]. We thus expect, polycrystals also exhibit a Boson peak with suppressed prominence, depending on the grain-boundary density. At lower frequencies, van Hove singularities can also appear in polycrystalline materials, whose dispersion relation becomes singular. Herein we show the existence of both types of peak structures and their contributions from phonons of different length scales.

Few simulation methods exist to complement experiments in the study the late stage diffusion behaviour resulting from phononic propagation. Conventional phonon scattering analyses at the atomistic scale can be carried out with molecular dynamics. However, phonon coupling to the resultant structure profile can be intractable to explore due to the limiting numerical time step step by vacancy hopping. For this reason, we employ the phase field crystal (PFC) methodology originally developed Elder *et al.*, which simulates the temporally averaged density field [3.17] of a material. Phase field crystal methods have been systematically advanced overt the past 20 year and have already demonstrated effective for investigating solidification of different crystal structures [3.18–3.21] and topological plasticity in the solid state [3.22–3.26]. Although originally describing only diffusive growth, recent progress has extended the hydrodynamic framework of the PFC methodology to examine phonon scattering on sub-diffusive time scales, but still longer than MD time scales [3.27–3.29]. These multi-time scale models are often said to propagate *quasi-phonons*.

This article shows the results of a novel study on phonon triggered recrystallization in two spatial dimensions. First we provide a brief overview of the phase field crystal (PFC) model, and our simulation approach. Subsequently, we illustrate three novel procedures in the context of PFC simulations that allow measurements of the intermediate scattering function, longitudinal density of states, and an approximation of the input kinetic energy. We then detail new results on the

$\rho_{\text{ref}} k_b T$	B_l	B_x	R	β_0	β_2	D	dt	dx	dy	L
1	1.0	0.98	1	0.1	$0.1 \rightarrow 1$	1	0.01	0.8502	0.9817	512

Table 3.1: List of parameters used during this investigation. L denotes the length of the square numeric grid. Qualitative units are reported, which favour the hexagonal solid phase. The numerical spacings dx and dy we chosen such that the atomic spacing, $a_o \approx 10dx$. Table is adapted from [3.30].

appearance of a Boson peak and secondary grain-boundary van Hove singularity in polycrystaline materials. Finally, we study the input of kinetic energy into polycrystalline samples, thus triggering melting, and crystallization. We propose a potential rate relation that describes the maximally achieved metastable defect-fraction (e.g. melt pools, dislocations, etc.) as a function of the input kinetic energy. We expect that the resultant mechanism explored herein are of frequent occurrence in rapid solidification processing, including in additive manufacturing, and may help elucidate current challenges with these emerging methods.

3.2 Investigation of Polycrystalline Phonon Scattering

3.2.1 Model

Phase field crystal models herald back to the work of Elder *et al.* [3.17]. Here the authors construct a pseudo Landau-Ginzburg theory for a time-averaged density field, which implicitly subsumes contributions from thermal and phonon vibrations. The model has been demonstrated to describe dynamic plasticity on the atomic scale, both qualitatively [3.18, 3.22] and quantitatively [3.24, 3.31]. The inherent anisotropy further permits studies of interface driven diffusion [3.32] and grain boundary premelting. The technique has also exhibited glassy behaviours [3.23, 3.33, 3.34], to which we shall later make connections.

The model begins by construction of an effective free energy, F, as a functional of the density field, ρ. Expanding about a uniform reference density near the transition point, ρ_{ref}, the free energy can be split into ideal gas and interaction components [3.35]. The latter of which takes the form of a series of correlations of increasing order. Expanding the ideal contribution near the

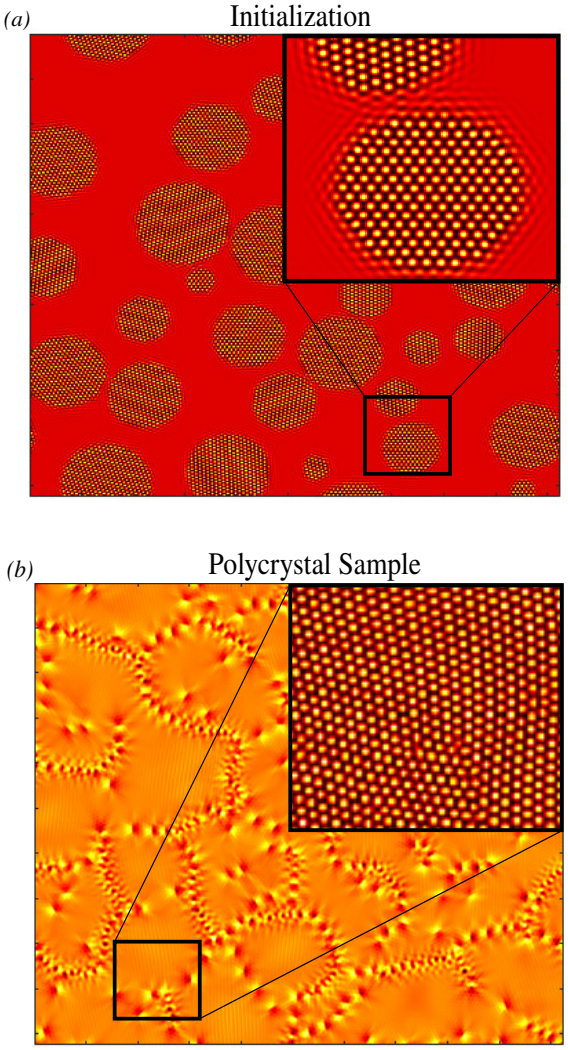

Figure 3.1: Illustration of the phase field crystal density field during polycrystalline growth on a 1024^2 simulation domain. Subpanel (a) highlights the structure after 100 time steps with an initial distribution of circular seeds. After 5000 time steps, the uniform liquid phase almost fully crystallizes and individual grains impinge on another. Subpanel (b) shows the resultant hydrostatic strain map of the impinged polycrystal, which uses the density filter introduced in appendix 3.6.1. The inset magnifies the density field of a grain-boundary region. Figure adapted from [3.30].

reference density, and keeping only contributions from the two-point correlation results in [3.36],

$$\frac{F}{\rho_{ref} k_b T} = \int_\Omega \Big[\frac{\rho^2}{2} - \frac{\rho^3}{6} + \frac{\rho^4}{12} - \frac{\rho^2}{2}(1 - B_l) + \rho B_x (R^2 \nabla^2 \rho + \frac{R^4}{2} \nabla^4 \rho) \Big], \tag{3.1}$$

where the free energy has been recast into dimensionless units by division through the Boltzmann energy scale $k_b T$ and the reference density. Here Ω refers to the simulation domain. B_x, B_l, R, are components of the assumed two-point correlation function, while B_l controls the liquid compressibility and has some intrinsic temperature dependence. Meanwhile, B_x controls the solid pressure and compressibility also has an inherent temperature dependence as described in Appendix 3.6.1. Below a certain temperature, the correlation causes the hexagonal phase of atomic length R, to be a minimum energy configuration, while at higher temperatures the systems favours the formation of a uniform density distribution. Appendix 3.6.1 describes the thermodynamic phase diagram of the model for liquid-solid coexistence. It is also noted that modifications of the two-point correlation and inclusion of higher order correlations can allow for further crystallographic phases or vapour phases [3.37, 3.38]. Additional fields can also be added to allow for description of multi-component alloys [3.20].

The dynamics of the phase field crystal density field propagate through a damped wave-like equation derived in detail in our earlier work [3.29]. This is given by,

$$\frac{\partial^2 \rho}{\partial t^2} + \beta_0 \frac{\partial \rho}{\partial t} - \beta_2 \nabla^2 \left(\frac{\partial \rho}{\partial t} \right) = D \nabla^2 \left(\frac{\delta F}{\delta \rho} \right) + \nabla \cdot \eta, \tag{3.2}$$

where gradients in the chemical potential, $\mu = \frac{\delta F}{\delta \rho}$ act as a source of both diffusive and wave-like density propagation in a solid. The mobility parameter, D is assumed constant here, though some thermal and dynamic dependencies may already be embedded in the form of the free energy attained after coarse-graining in time. The vector field η denotes a noise current representative of fast processes on the order the atomic vibrations and which have been averaged out in the free energy functional. The noise current is assumed to obey, $\langle \eta_i \rangle = 0$ and $\langle \eta_i \eta_j \rangle = \sigma \delta_{ij}$, where δ_{ij} is the Kronecker delta between vector directions i and j. This relation is in accordance with the

fluctuation-dissipation theorem where σ is on order of the thermal scale. As argued in our previous work [3.29], dissipation arising from vacancy diffusion is attributable to the β_0 term. Meanwhile the β_2 term is a novel addition to previous PFC works with phonon effects [3.27, 3.28], affecting the dissipation based on the wavevector modes of the signal, thus allowing for a description of phonon softening. The parameter β_2 may also be viewed as a phase dependent modulation to the dissipation. The additional dampening arises from temperature and phonon-phonon scattering that are evidently important for our current work. When the dissipation approaches infinity, the wave model reduces to the conventional local diffusive model. The inclusion of the first, inertial, term provides a short time scale that is important for rapid elastic relaxation in dynamics, a feature that can significantly change dislocation dynamics and the growth morphology a solid-liquid front (e.g. from planar to cellular). It is noteworthy that the full model of Reference [3.29] also included strain diffusion, which was argued to modify dislocation climb and glide timescale. This effect was also recently introduced effectively into an PFC amplitude model framework [3.39].

For simulations reported in this work we use the set of model parameters listed in Table 3.1, which also includes the numerical parameters used. We solve equation 3.2 through the pseudo-spectral method that was developed previously [3.29].

3.2.2 Polycrystalline Sample Construction

We studied phonon scattering in polycrystalline samples solidified in the phase space of the aforementioned PFC model. The construction of a polycrystalline material whose grain boundary distribution matches experiments can be quite challenging. In selective laser melting, grain structures resemble those achieved in directional solidification experiments. Depending on the rapidity of the process, grains may develop as cellular fronts, or dendritic networks that impinge. In the former scenario when the characteristics Mullins-Sekerka wavelength is large, grain sizes can be thousands of atoms large. The plasticity of such configurations is believed to be dominated by lone dislocations and geometrically necessary dislocations near cell boundaries. Meanwhile, the grain structure of crystals comprising impinged dendritic networks can be composed of many smaller high-angle nano-grain boundaries. Nano-crystalline structure is generally accompanied by va-

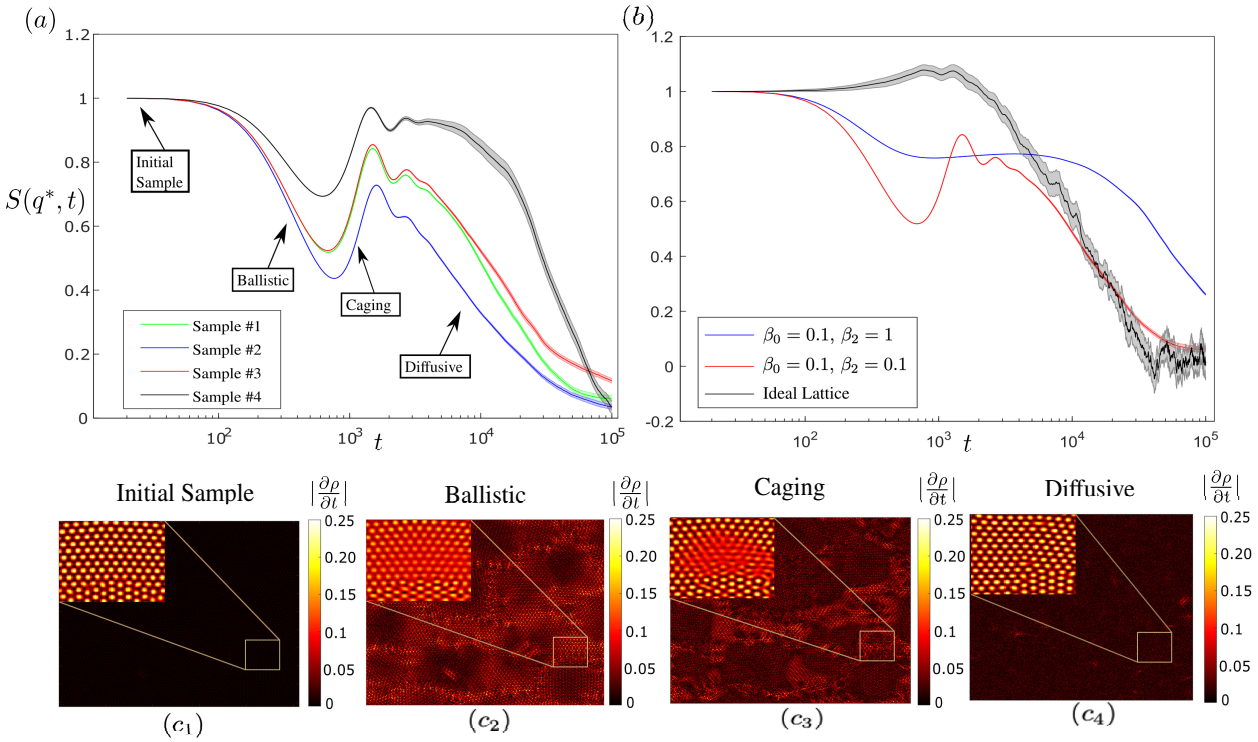

Figure 3.2: Illustrated is the dynamic structure factor, $S(q^*,t)$, measured at the reciprocal lattice wave vector q^*, as a function of time, t. Subpanel (a) shows a comparison of $S(q^*,t)$ for 4 polycrystalline samples with different initial grain size distributions. The curves are supplemented with transparent bordered region denoting the standard error attained from averaging over 10 different realizations of thermal noise ($\sigma = 0.2$). Subpanel (b) depicts the dependence of $S(q^*,t)$ with different model dissipation values. The decay behaviour of an ideal crystal is also illustrated in grey. Below, the maps of $|\frac{\partial \rho}{\partial t}|$ highlight the dynamic behaviour of samples at differing stages of evolution: initial sample, ballistic regime, β–dissipation (caging) regime, and α–dissipation (diffusive) regime, respectively. An inset is provided in each map that highlights a subsection of the density field, which was grain-boundary in the initial impinged sample. Figure adapted from [3.30].

cancy clusters [3.40], whose local thermodynamics may favour fracture or melt-pool formation. Upon recrystallization these metastable defects may cause large misorientation gradients [3.41]. We further note that unstable growth below the spinodal can also generate a plethora of metastable structures. It is noted that it is often difficult to gather ample statistics of such structures from experiments. Furthermore, the non-equilibrium extent of such structures can be challenging to ascertain.

In this work, we focus on reproducing a realistic statistical distribution of grains, with an emphasis on different misorientation grain boundaries. We constructed 50 simulation samples that were initialized with normally distributed angles, and random initial seed sizes and number. To allow for crystallization, the seeds were placed inside an undercooled liquid melt, and the system was then allowed to grow according to equation 3.2 until grain impingement. An illustration of a typical polycrystalline sample during the growth phase is shown in subpanel (a) of figure 3.1. The impingement criterion can be found by observing changes in the slope of the free energy in time. An example of one of our fully solidified polycrystalline samples is shown in subpanel (b) of figure 3.1, where a strain map is provided to highlight the dipolar character of individual dislocations that emerge after impingement. Lines of jammed dislocations separate the individual grains from another. We note that some long-range strains are found within bulks that result from the bending of slip lines. Our typical grain sizes range between 4 to 50 atoms in length. The resultant grains can subsequently be characterized through their grain-number, grain-size, strain distribution ($\langle \nabla \cdot u^2 \rangle$), and energy distribution.

3.2.3 Intermediate Scattering Function

A metric often used in incoherent neutron scattering of polycrystalline materials is the self intermediate scattering function, or dynamic structure factor, $S(q,t)$. This can be evaluated by

$$S(q,t) = \langle \tilde{\rho}_{-q,0} \tilde{\rho}_{q,t} \rangle, \tag{3.3}$$

where $\tilde{\rho}_{q,t}$ denotes the Fourier transform of the density field at wavevector magnitude q, and time t. The average, $\langle\cdot\rangle$ is performed over realizations of the thermal noise, and all radial variations of wavevectors of magnitude (q). To compare with experimental results, one would further average over crystalline configurations, though the main features are expected to be self-averaging over large enough samples.

The structure factor provides information about the nature of the crystal evolution. Berry *et al.* have previously used this metric in binary phase field crystal models, to illustrate caging in glassy undercooled melts [3.31] where a timescale competition exists between different atomic species. In such cases, the intermediate scattering function exhibits multi-stage stretched exponential relations, with additional stages resulting from the timescale of heterogeneous escape. We have found similar evidence in relation to the competition of mass and phonon motions in polycrystalline samples, as will be shown below. Namely, phonon caging results in an extension of a plateau region between the ballistic and diffusive dynamic regimes, which is often termed β-relaxation in neutron scattering experiments of glassy materials. Molecular dynamics studies conducted by Zhang *et al.* originally showed that polycrystals may share this glass-like feature [3.9]. We note that a dip prior to the β-relaxation regime has been referred in the studies of glasses to be related to the so-called Boson peak [3.42]. In the context of polycrystalline materials, the extent of the plateau may shed some light on the inherent amorphous structure of grain boundaries and defects.

Thus we measured $S(q,t)$ for the evolution of the polycrystals that we created earlier. The evolution was simulated in the presence of a large noise, $\sigma = 0.2$. This choice of noise amplitude was chosen to represent the highly non-equilibrium excitation strains that develop in a material during a large ad-hoc quench. The measured $S(q,t)$ is illustrated in subpanel (a) of figure 3.2 for a number of polycrystalline samples exhibiting similar two-time scale behaviour. The crossover behaviour between the ballistic and caging regimes was found to impacted by the amount of high wavevector dissipation, which is controlled through β_2. This is illustrated in subpanel (b) of the same figure, which also includes the structure function evolution of an idealized lattice that only contains a single decay timescale.

Subpanels (c_1-c_4) illustrate $|\frac{\partial \rho}{\partial t}|$ at different stages of the structure evolution. Here, an initial

seed (c_1) begins inactivated, subsequently releasing elastic propagations that diffuse (c_2). This *quasi-phonon* diffusion takes the density configuration away from the starting state. Although no plastic deformation is associated with this early response, the time averaged density field varies in local amplitude. The ballistic diffusion factor may then be deduced from the initial exponential decay scale seen in subpanel (a). In an idealized lattice only local amplitude fluctuations drive the system out of the starting configuration as was observed in subpanel (b). In polycrystalline materials however, a significant portion of kinetic energy and activity is limited (caged) near to the grain-boundaries, while grain bulks remain relatively unchanged. This behaviour is observed in subpanel (c_3) and constitutes the crossover regime between *quasi-phonon* diffusion and plastic diffusion. As *quasi-phonons* are depleted from the grain bulks, large density regions remain unperturbed. As a result the autocorrelation function plateaus. Meanwhile phonons scatter off and collect at sites of high energy. This allows for the formation of metastable states. In multi-component alloys, intermetallic phases may form. In our pure material system, recrystallization follows and the system grows and coarsens through mass diffusion (c_4). Rough estimates of required annealing times can be garnered from analyzing the decay scale of the dynamic structure factor.

3.2.4 Longitudinal Phonon Density of States

The rapid imparting of laser energy into a lattice can cause temperature pile-up, a property of phonon scattering and softening that contributes to the caging-regime described above. This necessitates the investigation of the spectrum of phonon frequencies and energies, which can be analyzed through the phonon density of states, $\mathscr{G}(\omega)$. Following molecular hydrodynamics [3.43], the density of states can be calculated through

$$\mathscr{G}(\omega) = \mathscr{F}_{\omega}\left[N\int_{\Omega} d^2q\langle\overrightarrow{g}(q,0)\cdot\overrightarrow{g}(q,t)\rangle S(q,t)\right], \tag{3.4}$$

where N is a normalization constant, $\overrightarrow{g}(q,t)$ is the Fourier transform of the local momentum density and $\langle\cdot\rangle$ is a thermal average as performed in the calculation of the intermediate scattering

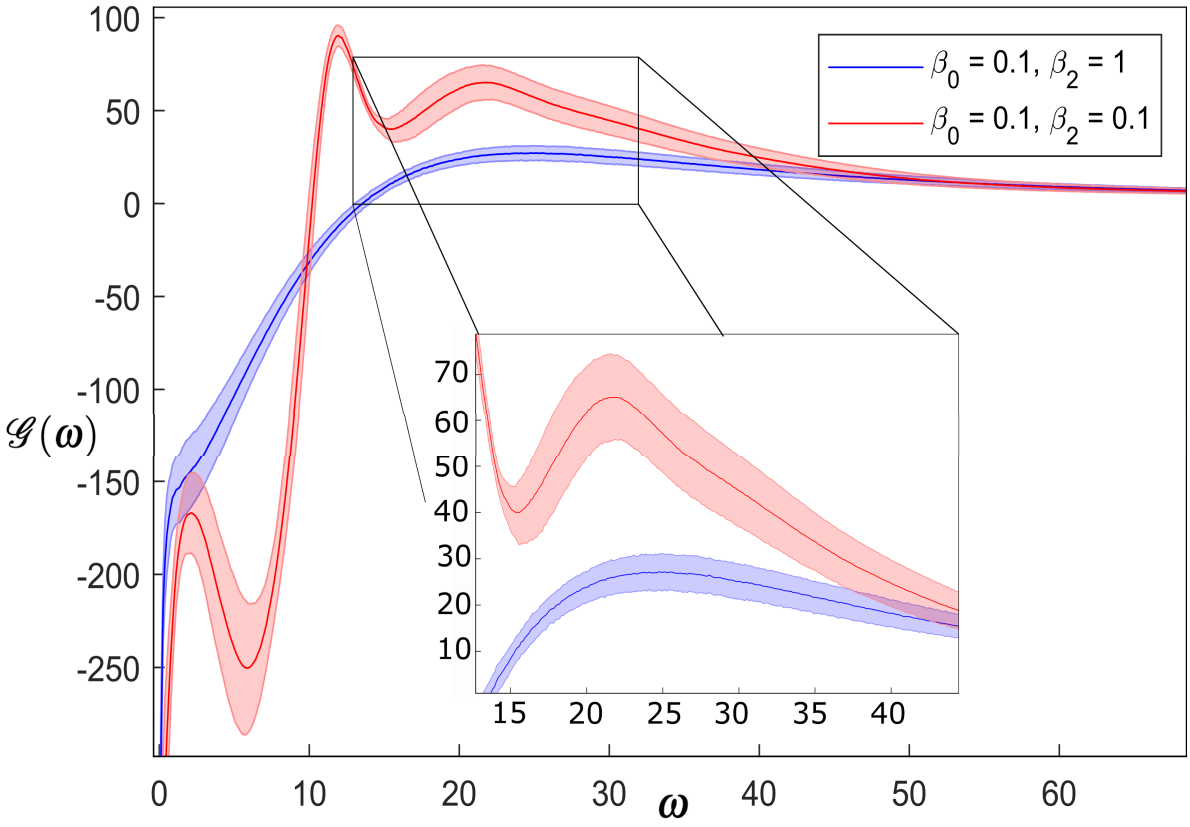

Figure 3.3: Normalized longitudinal phonon density of states for two values of β_2 dissipation. The inset focuses on the high frequency broad peak exhibited by both data sets. The frequency, ω is given in units of the inverse of the time step, dt^{-1}. As we have alluded to earlier, the negative density of states should be interpreted as a depletion of longitudinal modes. The transparent borders reflect the standard error of the measured averaged of polycrystal samples. Figure adapted from [3.30].

function $S(q,t)$. This metric is often probed in Raman spectroscopy to understand which phonons frequencies are the active energy carriers in a given process. In such studies the longitudinal and transverse momentum contributions can be separated through use of the incident polarization. The phonon density of states has remained a valuable metric in thermal conductivity optimization. Moreover, the phonon density of states can differentiate between glassy structures and pristine lattices. The reason for which is that glassy materials exhibit additional scattering and dampening, hence resulting in harmonic sets of peaks in the vibrational spectrum.

Even a qualitative assessment of the phonon density of states has remained elusive in phase field

crystal modelling, as the momentum has not been extractable. This has made the study of phonon behaviours challenging to compare to experiments. However, by making use of the Helmholtz decomposition a relation between the longitudinal momentum, $\overrightarrow{g}_l$, and $\frac{\partial \rho}{\partial t}$ can be developed. Since hydrodynamics constitutes the basis for the derivation of our dynamical model, we exploit the mass continuity equation, writing it as,

$$\begin{aligned} \frac{\partial \rho}{\partial t} &= \nabla \cdot \overrightarrow{g} \\ &= \nabla \cdot \left(\nabla \phi_{\overrightarrow{g}} + \nabla \times H_{\overrightarrow{g}} \right) = \nabla^2 \phi_{\overrightarrow{g}}. \end{aligned} \tag{3.5}$$

Here the momentum has been decomposed into longitudinal, $\overrightarrow{g}_l = \nabla \phi_{\overrightarrow{g}}$, and shear, $\overrightarrow{g}_s = \nabla \times H_{\overrightarrow{g}}$, modes. Taking the derivatives to Fourier space then permits a relation between the longitudinal component and $\frac{\partial \rho}{\partial t}$ given by

$$\overrightarrow{g}_l = \nabla \mathscr{F}^{-1} \left[\frac{\frac{\partial \tilde{\rho}}{\partial t}}{-k^2} \right], \tag{3.6}$$

where $\tilde{\rho}$ is the Fourier transform of the PFC density field. This expression can be self-consistently determined during simulations. To avoid numerical divergence, we set the $k = 0$ component of $\overrightarrow{g}_l$ to 0. The longitudinal momentum can be interpreted as coming from shock fronts released or scattered from stress sources within the bulk polycrystal. Substituting equation 3.6 into equation 3.4 and Fourier transforming in time allows for an approximate measure of the longitudinal density of states, neglecting potential cross terms between $\overrightarrow{g}_l$ and $\overrightarrow{g}_s$. We expect these contributions to be quantitatively important, but unnecessary to provide a qualitative picture of the phonon spectrum peaks.

The phonon density of states is intricate, with many frequency peaks closely distributed from one another. In a pristine lattice, Debye's theory of phonon dispersion predicts, $\mathscr{G}(\omega) \propto \omega^{d-1}$, where d is the spatial dimension. Thus it is customary to report the ratio, $\Gamma(\omega) = \frac{\mathscr{G}(\omega)}{\omega^{d-1}}$, which for a perfect crystal is expected to be constant. However, a realistic material will always exhibit some defect or metastable structures that modify the dispersion relation. As a consequence, additional peaks are found in $\Gamma(\omega)$, as illustrated in figure 3.3. This is also observed in the terahertz frequency range where additional peaks are known to result. They are likely due to the dominance

of mechanisms such as caging, scattering and softening, although the precise cause of such peaks remains a subject of debate. Some peaks may be attributed to Van Hove singularities where the dispersion relation becomes singular [3.14]. Alternatively, the Ioffe-Regel limit may be the cause of maxima, wherein phonons with wavelengths less than their mean free path experience additional dampening [3.44]. Near 1.5 THz ($\omega \approx 22dt^{-1}$ in the PFC data of figure 3.3) a broad asymmetric peak called the Boson peak has also been reported [3.12, 3.13]. Originally documented in low temperature glasses, the Boson peaks is believed to occur due to excessive phonon softening [3.12, 3.13, 3.15] and has been found to occur in higher temperature systems.

3.2.5 Variation of Input Kinetic Energy

The phonon spectrum allows a description of the shock pulses that can be induced in a polycrystal during material processing. In reference to selective laser melting, depending on the energy imparted per area (fluence), recrystallization, plastic deformation, or fracture will ensue. Here electrons become excited, distributing their excitation energy to lattice vibrations on femto- to picosecond time scale [3.6]. Local energy densities may exceed various formation energies to allow for corresponding transformations. Alternatively, shock peening processes aim to increase dislocation density resulting from the interaction of the shock with material structure. Furthermore in rolling, shock deep within the bulk is produced from the pressure imposed by the rollers. In the context of phase formations and phonon dampening, we view the energy imparted in these various processes as instantaneous, though we acknowledge that the early time behaviour may play a dominant role.

We thus model the energy imparted onto a lattice as a kinetic energy, T_l, that can be related to the laser energy via: $E_{\text{laser}} = \gamma T_l$. Here γ denotes an effective absorptivity of the crystal. This can be connected to the longitudinal momentum we determined earlier as,

$$T_l(t) = \int_\Omega dr \frac{\langle \overrightarrow{g}_l(r,t) \cdot \overrightarrow{g}_l(r,t) \rangle}{2\rho_{\text{ref}}}, \tag{3.7}$$

where T is the effective temperature of the system, and ρ_{ref} is the reference density.

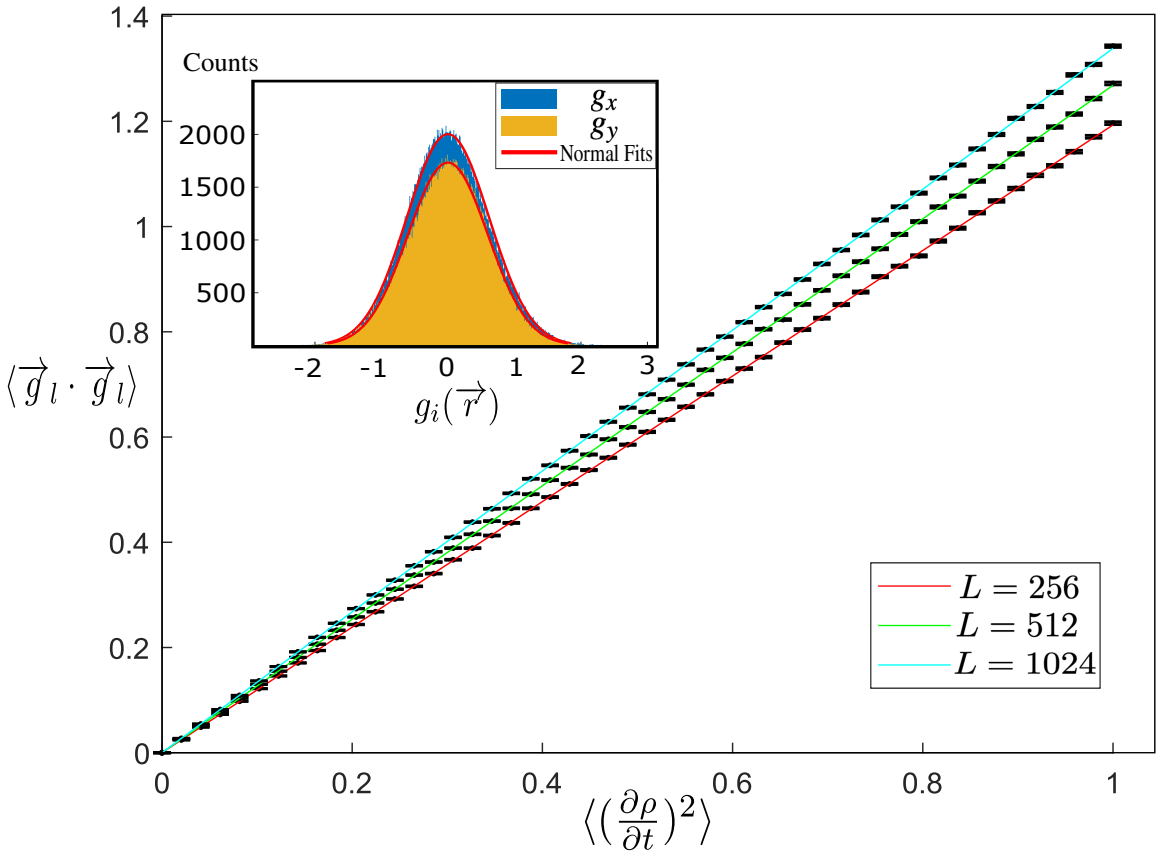

Figure 3.4: Linear relationship obtained between $\langle \overrightarrow{g}_l \cdot \overrightarrow{g}_l \rangle$ and $\langle (\frac{\partial \rho}{\partial t})^2 \rangle$ for three different system sizes. The errorbars represent averaging over 500 realizations of the initial $\frac{\partial \rho}{\partial t}$. The inset shows the distribution of momenta for the case of $\langle \left(\frac{\partial \rho}{\partial t} \right)^2 \rangle = 0.5$ ($\overrightarrow{g}_x$ and $\overrightarrow{g}_y$ are blue and orange respectively). Figure adapted from [3.30].

As a first attempt to apply equation 3.7 to phase field crystal models, we introduce momentum through a normal distribution of the initial $\frac{\partial \rho}{\partial t}$ field, with average $\langle \frac{\partial \rho}{\partial t} \rangle_r = 0$ everywhere. For a given variance, 500 realizations of $\frac{\partial \rho}{\partial t}$ were constructed on a numerical grid the same size as our simulation domain in Table 3.1 (512 x 512). We subsequently found the momentum components, $\overrightarrow{g}_x$ and $\overrightarrow{g}_y$, to be approximately normally distributed. The inset of figure 3.4 illustrates the histogram of momenta, which when fitted and averaged over realizations provides a measure of the variance $\langle \overrightarrow{g_l} \cdot \overrightarrow{g_l} \rangle$. The main part of Figure 3.4 plots the relation between input $\langle \left(\frac{\partial \rho}{\partial t} \right)^2 \rangle$ and the measured $\langle \overrightarrow{g_l} \cdot \overrightarrow{g_l} \rangle$ for three domain sizes. For the 512x512 system, we find the linear relation $\langle \overrightarrow{g_l} \cdot \overrightarrow{g_l} \rangle = 1.267 \langle (\frac{\partial \rho}{\partial t})^2 \rangle$, with reduced $R^2 = 1.00$. Here the latter fit is applicable to the simula-

tions that we report below. The above procedure provides a simple connection through equation 3.7 between $\langle(\frac{\partial \rho}{\partial t})^2\rangle$ and the input kinetic energy.

3.3 Interpretation of Results

3.3.1 Phonon Relaxation Mechanisms

Our phase field crystal simulations of polycrystal relaxation revealed a ubiquitous caging regime in the intermediate scattering function as seen in figure 3.2. That is, a multi-stage stretched exponential-like curvature. This interpretation is consistent with molecular dynamic simulations of Ni polycrystals, which found a similar two time-scale behaviour [3.9]. This glassy caging behaviour was lacking in simulations of an idealized crystal (without grain-boundaries) as is illustrated in subpanel (b) of the same figure. Our results thus suggest that grain-boundaries are the cause of the two-time scale behaviour. Thus we suspect that increasing the defect density will result in materials that further resemble their metallic glass counterparts in regards to the phonon scattering spectrum. Our observations are mainly qualitative, and would thus require a careful treatment of grain boundary energy, such as in the work done by Mellenthin *et al.* [3.45] to connect to an quantitative material. We leave the study of how changing the polycrystal grain size and grain boundary energy affect the phonon spectrum to future works.

In addition to the glassy-like properties of polycrystals, we further observe that phonon scattering results in liquid pools that suppress further ballistic scattering, and coarsen after formation. Some example videos of this process for different values of the dissipation constant (β_2) can be found in the supplementary material [3.46]. The liquid pools seem to result in ringing (Boson peak) of the dynamic structure factor during the crossover from ballistic to diffusive motion. In regards to the density field, this corresponds to a relaxation in the bulk, but energetic grain boundaries. It is noted that in the limit of substantial low-wavelength dissipation, the ringing modes are suppressed as is shown in subpanel (b) of figure 3.2 when comparing the results for $\beta_2 = 1$ and $\beta_2 = 0.1$. Furthermore, the melt pool sizes are also found to be suppressed as β_2 was increased (See supplemental videos [3.46]). The pool nucleation mechanism is likely influenced by local grain energies,

which is different for each polycrystalline sample studied. Here we have averaged over different grain-boundary energies, however further analysis of the impact of grain-boundary energies may be conducted in future works. While the melt pools appear to form on grain boundaries, they can also form along slip planes of the host lattice structure when two grain boundaries are close to one another. These liquid pools recrystallize on longer timescales than their formation, potentially annealing into dislocations. It is noteworthy that the defected regions and recrystallization zones resemble the necklace structures found in dynamic recrystallization experiments [3.47] that can lead to serrated grain boundaries. Importantly, energy is being added to the system by external mechanical deformation. The induced strain subsequently generates phonons propagating through the lattice and carry the energy to the grain boundaries. Typically, when a material is externally strained, recrystallization takes place on the grain boundary within the bulk. When the recrystallized grains are small relative to their host, the morphology resembles a necklace. As the input energy is increased, further heterogeneous nucleation takes place. In certain scenarios, the liquid pools could become highly depleted in density, where we suspect cavitation or fracture would commence. Additionally, we note in multi-component alloys, the high energetics may induce concomitant precipitation similar to the work by Medina *et al.* where energy is added through external strain loading [3.48]. These aforementioned processes thus describe a recrystallization mechanism occurring as a result of phonon caging and scattering.

Further analysis of the phonon scattering spectrum through the longitudinal phonon density of states, revealed the emergence of resonance peaks. We note that the negative density of states, should be viewed as a depletion of available sites, since we are only considering longitudinal components of the velocity. In figure 3.3 we show the longitudinal density of states averaged over 10 polycrystals for two values of β_2 that control the low wavelength phonon dissipation. In both cases, we see a peak at roughly $\omega \approx 22\, dt^{-1}$. An inset is provided expanding this region. In the case of the lower dissipation (orange), we find additional peaks at lower frequencies. In the latter case, phonons propagate further between potential sites of scattering and softening. To this extent, we believe the additional resonances are caused by the phonon scattering/softening at boundaries. This interpretation is consistent with dispersion relation calculations that suggest softening as a culprit

for low frequency peaks. Meanwhile, we suspect the high frequency peak could be a potential Boson-peak. We note however that this peak may be an artifact of the approximations that went into deriving equation 3.4. As result, further metrics to connect the high frequency peak may be necessary. In particular, low frequency shear waves may interact with the longitudinal modes. Importantly, the features of the resonance peaks are qualitatively consistent with experimental measurements of laser irradiated thin films, which are measuring the process at much shorted time scales [3.49, 3.50]. Waldecker *et al.*, further highlight the dominant activity of the longitudinal acoustic modes, such as those we have been able to measure [3.50]. More intricate hydrodynamic amplitude variants of the phase field crystal model that explicitly track the velocity vector field may also be able to elucidate the shear contributions.

3.3.2 Laser Melting

Our discussion thus far has dealt with polycrystalline lattices subjected to large thermal noise. These investigations are thus applicable to thermal annealing experiments. However in the rapid solidification encountered in processes such as additive manufacturing, energy is transferred near instantaneously from a shock. Following the procedure described in the previous section, we add an initial burst of kinetic energy, E_o, in the form of a density distribution corresponding to an initial $\langle\left(\frac{\partial\rho}{\partial t}\right)^2\rangle$. This addition represents the first attempt at describing the energy embedded in shock fronts that are found in both bulk material that are subjected to mechanical deformation [3.47] and in laser melting systems [3.51]. Subsequently we compare the defect fraction (in accordance with the thresholding method described in Appendix 3.6.2) over 10 simulations of different realizations of a fixed input energy. Additionally, our simulations were repeated over different polycrystalline configurations. The defect fraction comprised of structural defects, such as dislocations, and melt pools. The simulation is supplemented with a small noise, $\sigma = 0.01$, which accounts for rapid dynamics below the coarse graining scale of the PFC model. Figure 3.5 illustrates that an increasing input energy leads to an increasing maximal defect fraction, as measured using the procedure in Appendix 3.6.2. Subpanel (a) demonstrates the tracked defect fraction as a function of time for different input energies. Subpanels ($c_1 - c_4$) show the typical density fields at $t = 1500\Delta t$ for

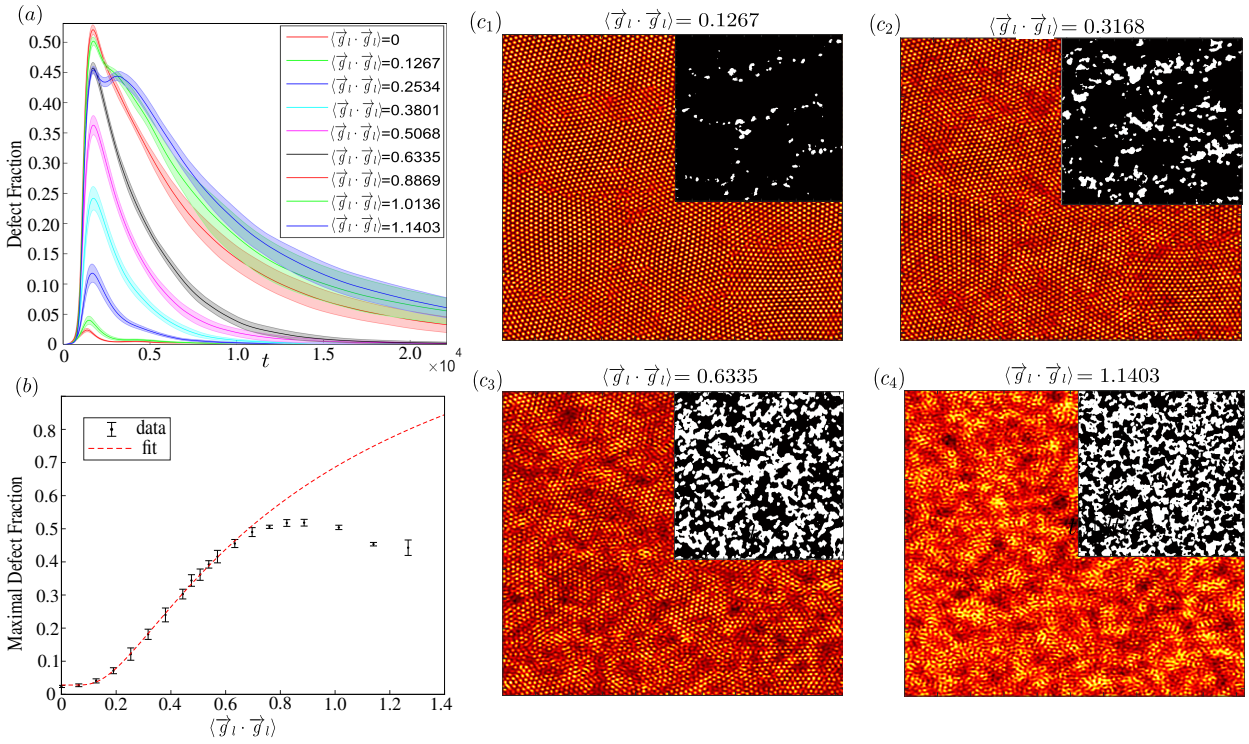

Figure 3.5: This figure highlights the response of a crystal to an initial input of kinetic energy. Subpanel (a) illustrates the defect fraction measured as a function of time, for different input energies. The associated errorbars are captured by transparent borders denoting the standard error, when averaged over different polycrystal samples. Subpanel (b) shows the maximal achieved defect fraction as a function of the input energy. Thereto we fit equation 3.8 (red line) with adjusted $R^2 = 0.9985$. Here $a_1 = 10.46$, $a_2 = 0.1051$, $a_3 = 0.6092$, and $a_4 = -10.44$. Errorbars denote the standard error measured over different polycrystal samples. Subpanels (c_1-c_4) illustrate the density field at time $1500\Delta t$ for different input kinetic energies for the same sample. The insets represent a thresholding analysis to determine the defect fraction. Figure adapted from [3.30].

different input kinetic energies, with the insets showing the defect fraction thresholding. Subpanel (b) highlights the maximally achieved defect fraction as a function of the input energy. It is noted that the defect fraction shown in the density maps as insets in Fig. 5. This metric subsumes features such as grain-boundaries, dislocations, and metastable liquid zones, all of which are created due to the stress/strain imparted by the input laser energy. We observe that these all serve as templates from which subsequent recrystallization occurs in the sample. In that sense, we are seeing both traditional mechanisms of recrystallization caused by stress/strain in the solid state [3.3], but also predicting novel mechanisms such as local recrystallization arising from metastable liquid/amorphous pools. Such mechanisms are expected to be ubiquitous in shocked materials, excited by laser irradiations [3.51, 3.52].

In analogy to the metastable Ostwald ripening curves [3.53], we attempt to describe defect nucleation rate through rate relation considerations. In this scenario, the energy dissipates roughly exponentially in time, $E_{in}(t) \approx E_o e^{-bt}$, with b dependent on the dampening in equation 3.2. Once an energy threshold has been reached, melt pools are found to form at defect sites and along slip lines of the crystal in relation to our earlier results. This qualitative morphology is in further corroboration with the necklace structures described above, We argue that the liquid pools have a substantial amount of energy buried in their solid-liquid interfaces. Thus we make the approximation that the volume of a given melt pool is proportional to boundary energy. We thus make the conjecture,

$$\begin{aligned} \frac{\partial E_{\text{boundary}}}{\partial t} &= \Gamma_+ - \Gamma_- \\ &= e^{-\frac{E_A}{E_o e^{-bt}}} E_{\text{boundary}} - \Gamma_{\text{Thermodynamic}}, \end{aligned} \tag{3.8}$$

where $\Gamma_+ = e^{-\frac{E_A}{E_{in}}} E_{\text{boundary}}$ represents the energy absorption rate expected to occur uniformly across the boundary. Here E_A denotes an effective activation energy for melt-pool growth. As a result of the metastability of the melt-pools, a thermodynamic restoring force that disperses interfaces is introduced through Γ_-, which is taken here as a constant. Equation 3.8 can be solved in

the limit of $b << 1$ to yield,

$$E_{\text{boundary}}(t) \approx C_1 e^{te^{-\frac{E_A}{E_{in}}}} + \Gamma_{\text{Thermodynamic}} e^{\frac{E_A}{E_{in}}}. \tag{3.9}$$

The integration factor C_1 includes an energy dependence that needs be determined. We then determine the time, $t_{\max}$, at which the boundary energy is maximized. This is achieved by setting equation 3.8 to zero, and performing a Taylor-expansion of equation 3.8 for small t. Recasting the equation 3.9 results in the approximate form,

$$E_{\text{boundary}}(t_{max}, E_o) \approx a_1 e^{a_2 e^{-\frac{a_3}{E_o}}} + a_4. \tag{3.10}$$

Here, a_i are the coefficients of our kinetic theory. Note that a_3 has dimensions of energy, and may be viewed as an effective activation energy to form metastable structures. The relation is expected to be independent of spatial dimension. However, we expect the boundary absorptivity to deviate as a result of the dislocation dimensionality. We have only aim here to describe the maximally achieved defect fraction subjected to an energy burst in the sample. To further account for healing and coarsening, $\Gamma_{\text{Thermodynamics}}$ may be extended to include energy and time dependence. We leave such a study for future work. We also note that equation 3.10 only accounts for a single phase transformation. In multi-phase studies (e.g. precipitation, void, etc.) equation 3.8 may be supplemented by additional activation energy terms.

We fit equation 3.10 to the maximal defect fraction extracted from the data of figure 3.5(a). The results are shown in 3.5(b). The results suggest are consistent with the above analytical theory for low input energies. It is noted that equation 3.8 represents a rather crude approximation of the system, since grain boundary structure, density segregation, fracture nucleation, and temperature effects can also impact the resultant curve. In particular, our analytical theory poorly predicts the high energy regime where a secondary defect peak is found to emerge in the simulation data of figure 3.5(a), which we believe is a result of the thresholding used to determine the defect fraction. In particular, this is because the high energy density fields (subpanel c_4) are found to be highly amorphous and not accounted by the thresholding. We note that phase field crystal models may

breakdown at this high energy limit as other structures such as metallic glass or fracture may form. To this end, future work may extend our study to multi-component materials following Ofori *et al.* [3.20]. Alternatively, fracture may be treated through the introduction of a vapour phase as in the work of Frick *et al.* [3.38]. We expect that the trends reported here are expected to be true independent of spatial dimension. However, a more quantitative validation of our results with experiments may also require the inclusion of latent heat to extend the theory to account for consistent coarsening time-scales. Nonetheless, we have illustrated in this work that laser induced recrystallization should include a pathway involving heterogeneous nucleation from nano-liquid pools found at high energy grain-boundaries.

3.4 Summary

In this article we have used PFC modelling with two-time scale dynamics (MPFC) to examine phonon excitation in polycrysatlline nanomaterials. In particular, we have investigated the dynamic structure factor of a polycrystalline material subjected to multi-time scale dynamics. In comparison to the single exponential decay of an idealized lattice, polycrystals are found to exhibit a two step decay process, commonly exhibited by glasses. A caging regime is found that results from phonon softening and is affected by the amount of high wavelength dissipation. Phonon accumulation was also found to result in the formation of metastable melt-pools. We have also performed the first analysis of the longitudinal phonon density of states with phase field crystal models. Herein we uncovered multiple peaks that emerge from phonon scattering and a broad peak, which is potentially relatable to the Boson-peak. As we have described, a more detailed investigation of the phonon scattering properties may be explored through use of hydrodynamic coupled phase field crystal models that explicitly evolve a velocity field.

Our phonon relaxation studies were then used to investigate the rapid transfer of energy into polycrystalline materials, and their subsequent relaxation and recrystallization. We found that increasing input energy resulted in an increase of the defect density and the formation of liquid pools. We developed a simple theory to describe the maximally achieved defect fraction as a

function of input energy. At low energies our results are in a agreement with the theory. Thus our work suggests that early stage shock-induced recrystallization is dominated by the formation of melt-pools. Future experimental work may be performed to assess the validity of our theory. Owing to the density depleted pools, high input energies are further expected cause cavitation and fracture, or nucleation of other metastable structures. Such processes may be the topics of future studies with the use of multi-component models or vapour phase models.

3.5 Acknowledgements

We thank Prof. Bradley Siwick for stimulating discussions. We thank NSERC (Natural Sciences and Engineering Research Council of Canada) and *le Fonds de recherche du Quebec—Nature et technologies* for funding support. Additionally, we thank Calcul Québec and the Digital Research Alliance of Canada for computing resources.

3.6 Appendix

3.6.1 Phase Diagram

The phase field crystal model is built as an expansion of the free energy about the liquidus for the study of solidification. For the details, we refer the reader to the work of Provatas *et al.*[3.36]. Here an effective temperature is varied through the parameters B_l or B_x that enter into equation 3.1. To understand the preferential selection of crystalline order versus uniform liquid state, it is customary to make a one-mode expansion of the density,

$$\rho(r) = \overline{\rho} + \Sigma_{G_j} A_{|G_j|} e^{iG_j \cdot r}. \tag{3.11}$$

The parameter $\overline{\rho}$ represents the uniform average density adopted by the liquid phase. A_{G_j} are the amplitudes centered about the reciprocal lattice vectors G_j, which act as order parameters of the crystal's translational symmetry. Substitution of equation 3.11 into 3.1 and subsequent integration

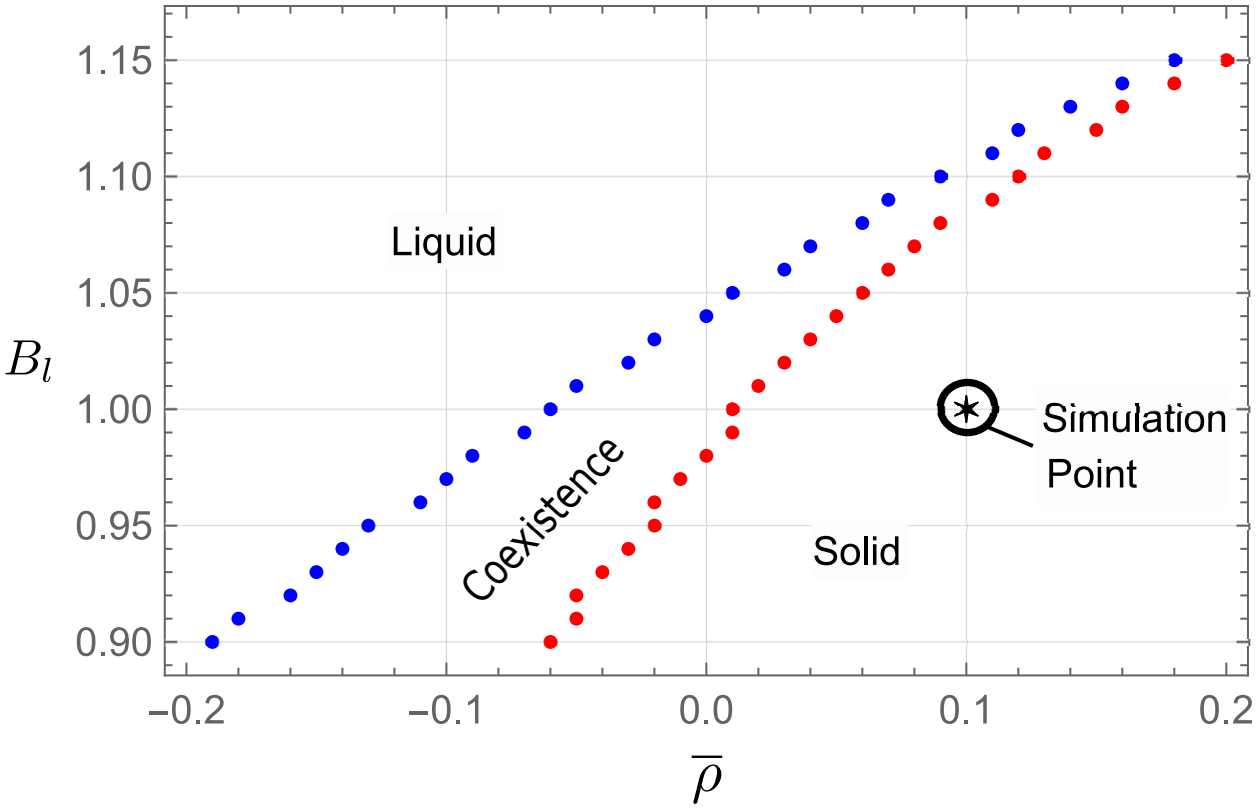

Figure 3.6: This figure illustrates the phase diagram obtained through a one-mode ansatz of the equilibrium crystal structure. The corresponding stable phase region is as denoted. The star denotes the phase state used for our study. Figure adapted from [3.30].

over a unit cell represents the approximate bulk free energy. All further free parameters, such as A_{G_j} and R, would need to be minimized. The solutions of which enumerate the bulk free energies of the thermodynamic phases. We emphasize that this expansion is an ansatz of the minimal energy states, which in generality should be verified through numeric simulation.

One may then solve the condition of phase coexistence:

$$\mu_1 = \mu_2 \tag{3.12a}$$

$$f_1 - \overline{\rho_1}\mu_1 = f_2 - \overline{\rho_2}\mu_2. \tag{3.12b}$$

Here $\mu_i = \frac{\delta F}{\delta \rho}$ is the chemical potential and $\overline{\rho_i}$ coexistence density associated to phase i. Although explicit calculation of the above relations is possible, one can also make use of a convex hull

algorithm of the free energy as detailed by Seymour *et al.* in their thesis[3.54]. Repeating the calculation at different temperatures results in a phase diagram as illustrated in figure 3.6. The highlighted points denote the temperatures and density used throughout this paper.

3.6.2 Imaging Methods

The density field carries large amounts of information in the Fourier modes. One can analyze the deviations from the mode expansion form of equation 3.11 to extract specific information about interface structures. As introduced in earlier work, the strain field can be extracted from

$$\nabla \cdot u \approx \mathscr{F}^{-1}\left[k\exp\left\{-\frac{k^2}{\sigma_0}\right\}\mathscr{F}\left[\rho\mathscr{F}^{-1}\left[(k-|G|)\exp\left\{\frac{-(k-|G|)^2}{\sigma_0}\right\}\mathscr{F}[\rho]\right]\right]\right], \tag{3.13}$$

where $\mathscr{F}$ denotes the Fourier transform operator. We use this filter not only for visualization of dislocations, but also as a metric for the dislocation density of a given polycrystal. The inset of Figure 3.1 shows and example of this filter.

We also make use of,

$$\mathscr{F}^{-1}\left[e^{-\frac{k^2}{\sigma_0}}\mathscr{F}[|\rho|]\right] \approx \overline{\rho}^2 + |A_G|^2, \tag{3.14}$$

which combined with thresholding allows for a rough characterization of the local phase. Our studies of defect fraction utilized a $\sigma_0 = 0.3$. The thresholding entailed summing the number of pixels with density values above 0.3 and subsequent division by the total pixel number. To our knowledge this type of approach was first described by Kocher *et al.* [3.55], when attempting to coarse-grain the phase field crystal model to a single order parameter.

3.6.3 Finite Size Analysis

Since our simulations are performed on a two-dimensional periodic domain, wave attenuation needs to be ensured to occur on scales larger than the system size. To ensure that peaks detected

with the density of states were not artifacts of finite size effects, we performed additional simulations on numerical grids with lengths 256 and 1024 grid points. We refer the reader to the supplemental material for videos of the process [3.46]. We found that the system size had negligible affect on the melting and recrystallization behaviour described throughout this work, nor on the presence of phonon softening that resulted in two time-scale dynamics.

3.7 Bibliography

[3.1] F.J. Humphreys and M. Hatherly. "Chapter 4 - The Structure and Energy of Grain Boundaries". In: *Recrystallization and Related Annealing Phenomena (Second Edition)*. Ed. by F.J. Humphreys and M. Hatherly. Second Edition. Oxford: Elsevier, 2004, pp. 91–119. ISBN: 978-0-08-044164-1. DOI: 10.1016/B978-008044164-1/50008-6.

[3.2] C. M. Sellars and J. A. Whiteman. "Recrystallization and grain growth in hot rolling". In: *Metal Science* 13.3-4 (1979), pp. 187–194. DOI: 10.1179/msc.1979.13.3-4.187.

[3.3] S. Gao et al. "Recrystallization-based grain boundary engineering of 316L stainless steel produced via selective laser melting". In: *Acta Materialia* 200 (2020), pp. 366–377. ISSN: 1359-6454. DOI: 10.1016/j.actamat.2020.09.015.

[3.4] F. C. Pinto et al. "Recrystallization in non-conventional microstructures of 316L stainless steel produced via laser powder-bed fusion: effect of particle coarsening kinetics". In: *Journal of Materials Science* 57 (27 2022), pp. 9576–9598. ISSN: 1573-4803. DOI: 10.1007/s10853-021-06859-1.

[3.5] U. Andrade et al. "Dynamic recrystallization in high-strain, high-strain-rate plastic deformation of copper". In: *Acta Metallurgica et Materialia* 42.9 (1994), pp. 3183–3195. ISSN: 0956-7151. DOI: 10.1016/0956-7151(94)90417-0.

[3.6] B. J. Siwick et al. "An atomic-level view of melting using femtosecond electron diffraction". en. In: *Science* 302.5649 (2003), pp. 1382–1385.

[3.7] M. I. Arefev, M. V. Shugaev, and L. V. Zhigilei. “Kinetics of laser-induced melting of thin gold film: How slow can it get?” In: *Science Advances* 8.38 (2022), eabo2621. DOI: 10.1126/sciadv.abo2621.

[3.8] F. Demmel. “Slow structural relaxation process facilitates solidification in liquid gallium”. In: *Physical Review B* 101 (1 2020), p. 014207. DOI: 10.1103/PhysRevB.101.014207.

[3.9] H. Zhang et al. “Grain boundaries exhibit the dynamics of glass-forming liquids”. In: *Proceedings of the National Academy of Sciences of the United States of America* 106 (16 2009), p. 77357740. DOI: 10.1073/pnas.0900227106.

[3.10] D. G. Cahill et al. “Nanoscale thermal transport”. In: *Journal of Applied Physics* 93.2 (2002), pp. 793–818. ISSN: 0021-8979. DOI: 10.1063/1.1524305.

[3.11] B. Golding and J. E. Graebner. “Echo Phenomena in Disordered Solids”. In: *Phonon Scattering in Condensed Matter*. Ed. by H. J. Maris. Boston, MA: Springer US, 1980, pp. 11–20. ISBN: 978-1-4613-3063-9. DOI: 10.1007/978-1-4613-3063-9_2.

[3.12] S. Ren et al. “Boson-peak-like anomaly caused by transverse phonon softening in strain glass”. In: *Nature Communications* 12 (1 2021). ISSN: 2041-1723. DOI: 10.1038/s41467-021-26029-w.

[3.13] M. González-Jiménez et al. “Understanding the emergence of the boson peak in molecular glasses”. In: *Nature Communications* 14.1 (2023), p. 215. ISSN: 2041-1723. DOI: 10.1038/s41467-023-35878-6.

[3.14] S. N. Taraskin et al. “Origin of the Boson Peak in Systems with Lattice Disorder”. In: *Physical Review Letters* 86 (7 2001), pp. 1255–1258. DOI: 10.1103/PhysRevLett.86.1255.

[3.15] M. Baggioli and A. Zaccone. “Unified theory of vibrational spectra in hard amorphous materials”. In: *Physical Review Research* 2 (1 2020), p. 013267. DOI: 10.1103/PhysRevResearch.2.013267.

[3.16] A. Zaccone and M. Baggioli. “Erratum: Unified theory of vibrational spectra in hard amorphous materials [Phys. Rev. Research 2, 013267 (2020)]”. In: *Physical Review Research* 4 (2 2022), 029001(E). DOI: 10.1103/PhysRevResearch.4.029001.

[3.17] K. R. Elder and M. Grant. “Modeling elastic and plastic deformations in nonequilibrium processing using phase field crystals”. In: *Physical Review E* 70 (5 2004), p. 051605. DOI: 10.1103/PhysRevE.70.051605.

[3.18] K. R. Elder et al. “Phase-field crystal modeling and classical density functional theory of freezing”. In: *Physical Review B* 75 (6 2007), p. 064107. DOI: 10.1103/PhysRevB.75.064107.

[3.19] M. Greenwood, N. Provatas, and J. Rottler. “Free Energy Functionals for Efficient Phase Field Crystal Modeling of Structural Phase Transformations”. In: *Physical Review Letters* 105 (4 2010), p. 045702. DOI: 10.1103/PhysRevLett.105.045702.

[3.20] N. Ofori-Opoku et al. “Multicomponent phase-field crystal model for structural transformations in metal alloys”. In: *Physical Review B* 87 (13 2013), p. 134105. DOI: 10.1103/PhysRevB.87.134105.

[3.21] Z. Wang et al. “Control of phase ordering and elastic properties in phase field crystals through three-point direct correlation”. In: *Physical Review E* 105 (4 2022), p. 044802. DOI: 10.1103/PhysRevE.105.044802.

[3.22] J. Berry, K. R. Elder, and M. Grant. “Melting at dislocations and grain boundaries: A phase field crystal study”. In: *Physical Review B* 77 (22 2008), p. 224114. DOI: 10.1103/PhysRevB.77.224114.

[3.23] J. Berry and M. Grant. “Modeling Multiple Time Scales during Glass Formation with Phase-Field Crystals”. In: *Physical Review Letters* 106 (17 2011), p. 175702. DOI: 10.1103/PhysRevLett.106.175702.

[3.24] J. Berry et al. “Defect stability in phase-field crystal models: Stacking faults and partial dislocations”. In: *Physical Review B* 86 (22 2012), p. 224112. DOI: 10.1103/PhysRevB.86.224112.

[3.25] P. Stefanovic, M. Haataja, and N. Provatas. “Phase field crystal study of deformation and plasticity in nanocrystalline materials”. In: *Physical Review E* 80 (4 2009), p. 046107. DOI: 10.1103/PhysRevE.80.046107.

[3.26] V. Skogvoll, M. Salvalaglio, and L. Angheluta. “Hydrodynamic phase field crystal approach to interfaces, dislocations, and multi-grain networks”. In: *Modelling Simulation Material Science and Engineering* 30 (8 2022), p. 084002. DOI: 10.1088/1361-651X/ac9493.

[3.27] P. Stefanovic, M. Haataja, and N. Provatas. “Phase-Field Crystals with Elastic Interactions”. In: *Physical Review Letters* 96 (22 2006), p. 225504. DOI: 10.1103/PhysRevLett.96.225504.

[3.28] S. Majaniemi and M. Grant. “Dissipative phenomena and acoustic phonons in isothermal crystals: A density-functional theory study”. In: *Physical Review B* 75 (5 2007), p. 054301. DOI: 10.1103/PhysRevB.75.054301.

[3.29] D. Burns, N. Provatas, and M. Grant. “Time-scale investigation with the modified phase field crystal method”. In: *Modelling Simulation Material Science and Engineering* 30 (6 2022), p. 064001. DOI: 10.1088/1361-651X/ac7c83.

[3.30] D. Burns, N. Provatas, and M. Grant. “Two-dimensional phase field crystal simulation of laser-induced recrystallization: A mechanism of grain-boundary phonon scattering and softening”. In: *Physical Review Materials* 7 (8 2023), p. 083402. DOI: 10.1103/PhysRevMaterials.7.083402.

[3.31] J. Berry and M. Grant. “Phase-field-crystal modeling of glass-forming liquids: Spanning time scales during vitrification, aging, and deformation”. In: *Physical Review E* 89 (6 2014), p. 062303. DOI: 10.1103/PhysRevE.89.062303.

[3.32] Z. Chen et al. “Phase-field crystal simulation facet and branch crystal growth”. In: *Applied Physics A* 124.5 (2018), p. 385. ISSN: 1432-0630. DOI: 10.1007/s00339-018-1800-5.

[3.33] S. Abdalla et al. “Thermodynamics, formation dynamics, and structural correlations in the bulk amorphous phase of the phase-field crystal model”. In: *The Journal of Chemical Physics* 157.16 (2022). 164502. ISSN: 0021-9606. DOI: 10.1063/5.0114705.

[3.34] M. Vasin and V. Ankudinov. “Competition of glass and crystal: Phase-field model”. In: *Mathematical Methods in the Applied Sciences* n/a.n/a (2023). DOI: https://doi.org/10.1002/mma.9207.

[3.35] Y. Singh. “Density-functional theory of freezing and properties of the ordered phase”. In: *Physics Reports* 207.6 (1991), pp. 351–444. ISSN: 0370-1573. DOI: 10.1016/0370-1573(91)90097-6.

[3.36] “Phase Field Crystal Modeling of Pure Materials”. In: *Phase-Field Methods in Materials Science and Engineering*. John Wiley & Sons, Ltd, 2010. Chap. 8, pp. 167–208. ISBN: 9783527631520. DOI: https://doi.org/10.1002/9F783527631520.ch8.

[3.37] G. Kocher and N. Provatas. “New Density Functional Approach for Solid-Liquid-Vapor Transitions in Pure Materials”. In: *Physical Review Letters* 114 (15 2015), p. 155501. DOI: 10.1103/PhysRevLett.114.155501.

[3.38] M. J. Frick, E. Wilson, and N. Provatas. “Consistent representation of vapor phases in phase field crystal dynamics”. In: *Physical Review Materials* 7 (2 2023), p. 023405. DOI: 10.1103/PhysRevMaterials.7.023405.

[3.39] K. Wang et al. “Exploring atomic mechanisms of microstructure evolutions in crystals under vacancy super- or undersaturation states by a kinetic amplitude-expanded phase-field-crystal approach”. In: *International Journal of Plasticity* 157 (2022), p. 103386. ISSN: 0749-6419. DOI: 10.1016/j.ijplas.2022.103386.

[3.40] M. Hillert, M. Schwind, and M. Selleby. “Trapping of vacancies by rapid solidification”. In: *Acta Materialia* 50.12 (2002), pp. 3285–3293. ISSN: 1359-6454. DOI: 10.1016/S1359-6454(02)00150-7.

[3.41] T. Pinomaa et al. “Multiscale analysis of crystalline defect formation in rapid solidification of pure aluminium and aluminium–copper alloys”. In: *Philosophical Transactions of the Royal Society A: Mathematical, Physical and Engineering Sciences* 380.2217 (2022), p. 20200319. DOI: 10.1098/rsta.2020.0319.

[3.42] C. A. Angell et al. “Relaxation in glassforming liquids and amorphous solids”. In: *Journal of Applied Physics* 88.6 (2000), pp. 3113–3157. ISSN: 0021-8979. DOI: 10.1063/1.1286035.

[3.43] S. L. Seyler and C. E. Seyler. “Molecular hydrodynamic theory of the velocity autocorrelation function”. In: *The Journal of Chemical Physics* 159.5 (2023), p. 054108. ISSN: 0021-9606. DOI: 10.1063/5.0153649.

[3.44] Y. M. Beltukov et al. “Boson peak and Ioffe-Regel criterion in amorphous siliconlike materials: The effect of bond directionality”. In: *Physical Review E* 93 (2 2016), p. 023006. DOI: 10.1103/PhysRevE.93.023006.

[3.45] Jesper Mellenthin, Alain Karma, and Mathis Plapp. “Phase-field crystal study of grain-boundary premelting”. In: *Physical Review B* 78 (18 2008), p. 184110. DOI: 10.1103/PhysRevB.78.184110.

[3.46] See Supplemental Material at Supplemental for a set of simulation videos.

[3.47] D Ponge and G. Gottstein. “Necklace formation during dynamic recrystallization: mechanisms and impact on flow behavior”. In: *Acta Materialia* 46.1 (1998), pp. 69–80. ISSN: 1359-6454. DOI: https://doi.org/10.1016/S1359-6454(97)00233-4.

[3.48] S. F. Medina. “Determination of precipitation–time–temperature (PTT) diagrams for Nb, Ti or V micro-alloyed steels”. In: *Journal of Materials Science* 32.6 (1997), pp. 1487–1492. ISSN: 1573-4803. DOI: 10.1023/A:1018562202876.

[3.49] L. Waldecker, R. Bertoni, and R. Ernstorfer. “Compact femtosecond electron diffractometer with 100 keV electron bunches approaching the single-electron pulse duration limit”. In: *Journal of Applied Physics* 117.4 (2015), p. 044903. ISSN: 0021-8979. DOI: 10.1063/1.4906786.

[3.50] L. Waldecker et al. “Electron-Phonon Coupling and Energy Flow in a Simple Metal beyond the Two-Temperature Approximation”. In: *Physical Review X* 6 (2 2016), p. 021003. DOI: 10.1103/PhysRevX.6.021003.

[3.51] M. M. Budzevich et al. “Evolution of Shock-Induced Orientation-Dependent Metastable States in Crystalline Aluminum”. In: *Physical Review Letters* 109 (12 2012), p. 125505. DOI: 10.1103/PhysRevLett.109.125505.

[3.52] V. Zhakhovsky et al. “Shock-induced melting and crystallization in titanium irradiated by ultrashort laser pulse”. In: *arXiv preprint arXiv:2306.09100* (2023).

[3.53] C. Sagui, D. S. O’Gorman, and M. Grant. “Nucleation and growth: Decay of a metastable state”. In: *Physical Review E* 56 (1 1997), R21–R24. DOI: 10.1103/PhysRevE.56.R21.

[3.54] M. Seymour. *Study of multi-point interactions in PFC models for complex structural transformations*. McGill University (Canada), 2018.

[3.55] G. Kocher and N. Provatas. “Thermodensity coupling in phase-field-crystal-type models for the study of rapid crystallization”. In: *Physical Review Materials* 3 (5 2019), p. 053804. DOI: 10.1103/PhysRevMaterials.3.053804.

Chapter 4

Temperature Coupling

To date, phase field crystal models have remained largely isothermal. However, many experimental configurations are open systems. As a result temperature can escape. Furthermore solidification is associated to a reduction of entropic degrees in freedom that are released as heat. In connection to our earlier observations, the large local energies can shift the phase diagram or reduce solidification growth velocity. In addition, temperature gradients are known to induce thermal stresses, which have the potential to cause of material fracture as well as secondary phase transformations within a material. The following chapter is subsequently aimed at introducing the energy diffusion equation into the MPFC formulation, along with a self-consistent description of latent heat production. As a consequence, our method captures the heat release from phase changes, phonon scattering and lattice fluctuations. In particular, we aim to illustrate that temperature increase can be limited and coupled to both density and vacancy diffusion.

Two Dimensional Phase Field Crystal Study of Thermo-Density Coupling: Thermal Expansion, Recalescence, and Plasticity

Duncan Burns, Nikolas Provatas, Martin Grant

Abstract

In this article we present a thermal coupling to a recently published two-time scale phase field crystal model (MPFC) to describe latent heat contributions of systems undergoing rapid phase transformations. We call this formulation *Temperature Field Crystal* (TFC), which permits the study of coupled density, vacancy and temperature field dynamics at the length-scale of atomic ordering. Following a derivation of the new thermo-density coupled MPFC model, several physical properties of the model are demonstrated. We reproduce the thermo-density interface profiles encountered in the steady state solidification growth limit. We further illustrate the existence of a vacancy concentration inherent in the phase field crystal amplitude. It is shown that with a frozen thermal gradient, of the form often used in directional solidification studies, a vacancy gradient is established along with an associated thermal stress. In particular, we show that within the isochoric limit of the model, effects of thermal expansion are incorporated through the change of amplitude with respect to temperature, rather than by increasing the equilibrium lattice length. The TFC model is then applied to the study of select solidification processes. It is shown that the release of latent heat during recalescence is accompanied by a change in the average thermal pressure. Moreover, we illustrate, for the first time that modulations of the recalescence curve can be indicative of plastic deformation, dislocation activity, and phonon scattering. Notably, the temperature evolution may be used as a marker for the grain distribution attained from nucleation following a system quench.

4.1 Introduction

Solids are in part characterized by their translation and rotation symmetry. The inherent structure differentiates solids from disordered thermodynamic phases, such as liquids and amorphous materials. Ordering can greatly affect global thermodynamic properties, or response behaviours. Individual phases of matter may be represented by minima of a free energy landscape. However, the kinetic pathway connecting them is by caveat out-of-equilibrium. In particular, the dynamical evolution of modes describing the transition between phases is tied to the different energy transportation mechanisms that operate at distinct length- and time-scales. The competition of energy pathways for energy relaxation, leads to the emergence of a wide set of phenomena such as caging [4.1, 4.2] and banding [4.3, 4.4], to mention a few.

Besides their interesting physics, non-equilibrium phase transformations are also of paramount importance to particular materials manufacturing processes, such as splat quenching, hot rolling of solids, and laser remelting and solidification. Here, the presence of large input energies can greatly alter the state of base material, leading to its subsequent transformation into phases comprising zones of frustration or defected microstructures. At low impart energies, a solid elastically deforms, sending oscillations through the lattice that dissipate energy gradients. However, at higher fluences, the lattice bonds break apart, producing dislocations and melt pools, which can recrystallize into inter-metallic or glassy phases, or even voids or cracks. Fine control of the material properties can be gained from increasing the density and nature of such thermally driven defects. As a concrete example, consider splat cooling, where the extreme solidification rates trap excess vacancies [4.5] and solute [4.6], which can lead to the formation of precipitates or metastable structures during coarsening. Another example occurs during hot rolling, where the induced strains on a metal sheet are so extreme as to lead to numerous recrystallization pathways to relieve the input strain energy [4.7]. The explosive interest in additive manufacturing in recent yeas has been largely due to the ability to form complex defect microstructures during solidification. In each scenario described above, the control of nanostructure is tantamount, and affects material properties.

The multi-scale nature of non-equilibrium phase transitions also makes their study challeng-

ing. Some information may be garnered from spatial and auto-correlation functions of the density and velocity as are measured in neutron scattering or electron microscopy techniques. Unfortunately such experiments are limited by spatial and temporal resolution, often only allowing atomic scale visibility in post-mortem measurements. The lack of complete theory and set of high resolution videos thus necessitates the development of computational models and simulation to probe the dominant dynamic behaviour of the growth, while also providing governing equations for key variables describing a process in a particular phenomenon. The multi-scale nature of most materials processes makes development of a comprehensive theory intractable. However, much can be gleaned from simplified theories retain the salient features of a dynamical phase transformations describing microstructure formation. This is done by exploiting time- and length-scale cutoffs, thus separating the dominant transport variables from that of the assumed self-averaging background.

Numerous simulation methods have been utilized to analyze microstructure growth behaviour at differing time- and length-scales fundamental to specific processes of interest. At the scale of individual atoms, while retaining atomic vibration resolutions, molecular dynamics techniques are used [4.8]. However, this resolution places limitations on the length and time scales accessible in simulations due to computational complexity. Continuum models are thus used to study longer length and times scales of crystal growth at the cost of neglecting the shorter length spatial regimes. One approach is through sharp interface models that contain an effective description of an interfaces through appropriate moving boundary conditions [4.9, 4.10]. For example, the local shift in free energy due to curvature requires the application of the Gibbs-Thomson interface curvature correction. At the intermediate scale between sharp interface models and molecular dynamics is the phase field (PF) technique. PF models are continuum field theories that carry some internal structure in the interface, but self consistently recover sharp-interface constraints on scales where the inverse curvature is larger than the interface thickness [4.11]. However, any process emergent at the atomic scale, such as elasticity, plasticity, grain boundaries are not inherently and self-consistently captured by traditional phase field models.

Plasticity has a topological nature and can be incorporated into a continuum model by encoding in it the propensity for orientational ordering, as is done in phase field crystal (PFC) models. Such

methods propagate a coarse-grained density field, which can be used to observe elastic distortion [4.12] and dislocation dynamics [4.1]. Recent interest in phase field crystal methods has in part been due to the rich interplay between crystal plasticity and microstructure evolution during solidification and solid precipitation, caused by the large amounts of energy that can be stored in a material during processing, as discussed above. While traditional phase field (PF) and phase field crystal (PFC) models are limited to dynamics on diffusional time scales, they have also been extended through various hydrodynamic approximations to account for multiple time scales, which also makes them amenable to the study of interface trapping [4.13], as well as *quasi-phonon* propagation [4.14–4.16].

Most phase field crystal (PFC) modelling studies have, to date, largely assumed immediate energy transfer to an infinite bulk solid. Subsequently the models are treated as isothermal. This leads, among other things, to temperature being treated as isothermal throughout a material. However, this approximation becomes inadequate for describing rapid processes, ranging from rapid solidification [4.17] to crystal plasticity [4.18, 4.19]. A self-consistent coupling of density to heat transport in PFC modelling can allow for a new modelling paradigm for investigating the important role of spatio-temporal temperature variations on rapid solidification, thermally-mediated stresses and plasticity within materials.

There have been some notable works that have attempted to couple the PFC modelling approach to heat transport [4.20–4.22]. In the work of Kocher *et al.*, thermal-density coupling was designed such as to produce latent heat at an advancing solidification front in a Model C type fashion [4.23, 4.24]. Such considerations were sufficient to capture basic recalescence phenomena. Wang *et al.* advanced the topic by making efforts to correct the temperature dependence of the free energy to ensure concavity of the free energy with respect to temperature [4.21]. Punke *et al.* have since expanded this formulation to include an explicit temperature dependence to the ideal lattice spacing and showed differing dendritic morphologies when crystal were subjected to large thermal expansion strains [4.22].

In this work, we use the hydrodynamics of mass, momentum and energy conservation to derive a novel phase field crystal (PFC) formulation that will be shown to couple vacancy and strain

diffusion encoded in the density field to thermal transport. For simplicity of reference, we coin the PFC paradigm that emerges from our derivation as the *temperature field crystal (TFC)* framework as its main feature is to incorporate into PFC a mechanism for describing energy transport due to vacancy diffusion, strain and latent heat of structural changes, all of which emerge from the model's thermo-density coupling. Following the derivation of TFC, we proceed to illustrate enthalpy changes during solidification and how they account for the latent heat release, demonstrating that phonons carry a portion of this energy through the bulk solid. We compare simulations of dendritic growth to the classical sharp interface predictions of a thermally controlled dendrite growth [4.25]. In particular, we measure the interface velocity and illustrate the recovery of the analytic exponential decay profile of the temperature. Following this, we show that when working in a constant volume, the phase field crystal free energy naturally accounts for thermal expansion, through temperature variations of the pressure. To this end, we use the TFC model to simulate the dynamics of a crystal within a region of imposed heating and chilling at its boundaries. The established temperature gradients are shown to be accompanied by a vacancy gradient contained in the density field amplitude magnitude. As another demonstration of TFC, we show that recalescence during solidification is accompanied by a corresponding pressure rise within the material. Within this context, we also demonstrate decalescence, the reduction of temperature when heating a solid to above the melting point. Finally, we end this work by highlighting the relation between recalescence and plasticity, *i.e* a process whereby dislocation annihilation forms new bonds that release a latent heat into the solid, thereby resulting in asymmetric recalescence curves. Our results indicate that temperature rate measurements can be used as a marker for nucleated grain distributions, annealing, and phonon activity.

4.2 Preliminaries

4.2.1 Modified Phase Field Crystal model

The phase field crystal (PFC) modelling treats a material as a continuum defined through a *periodic* order parameter ψ, which simultaneously allows for the thermodynamics representation of

both homogeneous phases (liquid and gas) or atomically structured (solids) phases [4.12]. This parameter is related to the time-averaged local material density through, $\rho = \rho_{\text{ref}}(1+\psi)$, which is convenient for defining quantities in terms of the perturbation of the local density ρ away from a reference point ρ_{ref}. In PFC modelling, the free energy $F[\psi]$ is functionally expanded around the liquid density at a given reference temperature. The expansion is designed to be minimized (under appropriate constraints) by either a homogeneous phase ($\psi \to 0$), a state with an ordered lattice structure ($\psi \neq 0$), or both (coexistence). More recently, PFC free energies have been introduced that can distinguish between two homogeneous phases, thus allowing for the representation of vapour-liquid-solid phases [4.26, 4.27]. The PFC density has also been coupled one or more solute fields for the investigation of binary alloys [4.28], whose dynamics now contains equations of motion for the total density coupled to that of each solute [4.29]. In this work, we will derive our formalism for thermo-density coupling for a single component (i.e. pure) material defined by a single density field ψ.

Motivation for the form of the free energy has been taken from the density functional theory of freezing [4.30]. When expanding around a high temperature liquidus point, the free energy can be split into two contributions. Namely, a non-interacting ideal gas component and an expansion in n-point density-density correlations, C_n. The minimal form of the free energy is generally taken to C_2. Here,

$$\tilde{\mathscr{F}} = \frac{F}{T} = \rho_{\text{ref}} k_B \int_\Omega d^2 r \Big[A(T) + \lambda(T)\psi + \frac{\psi^2}{2} - \frac{\psi^3}{6} + \frac{\psi^4}{12} - \frac{\psi}{2}(C_2 * \psi) \Big], \tag{4.1}$$

where $k_b T$ denotes the Boltzmann thermal scale and Ω the spatial domain. In isothermal models, $\lambda(T)$ is generally set to 0, whereby the ψ^2, ψ^3, ψ^4 prefactors are correspondingly modified [4.31]. Here we include this linear contribution to ensure concavity of the free energy with respect to temperature. Meanwhile, the function $A(T)$ is a placeholder function for all temperature dependencies independent of density, This function includes the thermal de Broglie wavelength component of the ideal gas free energy and comprises corrective factors to the liquid free energy. We note that in

isothermal model variants, $A(T)$ is often taken 0.

In the work of Elder *et al.*, the correlation function is expanded in gradients, $\overline{C}_2(k) = (1 - B_l + 2B_x k^2 - B_x k^4)$ [4.12]. Here B_l and B_x are relatable to the liquid and solid bulk moduli respectively, holding some inherent temperature dependence. Depending on the value of B_l and B_x, a hexagonal structure or uniform phase may minimize Eq. 4.1. In 4.9.1 we detail the thermodynamics of the system and build the associated phase diagram. For describing more exotic crystal structures, the Fourier transform of C_2 can be represented by a sum of Gaussians centered at the relevant wavevector [4.32]. Each of the correlation function descriptions act on a coarse-grained density field. As a result, atomic profiles in the solid state have breadth accounting for rapid lattice vibrations, which differentiates the correlations from the true density correlation function. In this sense, the correlation form contains additional rapid kinetic energy considerations in combination with the entropic and stress energy contributions.

Microstructure dynamics in PFC modelling represents a "flow" of the ψ field through the free energy landscape built into the functional F. This flow is guided through a dynamical equation that, in its simplest form, operates on diffusive time scales and preserves total system mass and allows for. More complex variants of PFC dynamics also couple diffusive flow to hydrodynamics to capture shorter time scales, leading to a linear two-time scale dynamical equation coined the *modified phase field crystal* model [4.16],

$$\frac{\partial^2 \psi}{\partial t^2} + \beta \left[\frac{\partial \psi}{\partial t} \right] = D T_{\text{ref}} \nabla^2 \left(\frac{\delta \tilde{\mathscr{F}}}{\delta \psi} \right) + \nabla \cdot \eta, \tag{4.2}$$

where gradients of the chemical potential, $\mu = \delta F / \delta \psi$ act as a driving current of the wave-like dynamics. It is noted that in expanding the free energy around a reference state, we tacitly make the approximation $F(T) \approx T_{\text{ref}} \tilde{\mathscr{F}}$ in Eq. 4.1, in order to ensure linearity of Eq. 4.2. Although this approximation has the potential to limit the state space explored, we expect that around the reference temperature T_{ref} heat transfer properties will be correctly captured. It is emphasized, however, that in all subsequent uses of the free energy (thermodynamic analyses or dynamical equations), we employ the dimensional form $F = T \mathscr{F}$. Eq. 4.2 produces *quasi-phonons* from

sources of high local energy that diffuse with scale, D and experience dissipation in accordance with $\beta = \left[\beta_0 - \beta_2 \nabla^2\right]$. The gradient nature of β accounts for the different scattering experienced by different wavelength lattice oscillations, with ∇^2 being the minimal contribution necessary to account for the sudden drop-off of the longitudinal dispersion relation. The assumed self-averaging background fluctuations are captured through η in accordance with fluctuations-dissipation where $\langle \eta_i \rangle = 0$ and $\langle \eta_i \eta_j \rangle = \sigma \delta_{ij}$. In the case of diffusive dynamics $\left(\beta \to \infty \text{ and } D/\beta \approx \mathscr{O}(1)\right)$; here phonon propagation is subsumed into the fluctuations. Furthermore, we note that Eq. 4.2 is consistent with the global density conservation symmetry. It is also noteworthy that Eq. 4.2 contains strain-vacancy flow, as shown in [4.2].

For this work, the free energy encapsulated in the correlation function is of primary focus. This free energy contribution is then associated to entropic, stress, and rapid vibrational sources. Thereto, we associate an effective temperature, T. The slow (non self-averaging) kinetic energy is meanwhile captured in the inertial propagation inherent in Eq. 4.2. This description is not dissimilar from two-temperature models that are used to describe rapid laser melting, for which we describe more details later. it is noted that evolution solely through Eq. 4.2 with free energy of Eq. 4.1 assumes instantaneous bulk energy transfer upon destruction of the atomic bonds. In this approximation, the system is treated as infinite in extent thus the bulk acts as an energy sink. Here, we will specifically investigate the dynamics described above coupled to the flow of heat in terms of the temperature, T.

4.2.2 Hydrodynamics of Solids

In a previous publication we have shown that hydrodynamics can be utilized to arrive at kinetic equations describing a time averaged density field with *quasi-phonon* ballistics, with Eq. 4.2 a limiting case [4.16]. These effective phonons propagate at artificially low velocities, but sufficient to capture phenomena resulting from time scale differences, such as trapping [4.2] and dislocation annihilation velocities [4.33]. The waves mediate the interaction between sources of stress with an inherent dissipation from scattering mechanisms that are averaged over. The dynamics encapsulated in Eq. 4.2 conserve both the mass and momentum. Eq. 4.2 assumes constant temperature,

applicable in the limit of rapid thermal equilibration to a infinite reservoir. To account for temperature flux, we use the framework of hydrodynamics to account for fast competitive flows in density, momentum *and local energy*, with corresponding transport coefficients. It is expected that so coupling these three fields will be sufficient to capture crossover phenomena associated with energy relaxation from atomic to the mesoscale. An important topic to which the model can subsequently be used is in investigation of rapid solidification phenomena.

We start our derivation from the set of hydrodynamic equations used by Cohen *et al.* [4.34, 4.35], wherein vacancy concentration is incorporated as a separate thermodynamic variable alongside the strain in the solid. The resultant dynamic equations for the conservation of mass density (ρ), momentum density ($\mathbf{g}$) and energy density (ε), combined with strain ($\overleftrightarrow{u}$) flow, are given by

$$\frac{\partial \rho}{\partial t} = -\nabla \cdot \mathbf{g}, \tag{4.3a}$$

$$\frac{\partial \mathbf{g}}{\partial t} = -\eta \nabla \overleftrightarrow{\sigma} + \nu \nabla \nabla \mathbf{g}, \tag{4.3b}$$

$$\frac{\partial \varepsilon}{\partial t} = \frac{-(\varepsilon + P)}{\rho_{\text{ref}}} \nabla \cdot \mathbf{g} + D_T \nabla^2 \phi + \alpha_T \nabla^2 T, \tag{4.3c}$$

and

$$\frac{\partial \overleftrightarrow{u}}{\partial t} = -\frac{1}{\rho_{\text{ref}}} \nabla \mathbf{g} + D_v \nabla \nabla \phi + \nabla \frac{D_T}{T} \nabla T, \tag{4.3d}$$

where only diagonal components transport coefficients are considered. The first order contributions, such as the viscosity (ν), act as an approximation of scattering mechanisms that lead to an isotropic diffusion. Aside from dissipation, The momentum is primarily driven by the stress tensor, $\overleftrightarrow{\sigma}$. In the energy equation, P, α_T, and D_T refer to the pressure, thermal diffusivity, and a thermodiffusion transport coefficients respectively. The strain dynamics have a back-coupling to the thermodiffusion factor, D_T, describing a movement of vacancies in response to temperature gradients. The last equation also includes the time averaged vacancy diffusion factor D_v. Following Cohen, we define ϕ as as the variation of energy with strain under the assumption of constant density *i.e.* an effective vacancy stress. 4.9.2 makes an explicit connection between the ϕ and the

vacancy chemical potential that was introduced in our previous work [4.16].

For simplicity we take only the diagonal components of the transport coefficients. Thus, our approximation is limited to the presence of shear propagation modes. It is noted that shear waves are believed to be a contributor to massive deformation, such as in the formation of martensitic steels. Some of the time scale differences can be accounted for by suppression of the transport coefficients in equations 4.3a-4.3d. A potential avenue to further include these features is through additional order parameter as has been associated with the hexatic phase [4.36]. Future work may entail the extension of the methods herein to amplitude phase field crystal variants [4.37].

To proceed, we postulate the usual coarse-grained relation between density, vacancy concentration and strain [4.38], i.e.,

$$\delta\rho = -\delta c - \rho_{\text{ref}}\nabla\cdot\mathbf{u}, \tag{4.4}$$

where $\text{Tr}\overleftrightarrow{u} = -\nabla\cdot\mathbf{u}$. Through Eq. (4.4), the strain evolution Eq. 4.3d may be recast into a vacancy diffusion equation. In particular, substitution of 4.4 into 4.3d results in,

$$\frac{\partial c}{\partial t} = D_v\nabla^2\phi - D_T\frac{\nabla T\cdot\nabla T}{T^2}, \tag{4.5}$$

which expresses that vacancy flow is governed by gradients in the vacancy stress (constant density) and temperature. As mentioned, the transport coefficient D_T is the vacancy thermodiffusion factor, and the ratio D_T/D_v has in past been denoted by the Ludwig-Soret coefficient [4.39], which has been measured for a variety of materials [4.40–4.42]. More recently, the thermodiffusion factor has been posited as a mechanism for hydrogen blistering in systems with large temperature gradients, such as in the exhaust pipes of nuclear plants [4.43].

4.3 Formulation of a Heat Transport Equation with PFC Coupling

In this section, we use the equations in the last subsection to derive an energy equation that couples to the PFC density field. Rearranging Eq. 4.5 for ϕ and using Eq. 4.4, allows to re-write Eq. 4.3c

for the energy dynamics in a way that is explicitly independent of the vacancy stress, ϕ, i.e.,

$$\frac{\partial \varepsilon}{\partial t} = \frac{-(\varepsilon + P)}{\rho_{\text{ref}}} \nabla \cdot \mathbf{g} + \frac{D_T}{D_v} \frac{\partial \rho}{\partial t} + \alpha_T \nabla^2 T - \frac{D_T^2}{D_v} \frac{\nabla T \cdot \nabla T}{T^2}. \tag{4.6}$$

Here $\varepsilon + P$, denotes the enthalpy density h, whose connection to latent heat has been described by Kadanoff *et al.* [4.44]. This latent heat contribution is imperative to recover/enforce the Clausius-Clapeyron relation. It will also be shown that in addition to the usual heat release due to order changes, this enthalpic contribution to the latent heat also ascribes a heat of formation for dislocations and amorphous material phases. These features can be then explored in the context of bond breaking and bond formation.

We next express Eq. 4.6 in terms of temperature, T, and free energy, F, using the thermodynamic relations

$$\varepsilon = -T^2 \frac{\delta}{\delta T} \left[\frac{F}{T} \right], \tag{4.7a}$$

and

$$p = (1 + \psi) \frac{\delta F}{\delta \psi} - f, \tag{4.7b}$$

where f denotes the free energy density, i.e., the integrand of Eq. 4.1 (multiplied by $k_B T \rho_{\text{ref}}$). We note then that large simplification can be made by using chain rule to express $\partial \varepsilon / \partial t$. Since our free energy depends on the temperature, T, and order parameter, ψ, we have,

$$\frac{\partial \varepsilon}{\partial t} = -T \frac{\delta^2 F}{\delta T^2} \frac{\partial T}{\partial t} - \frac{\delta F}{\delta \psi} \frac{\partial \psi}{\partial t} \tag{4.8}$$

We note that at equilibrium, the prefactor, $-T \delta^2 F / \delta T^2$, represents the isochoric heat capacity. When including solute transport in the framework additional chemical potential factors would appear in Eq. 4.8, consistent with the math encountered in phase field modelling [4.45].

Combining Eqs. 4.6 and 4.8, we arrive at the simplified form,

$$\left(-T\frac{\delta^2 F}{\delta T^2}\right)\frac{\partial T}{\partial t} = \left(h-\mu+T\frac{\partial \mu}{\partial T}+\frac{D_T}{D_v}\right)\frac{\partial \psi}{\partial t} + \alpha_T \nabla^2 T - \frac{D_T^2}{D_v}\frac{\nabla T\cdot\nabla T}{T^2} \tag{4.9}$$

Thermodynamic stability requires that $\delta^2 F/\delta T^2 < 0$, for the simultaneous increase of temperature and energy. We note that this condition enforces temperature evolution, which softens the presence of interfaces.

For a system at the coexistence temperature T_M, undergoing a phase transformation, the Clausius-Clapeyron relation is expected to hold. Under such a constraint, $\partial\psi/\partial t \approx \Delta\psi/\tau$, where $\Delta\psi$ denotes the density change upon the transition and τ is the timescale of the process. At the transition point, the temperature will not vary, hence

$$\left(h-\mu+T\frac{\partial \mu}{\partial T}+\frac{D_T}{D_v}\right)\Bigg|_{\text{coexistence}} = 0$$

since $\partial\Psi/\partial t \neq 0$. Furthermore, $\mu_{\text{liquid}} = \mu_{\text{solid}}$, a statement of chemical equilibrium. Subsequently we may write,

$$L = \Delta h = -T_M \frac{\partial \mu}{\partial T}\Bigg|_{\text{coexistence}}, \tag{4.10}$$

where L is the latent heat of fusion. Eq. 4.10 is a representation of the Clausius-Clapeyron relation in the $\mu - T$ plane and used in the seminal work of Mullins *et al.* to estimate the capillary length [4.46].

4.3.1 Specialization to the PFC Free Energy

To specialize the above density-coupled heat transfer equations in Eq. 4.9 to the case of solidification, we substitute the free energy in Eq. 4.1, and expand the derivative expressions involving the free energy in Eq. 4.9 in terms of the density and temperature. We walk through some of the details next.

We first evaluate the mobility component, which yields,

$$\begin{aligned}\frac{\delta^2 F}{\delta T^2} = k_B \rho_{\text{ref}} \Bigg[& 2\frac{\partial A(T)}{\partial T} + T\frac{\partial^2 A(T)}{\partial T^2} \\ & + \left(2\frac{\partial \lambda(T)}{\partial T} + T\frac{\partial^2 \lambda(T)}{\partial T^2}\right)\psi \\ & - \psi\frac{\partial C_2}{\partial T} * \psi - T\frac{\psi}{2}\frac{\partial^2 C_2}{\partial T^2} * \psi \Bigg].\end{aligned} \tag{4.11}$$

Here the model assumes a temperature dependence in the coefficients *and* the two-point correlation, C_2. In the work by Kocher *et al.* [4.20] it is assumed that all the temperature dependence is in the correlation function (i.e., $A(T) = \lambda(T) = 0$), which leads to a bulk heat capacity that is constant and vanishing at the reference density. In particular, for certain density ranges the previous formulation of Kocher *et al.* may violate the thermodynamic stability condition, $\delta^2 F/\delta T^2 < 0$. It is noted that Wang *et al.* make the approximation that $A(T) = \theta \log(T/T_o)$, which arises from the ideal gas thermal de Broglie wavelength. Such a factor can also be used to shift the heat capacity, and obeys the above concavity condition.

The latent heat contribution on the left hand side of Eq. 4.9 can also be expanded, yielding,

$$\begin{aligned}h - \mu + T\frac{\partial \mu}{\partial T} = & k_b T \rho_{\text{ref}} \Bigg[T\left(\frac{\psi}{2} - 1\right)\frac{\partial C_2}{\partial T} * \psi \\ & + T(1-\psi)\frac{\partial \lambda(T)}{\partial T} - T\frac{\partial A(T)}{\partial T} \\ & - \left(1 + \frac{\psi}{2}\right) C_2 * \psi \Bigg]\end{aligned} \tag{4.12}$$

Substituting Eqs. 4.11 and 4.12 into Eq. 4.9 can finally be used to construct a heat transport equation in terms of an arbitrary phase field crystal (PFC) two-point correlation interaction kernel. Although in this work we will restrict our attention to the basic gradient correlation kernel developed by Elder *et al.*, other forms can also be used, such as those leading to more complex crystalline lattices [4.32]. Moreover, other forms of the free energy can be substituted into the above formalism, such as those suitable for multiple phases [4.26, 4.27].

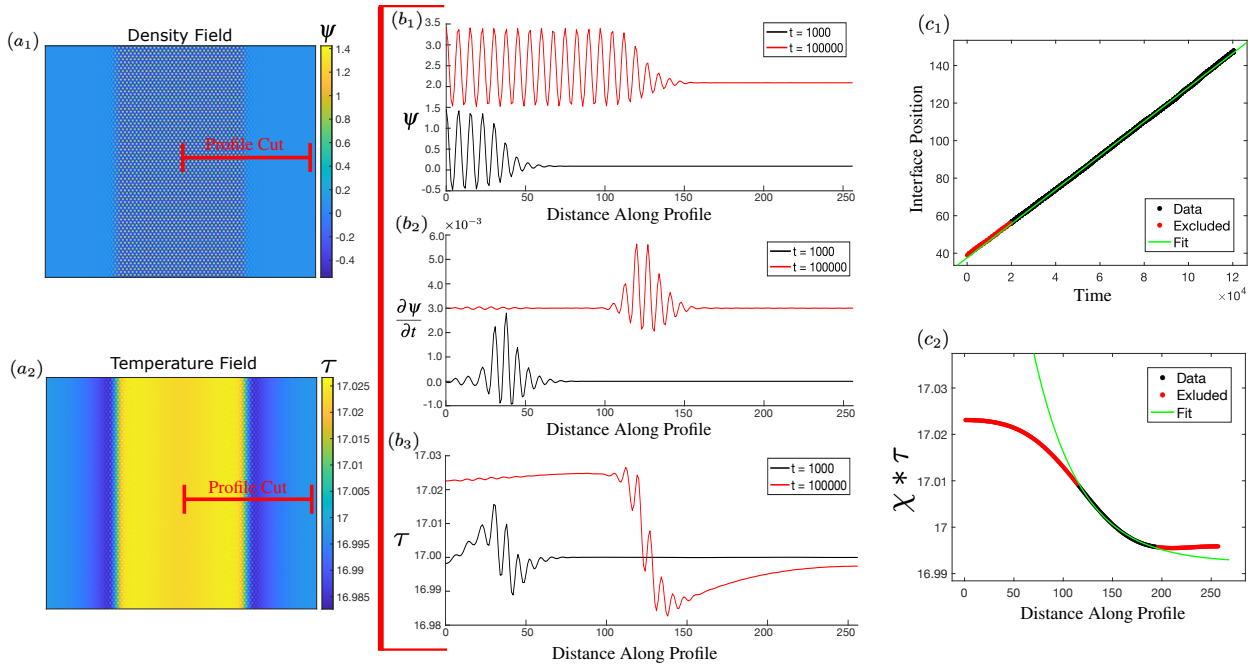

Figure 4.1: Growth of a planar solidification of an initialized stripe of solid placed in an undercooled melt. Subpanel (a_1 and a_2) show the evolving density and temperature fields at $t = 100000$, respectively. Subpanels b_1 - b_3 highlight one dimensional profiles cuts along the red line denoted in a_1 and a_2. Two instances in time are shown of the density (b_1), the velocity (b_2) and temperature (b_3), with the $t = 100000$ profiles shifted vertically for clarity. The interface position is tracked as a function of time in subpanel (c_1). A linear fit of the interface positions is performed between 2×10^4 and 12×10^4 to estimate the steady state growth velocity. Subpanel c_2 fits the exponential decay region of the smoothed temperature profile for comparison against Eq. 4.18. We list the simulation parameters used in Tables 4.1 and 4.2.

4.3.2 Reduction to a Minimal Model: The Temperature Field Crystal (TFC) Model

It is instructive to distill a minimal model from Eqs. 4.9-4.12. To do so we use the gradient correlation kernel introduced by Elder *et al.*,

$$\overline{C}_2(k) = (1 - B_l(T) + 2B_x k^2 - B_x k^4), \tag{4.13}$$

where B_l and B_x control the bulk moduli of the disordered and ordered phases, respectively. We illustrate this connection in more detail in 4.9.1. For the sake of simplicity, we make the approximation that the liquid bulk modulus is weakly temperature dependent according to

$$B_l(\tau) \approx -B_l^0 + B_l^1 \tau, \tag{4.14}$$

where $\tau = T/T_{\text{ref}}$ is a dimensionless temperature parameter. In doing so, the bulk modulus can be viewed as expanded around a reference temperature corresponding to the reference density of the liquidus around which the free energy was expanded. Here it will be assumed that $B_l^1 > 0$ and $B_l^0 > 0$, which is consistent with Singh *et al.* who examined a wide variety of thermomechanical properties of liquid metals [4.47]. This is further consistent with past density functional theory derivations of phase field crystal models [4.31]. Meanwhile, we shall also make the assumption that B_x is independent of temperature. We note that although B_x is independent of temperature, the solid bulk modulus still retains temperature dependence in accordance with 4.9.1.

The additional temperature dependencies $A(T)$ and $\lambda(T)$ added into the free energy in Eq. 4.1 can be obtained by expansion from the ideal gas contribution [4.48]. Each such component will be proportional to $\log(\rho_{\text{ref}}\Lambda_T)$, where Λ_T is the thermal de Broglie wavelength. We thus make the approximation,

$$A(\tau) \approx A^0 - A^1 \tau, \tag{4.15}$$

and

$$\lambda(\tau) \approx \lambda^0 - \lambda^1 \tau, \tag{4.16}$$

These linear forms are only expected to hold quantitatively within a narrow temperature region, but can still be relatively good approximations for reasonably chosen A^i and λ^i. These forms also allow for the additional flexibility for better approximating the disorder phase energy. We choose the parameters $A^i > 0$ and $\lambda^i > 0$ in accordance with the thermodynamic stability criteria and thermomechanical properties listed in Appendix 4.9.1.

In summary, by making the substitutions of Eqs. 4.13-4.16 into the simplified form 4.9 we

arrive at the following final form of the TFC temperature equation to couple to the PFC density equation:

$$\begin{aligned}
&\mathscr{M}_T(\psi,\tau)\frac{\partial\tau}{\partial t} = \alpha_T\nabla^2\tau - \frac{D_T^2}{D_v T_{\text{ref}}}\frac{\nabla\tau\cdot\nabla\tau}{\tau^2} \\
&+ T_{\text{ref}}\tau\Bigg[\lambda^0 - A^0 - \frac{1}{2}(1+A^0)\psi^2 - 2\lambda^1\tau + 2A^1\tau \\
&+ \Bigg(-A^0 + \lambda^1\tau + 2B_l^1\tau + B_x(2+\psi)\nabla^2 \\
&+ B_x\left(\frac{1+\psi}{2}\right)\nabla^4\Bigg)\psi\Bigg]\frac{\partial\psi}{\partial t} + \mathscr{M}_T(\psi,\tau)S(\mathbf{x},t),
\end{aligned} \tag{4.17}$$

where $\mathscr{M}_T(\psi,T) = \tau\left[2A^1 + 2\lambda^1\psi - B_l^1\psi^2\right]$. Here $S(\mathbf{x},t)$ has been added as a time dependent temperature source function, which may act locally to represent an external heat source. Eq. 4.17, in conjunction with the PFC dynamical Eq. 4.2, comprise a coupled set of evolution equations that are propagated iteratively in time. To solve the above thermo-density coupled TFC model, We use explicit Euler time-stepping to propagate the temperature field in Eq. 4.17 in conjunction with semi-implicit pseudospectral methods for the density field, the details of which are found in our earlier work [4.16].

4.4 Application to Steady-State Solidification

In this section, we test that the temperature field crystal (TFC) model can correctly capture the meso-scale physics of heat transport across a solidifying front. In the review by Langer on interface driven instability patterning, the one-dimensional steady state temperature profile of a planar interface is found analytically [4.25], in terms of the dimensionless temperature, $u = (T - T_M)/(c_P L)$. Here T_M refers to the melting temperature, c_P to the isobaric heat capacity and L denotes the latent heat, which is assumed constant across the interface. The steady profile for an interface moving at

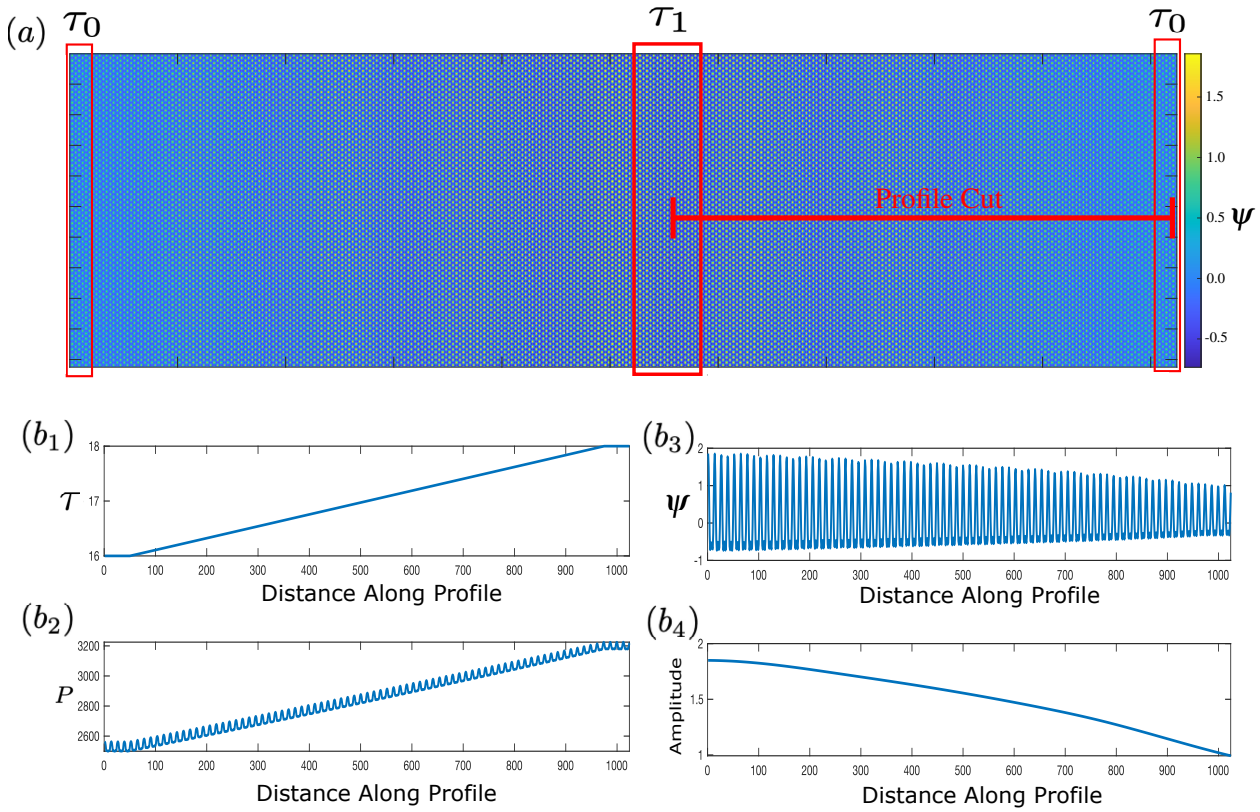

Figure 4.2: An idealized crystalline lattice is allowed to relax subjected to constant temperature regions imposed in the sample at the locations shown in subpanel (a). Along the indicated red line, the temperature, pressure, density, and density wave amplitude magnitude are presented in (b_1), (b_2), (b_3), and (b_4) respectively. The amplitude magnitude was extracted through a spline connecting peaks of the density field. The simulation parameters used are listed in Tables 4.1 and 4.2 (noting that we use units throughout where $k_B \rho_{\text{ref}} T_{\text{ref}} = 1$, as shown in Table 4.1).

velocity v was found to obey,

$$u(z) = \begin{cases} \exp\left(-2\frac{z}{l_{D_T}}\right) - 1, & \text{if } z \geq 0 \\ 0, & \text{else,} \end{cases} \tag{4.18}$$

where z denotes the distance into the liquid phase with origin positioned at the solid-liquid interface. The thermal length, $l_{D_T} = D_T / v$, sets the exponential decay scale of the temperature into the liquid. Here D_T denotes the thermal diffusivity, which can be approximated via, $D_T = \alpha_T / \bar{\mathscr{M}}_{\mathscr{T}}$ (where the overbar denotes the mean value). Since, u is proportional to T, we should expect the

exponential decay of the steady state temperature profile to be identical to the dimensionless temperature field in Eq. 4.18. We thus simulate our TFC model with aim to recover the consistent temperature decay scale given by, l_{D_T}. We note that while sharp interface theories and traditional phase field models typically assume a constant latent heat release, in reality, we expect higher-order non-uniformity in the latent heat released due to density variations across the solid-liquid interface structure. This is ignored in this test.

We initialize a stripe of solid into a supercooled liquid environment. The parameters (listed in table 4.1 at the end) are chosen to favour the planar growth of the solid. Figure 4.1 illustrates time snapshots of the density (a_1) and temperature (a_2) fields. A one-dimensional profile is obtained by analysis along the indicated red line. In subpanels (b_1) - (b_3), the associated density, velocity, and thermal profiles are presented for two time snapshots of the growth, shifted vertically for clarity. In subpanel (b_1) a clear distinction between the solid and liquid is shown with an interface established through a decay in the density amplitude. High density variation at the front leads to peaks in $\partial\psi/\partial t$, the source of the latent heat term in Eq. 4.17. Through this latent heat coupling, the high density activity releases a subsequent heat into the growing solid phase, increasing its temperature, as shown in the color panel a_2. In subpanel b_3 we observe the establishment of the characteristic steady state temperature profile across the solid-liquid interface. It is noted that because of the solid and liquid coexistence density difference captured by the TFC model, the solid depletes the liquid density surrounding the interface, resulting in a depletion layer in the temperature profile, to be expected as a result of our initialization, with uniform average density distribution. Such a feature is absent from the sharp interface model which neglects density difference. This behaviour likely the cause for the reduced solid temperature in the work by Punke *et al.* [4.22].

We track the interface position by filtering the density field through,

$$\eta = \mathscr{F}^{-1}\left[\exp\left(-\frac{k^2}{0.0009}\right)\mathscr{F}[|\psi|]\right], \tag{4.19}$$

which we have introduced in our earlier work [4.16]. The index position of the interface is tagged by evaluating, $\min\Big(\eta - (\max(\eta)+\min(\eta))/2\Big)$. This process is summarized in the data presented

in subpanel (c_1), which plots the position of the interface versus numerical time. The asymptotic linear scaling depicts the transition of solidification to the steady state growth limit over the time scale examined. An effective velocity of $v = 0.0009$, in units of numeric lattice units over time steps, is obtained by fitting a linear profile to the late stage growth. The fit has an adjusted $R^2 = 0.99972$ with form $y = mx + b$.

To obtain the thermal diffusion length, we estimate the temperature diffusion constant, $D_T = \alpha_T / \bar{\mathscr{M}}_T$, where $\bar{\mathscr{M}}_T = \langle \tau \left[2A^1 + 2\lambda^1 \psi - B_l^1 \psi^2 \right] \rangle$. These considerations give a thermal diffusion length as $l_{D_T} \approx (0.0134)^{-1}$. A direct connection to the steady-state Eq. 4.18 is garnered by using the determined l_{D_T}. In subpanel (c_2), we fit the exponential form of Eq. 4.18 to a smooth temperature interface profile,

$$T_{\text{smooth}} = \chi * \tau = \mathscr{F}^{-1}\left[\exp\left(-\frac{k^2}{0.0009} \right) \mathscr{F}[\tau] \right]$$

This additional smoothing is required for our comparison to remove the granularity produced due to the atomic structure within the interface, a key feature inherent in all PFC models. Our fit has an adjusted $R^2 = 0.99761$, with fitted diffusion length, $l_{D_T} \approx (0.01065)^{-1}$. We recover from our simulations a thermal diffusion length that is comparable to sharp interface models. We note a departure from the exponential decay behaviour at the interface endpoints. On the solid side, this is due to the release of latent heat, which results in an excess heat that need diffuse. In the limit of infinite solid diffusion, as is assumed for the sharp-interface result, this peak will soften, instantaneously increasing the bulk solid temperature. Meanwhile, on the liquid-side, the phenomenon of density depletion mentioned above results in an opposing character. In the sharp-interface theory, the solid and liquid are assumed at the idealized coexistence densities, which differs from the true situation, which is captured in the TFC model. Lastly, although we utilized a Gaussian smoothing factor on order of the interface size, the scale represents another possible degree of freedom in the fit that we did not consider. Nonetheless, restricting the fit to within the interface region shows a qualitative agreement between the profile predicted by our TFC model and the analytic sharp interface steady state temperature profile.

4.5 Temperature-Pressure Response

In traditional solidification processes, the solid-liquid interface can be approximated to be in local thermal and chemical equilibrium, hence heat transport can often be neglected. During rapid solidification processes, however, the interface is out of equilibrium [4.49] and transient thermal kinetics must be incorporated in order to properly capture the resulting micro-structures [4.4]. Of particular importance are also stresses that arise due to the presence of non-homogeneous temperature profiles during the solidification. Such thermally-induced stresses are often associated with thermal expansion, and are indicative of a material's temperature history. Beyond certain threshold such stresses can cause local precipitation and fracture to occur. It is imperative for an atomistic temperature model to be able to capture the thermal expansion behaviour during rapid cooling. This section demonstrates the use of the TFC formalism in capturing thermal-induced stress often encountered in rapid solidification.

Previous attempts at including the thermal expansion behaviour in phase field crystals models has required the explicit temperature control of equilibrium lattice length [4.22]. However, phase field crystal models are built in a fixed volume environment. Thus fluctuations of the equilibrium lattice length would thus result in differing lattice site number. To address this observation we treat the volume of phase field crystal models as constant, with fixed global atomic density. From a thermodynamic perspective the thermal expansion behaviour can be tied to the temperature dependence of the pressure,

$$\frac{\partial P}{\partial T}\Big|_{V,\rho} = \beta \kappa_T . \tag{4.20}$$

Here β is the volumetric thermal expansion factor, while κ_T denotes the isothermal bulk modulus. Both β and κ_T are further described in Appendix 4.9.1 and derived form the free energy of Eq. 4.1. The relation in Eq. 4.20 illustrates that previous phase field crystal model variants have, in fact, already contained implicit thermal expansion properties. This is the case, for example, when thermal gradients cause a density flow such as to reach mechanical equilibrium.

The aforementioned effect of thermal expansion in fixed-volume ensemble is demonstrated in Figure 4.2. The figure illustrates steady-state profiles obtained from simulation of Eqs. 4.2 and

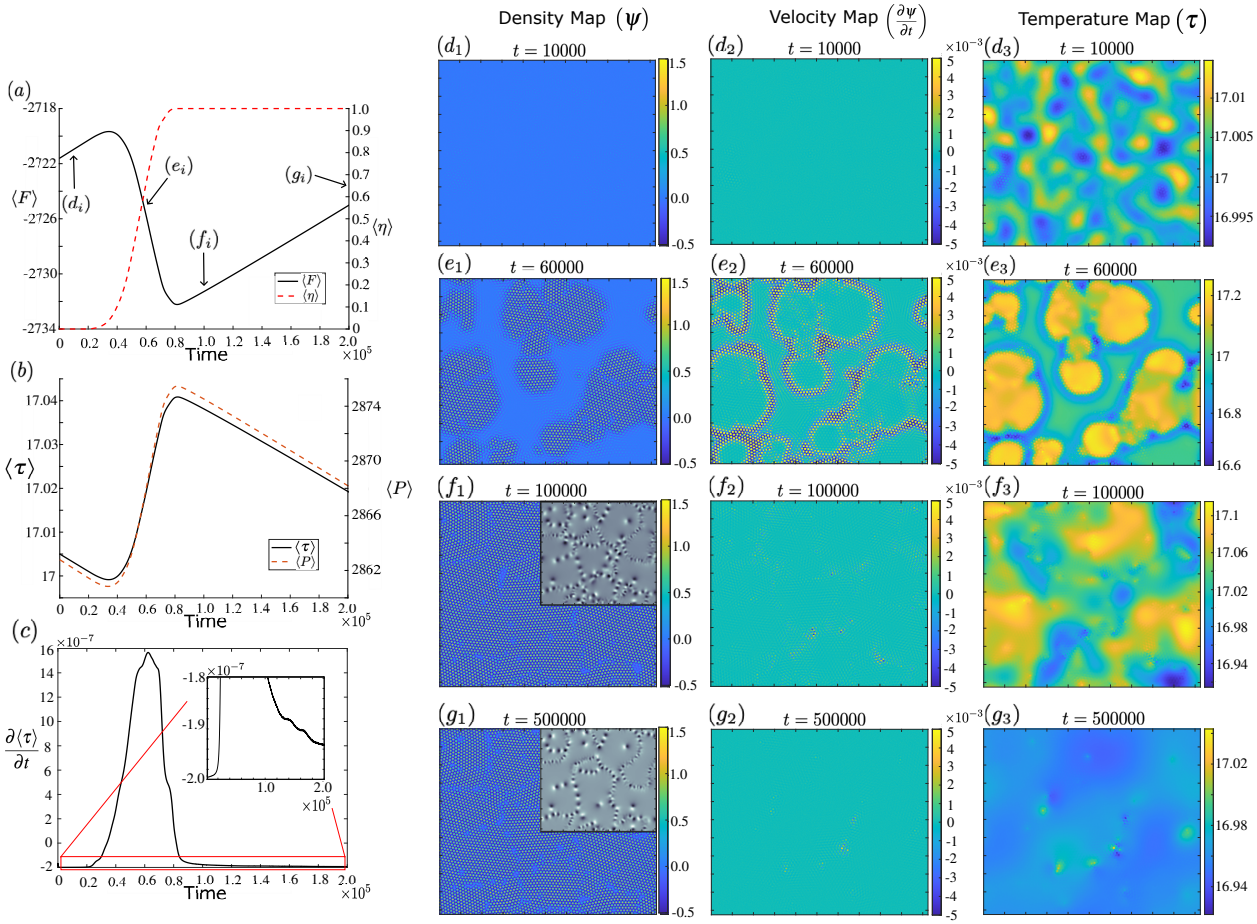

Figure 4.3: A uniform liquid phase is linearly cooled below the recalescence point. Subpanel (a) illustrates the minimization of the average system free energy, $\langle F \rangle$, in conjunction with an increase in the average solid fraction, $\langle \eta \rangle$. In subpanel (b) the time dependence of average temperature, $\langle T \rangle$, and average pressure , $\langle P \rangle$ are shown. The average free energy and pressure are computed with $k_B T_{\text{ref}} \rho_{\text{ref}} = 1$ in accordance with table 4.1. We present the time response of the average temperature rate in subpanel (c) with an inset highlighting its asymmetry, which is associated with plastic relaxation. Subpanels (d_1) - (g_3) show maps of the density, velocity, and temperature during the evolution process at the corresponding simulation times indicated in subpanel (a). An enhanced zoom in of the density maps reveals the atomistic profile. Subpanels f_1 and g_1 show a map of the hydrostatic strain associated with an impinged grain boundary. We list the simulation parameters used in Tables 4.1 and 4.2.

4.17. Subpanel (a) highlights regions of the PFC density in a domain in which the temperature is maintained fixed at $T_0 = 18$ at the two ends of the system and $T_1 = 16$ in the middle. This choice

was made to qualitatively emulate the effect a chill wall or heating surface. The corresponding one-dimensional temperature and pressure profiles along the red line in subpanel (a) are shown in subpanels b_1 and b_2 respectively.

Acting as a mediator of stress relief, the phase field crystal density field varies in amplitude. This is illustrated in figure 4.2 subpanel b_3 and b_4, where the latter image is obtained by a maximal envelope of the density field of b_3. This phenomenon is to be expected from considerations of steady-state solid hydrodynamics, as was discussed earlier. The behaviour is in analogy to electromigration where a vacancy gradient is established in response to gradients of an electric potential [4.50]. Fluctuations in the density field can be connected to variations in the vacancy concentration following Eq. 4.4. Moreover, we expect the existence of vacancy pressure to be produced in the presence of a given vacancy concentration. In the context of a time averaged density field, thermal excitations broaden the atomic profile, while maintaining a uniform average density.

We have illustrated that the phase field crystal amplitude is qualitatively tied to the vacancy concentration. Thus, in the shift to traditional constant-volume (isochoric) phase field crystal models, thermal expansion is mediated by a corresponding change of amplitude, which in turn indicates a vacancy pressure. Our findings suggest that assessing thermal stress damage in phase field crystal models must entail a quantification of the local amplitude gradients. We expect that the pressure equilibration encountered when moving into a constant pressure ensemble will result in a thermally-expanded lattice length. We note that phase field crystal models can be readily extended to the constant pressure ensemble through introduction of an auxiliary Lagrange multiplier Eq. [4.29].

4.6 Recalescence

Blacksmithing from past millennia has relied on the skill of artisans to assess the conditions of their material relative to the dynamic point of a structural transition within it. Depending on the cooling-rate, local heat release from a phase transformation will result in dancing shadows on the surface of a piece of red-hot iron. This phenomenon is known as *recalescence*, with a corresponding reverse

process, *decalescence*. Although known for years, high resolution temperature profiles indicate that the material is undergoing more than just the change of phase during these processes. More recent experiments have found that the temperature and its rate of change during recalescence can shed light on the critical nucleus size that triggered the phase transition [4.51]. This section applies the TFC modelling formalism to study the cooling rate following a first order phase transformation, showing how the processes of recalescence can be used to assess the defect density in the solidifying material. Specifically, it is shown that following the temperature-time-transformation (TTT) curves of this processes subsumes information on both structural phase transformations and dislocation activity.

4.6.1 Transformation Induced Heat Generation

We used the TFC framework to uniformly cool a liquid phase. The results are shown in Figure 4.3. At the recalescence temperature, thermal fluctuations drive the system over the transition barrier resulting in nucleation of a crystal. The material subsequently crystallizes, with a drop in system free energy. We illustrate the free energy, $\langle F \rangle$, drop behaviour in subpanel (a) of Figure 4.3. The corresponding solid fraction, η, is provided, measured by thresholding using Eq. 4.19. Subsequently, the number of grid points satisfying $\Big(\eta(x,t) - (0.1 + \psi_0)\Big) > 0$ is tabulated, thereby providing a rough picture of the transition.

Figure 4.3 also shows density, velocity, and temperature maps at different stages of the solidification in subpanels d_i, e_i, f_i, and g_i. Below the recalescence temperature, the liquid phase (d_i), solidifies, with differently orientation nuclei (e_i). The latent heat release increases the solid phase temperature, which is captured in subpanel (e_3). As the misoriented seeds impinge (f_1), the latent heat production is reduced at the grain boundaries, which is highlighted in the temperature map of subpanel (f_3). Further density evolution results in annealing, the plastic relaxation of grain boundaries and dislocations (g_i subpanels).

We illustrate the general recalescence phenomena in subpanel (b). In particular, latent heat release leads to an average temperature ($\langle T \rangle$) rise that separates bulk uniform cooling from the phase transformation. In conjunction with our earlier discussion on thermal expansion, the average

system pressure is also found to correspondingly rise. In certain situations we note that the pressure fluctuations associated with a phase transition can be sufficient to shift local thermodynamics. As a result, additional phases may form that are metastable in the context of the global thermodynamics. We also observe an asymmetry in the time rate temperature change between the nucleating liquid phase compared to late stage of solidification when crystals impinge. This is magnified as an insert of subpanel (c). As the polycrystalline system relaxes, the slow cooling rate accounts for the latent heat carried dislocations and phonons. To our knowledge, the TFC formalism is the atomic-continuum methodology that can capture latent heat release associated to plastic relaxation and phonon processes. This is discussed further below.

4.6.2 Plasticity Induced Heat Generation

In the absence of external temperature heating/cooling (source term $S(\mathbf{x},t) = 0$ in Eq. 4.17), we investigate the latent heat production associated with solid-state annealing. Here, we use TFC model parameters that favour the formation of a solid. By initialization of a polycrystalline sample through the procedure outlined in earlier work [4.2], we allow the grain boundary structure to relax. We summarize the results of system evolution in figure 4.4. Insets are provided in the figure to highlight the hydrostatic strain map of two polycrystalline snapshots. In subpanel (a) we observe an average free energy decrease, the late stages of which are associated to dislocation annihilation and grain rotation. As expected, energy is released in such stress relaxation events. Analogous to recalescence, the average temperature and pressure rise (b). We believe that the asymmetric curvature observed in subpanel (c) of figure 4.3 is associated with such deformation heating. We note that the heat generation associated with this process is an order of magnitude smaller than the heat release associated with order-disorder of solidification. The difference is in part due to the location on the phase diagram. However, this can alternatively also be caused by the low dislocation energies in two dimensions. In three dimensional systems, we expect an increase in heat generation due to plastic processes, in accordance with the increase in dislocation and grain boundary energy.

Dislocation activity is associated with temperature fluctuations in conventional temperature-

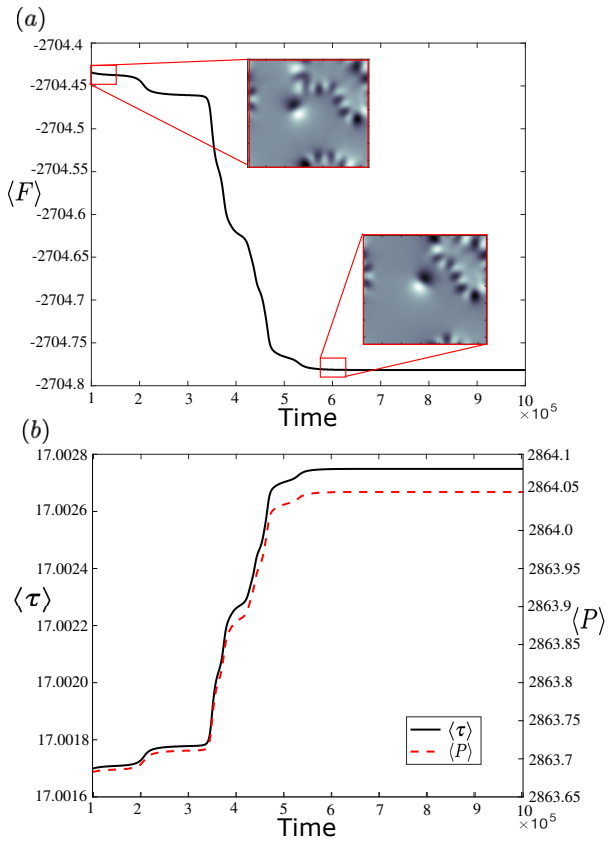

Figure 4.4: A polycrystal is simulated with TFC and allowed to relax, a processes featuring dislocation flow and grain elimination. Subpanel (*a*) shows the time dependence of the average free energy. Decreasing steps are indicative of the dislocation and grain boundary mobility. Two different snapshots of the hydrostatic strain map are provided to emphasize the grain structure. Subpanel (*b*) highlights the change of corresponding average temperature, $\langle \tau \rangle = \langle T/T_{\text{ref}} \rangle$, and average pressure, $\langle P \rangle$, associated to the relaxation process in (*a*). We list the simulation parameters used in Tables 4.1 and 4.2.

time-transformation diagrams. The aforementioned observations indicate that TFC formalism can serve as an effective temperature-time-transformation modelling approach, at least for processes associated with solidification, since like any PFC approach, it represents an expansion near liquid coexistence. Rapid solidification experiments have found the existence of dislocations, metastable phases and microstructures [4.6, 4.52–4.55]. In such scenarios, the interfacial behaviour departs from the steady state scenario of section 4.3. We thus expect that TFC may allow characterization of non-uniform latent heat generation that can be indicative of secondary phase formation

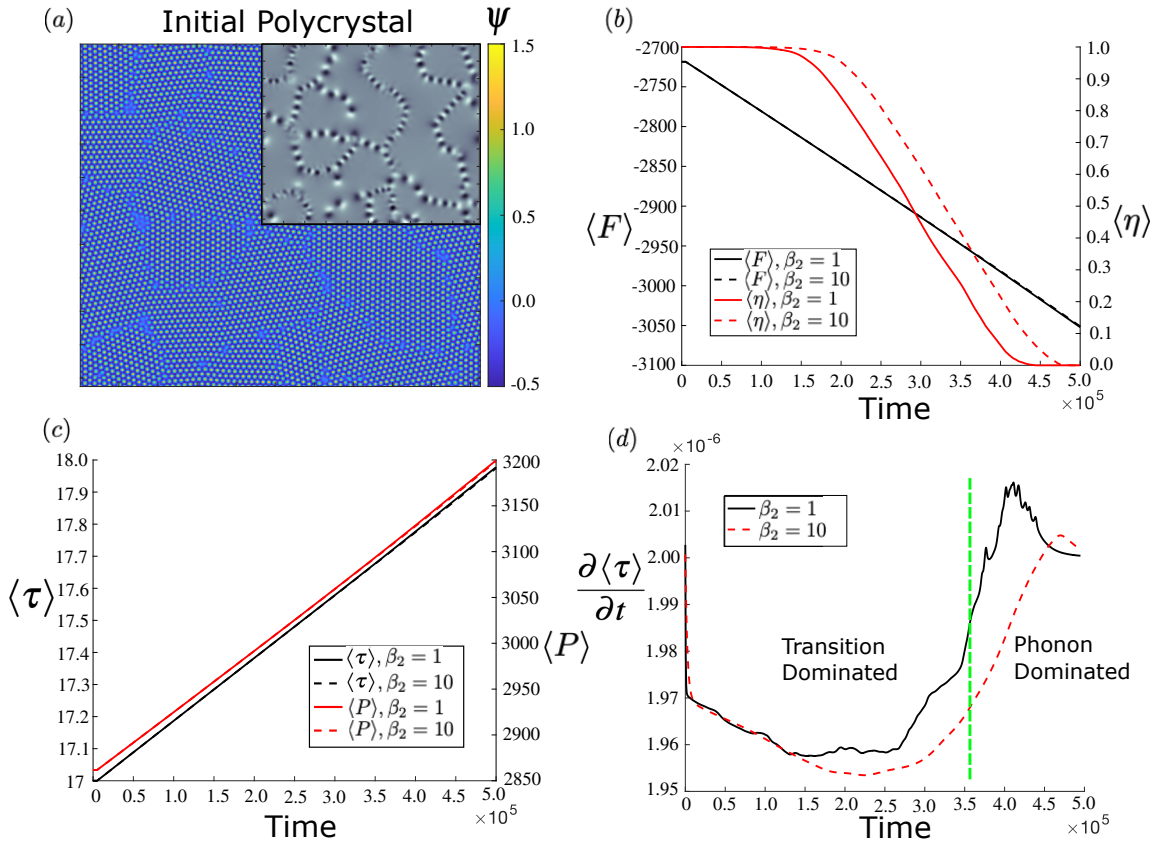

Figure 4.5: The heating of a polycrystal with two values of the dissipation constant β_2 is simulated with TFC. Subpanel (*a*) illustrates the initial polycrystalline density map with corresponding hydrostatic strain. In subpanel (*b*) we highlight the average system free energy, $\langle F \rangle$, and average solid fraction, $\langle \eta \rangle$ for both values of β examined. We illustrate the corresponding temperature and pressure ramps in subpanel *c*. We depict the rate of temperature increase in subpanel (*d*). Two dominant mechanistic regimes are highlighted, delineated in time by the vertical green line. We list the simulation parameters used in Tables 4.1 and 4.2.

and/or dislocation formation and activity. The TFC formalism can further serve as a candidate for modelling the dislocation structure obtained during solidification banding, which results from temperature diffusion scales becoming similar to that of mass diffusion [4.4]. In the solid-state, information about dislocation density nucleation (From applied stress or laser induced excitation) may be characterized from the average temperature response. Alternatively, dislocation dynamics can be assessed central to experimental measurements of the internal friction spectrum [4.56] can be investigated. Phase field crystal models have previously been shown capable at investigating

grain boundary slip [4.57]. In conjunction with temperature response, the internal friction spectrum of polycrystals may be concomitantly investigated within the framework of the TFC proposed formalism.

4.6.3 Phonon Induced Heat Generation

Another source of potential heat generation arises from phonon scattering. As high energy density perturbations propagate through a polycrystalline sample, thermal and defect scattering can split into higher frequency contributions. Such oscillations should be subsumed in the transient thermal variations accompanying the density field. The magnitude of phonon related temperature fluctuations can be significantly smaller than either crystallographic transformations described above. However, during processes such as shock loading, large phonon populations scatter and can increase the system temperature. Solid-state shock/strain heating has been documented experimentally [4.58]. We expect that during rapid phase transitions similar phenomena will be represented in through the heat transport designed into the formalism.

We illustrate an example of phonon induced heating in figure 4.5. Two dissipation constants are examined. Subpanel (*a*) shows an initial polycrystalline sample that is prepared as in the previous section. An inset is provided to enhance the grain structure for clarity. The crystal is rapidly heated to above the decalescence temperature, at which point melting occurs. We emphasize this feature in subpanel (*b*) where a decrease in solid fraction $\langle \eta \rangle$, indicative of the phase transition, is accompanied by a reduction in system free energy. The corresponding average temperature and pressure are illustrated in subpanel (*c*) of the same figure. Due to the large heating rate, the *thunderbolt* recalescence shape is not immediately observable. To elucidate this, we plot the average temperature rate in subpanel (*d*). As is expected of a reverse recalescence response, the temperature rate first decreases in time, reflecting the absorption of energy required for the transition from solid to liquid phase. Once grain boundaries have fully wetted and islets of solid remain, phonon activity becomes prevalent. As a result, the temperature rate can exceed the uniform heating rate applied to the system. Identical initial polycrystal and heating conditions are simulated with two values of β_2. We remind the reader that as β_2 is increased, the phonon decay length-scale is reduced. As a result,

the simulation with lower value of β_2 contains a higher phonon density [4.2]. Our results suggest that a larger phonon density can generated more heat, and thus increase the average temperature of the system. We note that in addition to phonon activity, a different β_2 can also shift the time scale of the simulation.

4.7 Summary

In this article we have presented a new phase field crystal variant (coined "TFC" for convenience) that self-consistently couples the two-time scale (MPFC) phase field crystal density dynamics to heat transport. In the derivation, we highlighted the additional enthalpic contributions to latent heat that were neglected in previous studies that examined such a thermo-density coupling. We demonstrated consistency of the model's heat transport properties by examining various phenomena. We found a qualitative agreement in the temperature profile across a steady-state solidification front and the analytically predicted forms found in the literature 4.18. We further demonstrated that the formalism captures the physics of thermal expansion in an isochoric system. At slow cooling rates, we observed the commonly found form of temperature versus time seen in recalescence during solidification, as well as the less commonly observed form of the pressure versus time accompanying recalascence. We further highlighted heat generation arising from plastic deformation mechanisms, as well as from phononic response. These latter features in particular are absent from conventional continuum and diffusive phase field modelling techniques. With atomistic resolution, *quasi-phonon*, and temperature diffusion modes present to the TFC formalism, it opens a new paradigm for investigation of the role of thermal stresses and thermally-coupled plasticity processes in microstructure formation occurring in rapid solidification regimes.

In constant volume ensemble, the conventional phase field crystal free energy predicts thermally mediated pressure variations. In the TFC formalism, a change of local temperature carries with it associated pressure gradients, which in turn affects local vacancy concentration, the latter of which is connected to the amplitude and average density encoded in the PFC equation. Large changes in local temperature and/or pressure changes (*e.g.* shock loading or laser heating) are also

Figure #	$\rho_{\text{ref}} k_b$	T_{ref}	D	A^0	A^1	λ^0	λ^1	B_x	B_l^0	B_l^1	α_T	D_T	D_v	$S(x,t)$	β_0	β_2	σ	$\langle\psi\rangle$
Figure 1	1	1	1	10	10	10	0.1	0.7	1	0.1	1000	0	1	0	1	1	0.001	0.09
Figure 2	1	1	1	10	10	10	0.1	0.7	1	0.1	1000	0	1	0	1	1	0.001	0.15
Figure 3	1	1	1	10	10	10	0.1	0.7	1	0.1	1000	0	1	-2×10^{-7}	1	1	0.001	0
Figure 4	1	1	1	10	10	10	0.1	0.7	1	0.1	1000	0	1	0	1	1	0	0.1
Figure 5	1	1	1	10	10	10	0.1	0.7	1	0.1	1000	0	1	2×10^{-6}	1	1, 10	0	0

Table 4.1: List of parameters used in the TFC model during this investigation. Each row reflects the parameter set used for generation of the corresponding figure.

expected to trigger metastable phase nucleation, particularly in multi-component alloys. We expect that such meta-stable processes may be examined by the proposed TFC formalism as they will have a signature in their temperature response since metastable structures will have an associated latent heat release.

We demonstrated that the recalescence curves contain a substantial amount information about the inner working of metals. Within the context of TFC, the recalescence curve encompasses information about ordering changes in a transformation, plastic deformation processes, as well as phonon-generated heat generation mechanisms. We suspect that detailed temperature measurements during solidification and/or annealing may allow for non-invasive metrics of microstructure and phonon response.

4.8 Acknowledgements

We thank Natural Sciences and Engineering Research Council of Canada (NSERC) and *le Fonds de recherche du Quebec—Nature et technologies* for funding support. Additionally, we thank Calcul Québec and the Digital Research Alliance of Canada for computing resources.

Figure #	L_X	L_Y	dx	dy	dt
Figure 1	512	512	0.8502	0.9817	0.02
Figure 2	512	2048	0.8502	0.9817	0.01
Figure 3	512	512	0.8502	0.9817	0.01
Figure 4	128	128	0.8502	0.9817	0.02
Figure 5	512	512	0.8502	0.9817	0.02

Table 4.2: List of numerical parameters used during this investigation. Each row reflects the parameter set used for generation of the corresponding figure.

4.9 Appendix

4.9.1 Thermodynamics

Mode-Expansion Formalism

Phase field crystal models are built through an expansion of the free energy about a point on the liquidus. In Elder *et al.* [4.12], the correlation function is built by its connection to the liquid-state structure factor of Argon, which is tacitly assumed to have a generic form applicable to the crystallization of other materials. The effective temperature built into the free energy is such as to control the formation of ordered phases from disordered phases without structure. To understand the phase energetics that emerge from a PFC model, it customary to approximate the solid phase through an associated mode-expansion ansatz given by

$$\rho(r) = \overline{\rho} + \Sigma_{G_j} A_{|G_j|} e^{iG_j \cdot r}, \tag{4.21}$$

where the sum is over reciprocal lattice vectors, G_j. The parameter $\overline{\rho} = \rho_{\text{ref}}(1+\psi_0)$ represents the uniform average density adopted by the system. The liquid phase corresponds to a state where $A_{G_j} = 0$ minimizes the free energy. Meanwhile, the ordered phase is the equilibrium configuration where the minimizing amplitude is non-zero. We note the existence of additional lower-dimensional phases such as the stripe phase. The energetics of different phases can be analyzed through substitution of Eq. 4.21 into the free energy in Eq. 4.1 and integrating over a unit cell of the solid phase being considered. This approximates the system's free energy in terms of $(\bar{\rho}, A_{G_j})$. As

an example, we investigate here the coexistence of a the classic 2D solid with a triangular lattice with a liquid. Keeping only the first crystallographic mode of the triangular lattice in equation 4.21 results in the following free energy,

$$\begin{aligned}\frac{\overline{F}}{k_b T \overline{a}^2 \rho_{\text{ref}}} &= A(T) + \lambda(T)\psi_0 \\ &+ (B_l(T))\frac{\psi_0^2}{2} - \frac{\psi_0^3}{6} + \frac{\psi_0^4}{12} \\ &+ 120A_{|G|}^4 + (32\psi_0 - 16)A_{|G|}^3 \\ &+ 12(1 - \psi_0 + \psi_0^2 - (1 + B_x + B_l(T)))A_{|G|}^2,\end{aligned} \tag{4.22}$$

where $\overline{F}$ denotes the free energy per atom. In reference to our fixed volume numerical grid, we keep the total number of lattice sites with lattice length $\overline{a}$ conserved. When considering more exotic configurations that lack an analytic representation, the free energy and thermodynamic potentials may be extracted numerically.

Phase Diagrams

To investigate what parameter range will favor a specific bulk phase, we build the associated phase diagram. Here we solve the condition of phase coexistence:

$$\mu_1 = \mu_2 \tag{4.23a}$$

$$f_1 - \overline{\rho_1}\mu_1 = f_2 - \overline{\rho_2}\mu_2, \tag{4.23b}$$

where $\mu_i = \delta F/\delta\rho$ is the chemical potential and $\overline{\rho_i}$ coexistence density associated to phase i. The chemical potential may be extracted as in the previous section,

$$\begin{aligned}\frac{\overline{\mu}}{k_b T \rho_{\text{ref}}} &= \lambda(T) + \psi_0 B_l(T) - \frac{\psi_0^2}{2} + \frac{\psi_0^3}{3} \\ &+ (-12 + 24\psi_0)A_{|G|}^2 + 32A_{|G|}^3,\end{aligned} \tag{4.24}$$

We next find the A_G that minimize the free energy in Eq. 4.22, and substitute these into the equations 4.23a and 4.23b, which can then be solved for the coexistence densities of each bulk phase, $\bar{\rho}_1$ and $\bar{\rho}_2$, at a corresponding temperature. Although explicit calculation of the coexistence relations is possible, one can also make use of a convex hull algorithm of the free energy as detailed by Seymour *et al.* [4.59], and readily available in many applications like Mathematica. Repeating the calculation at different temperatures and average densities results in a phase diagram such as the one illustrated in figure 4.6 for the classic PFC model of Ref. [4.12]. The highlighted regions spans the set of temperatures and average system densities used throughout this article.

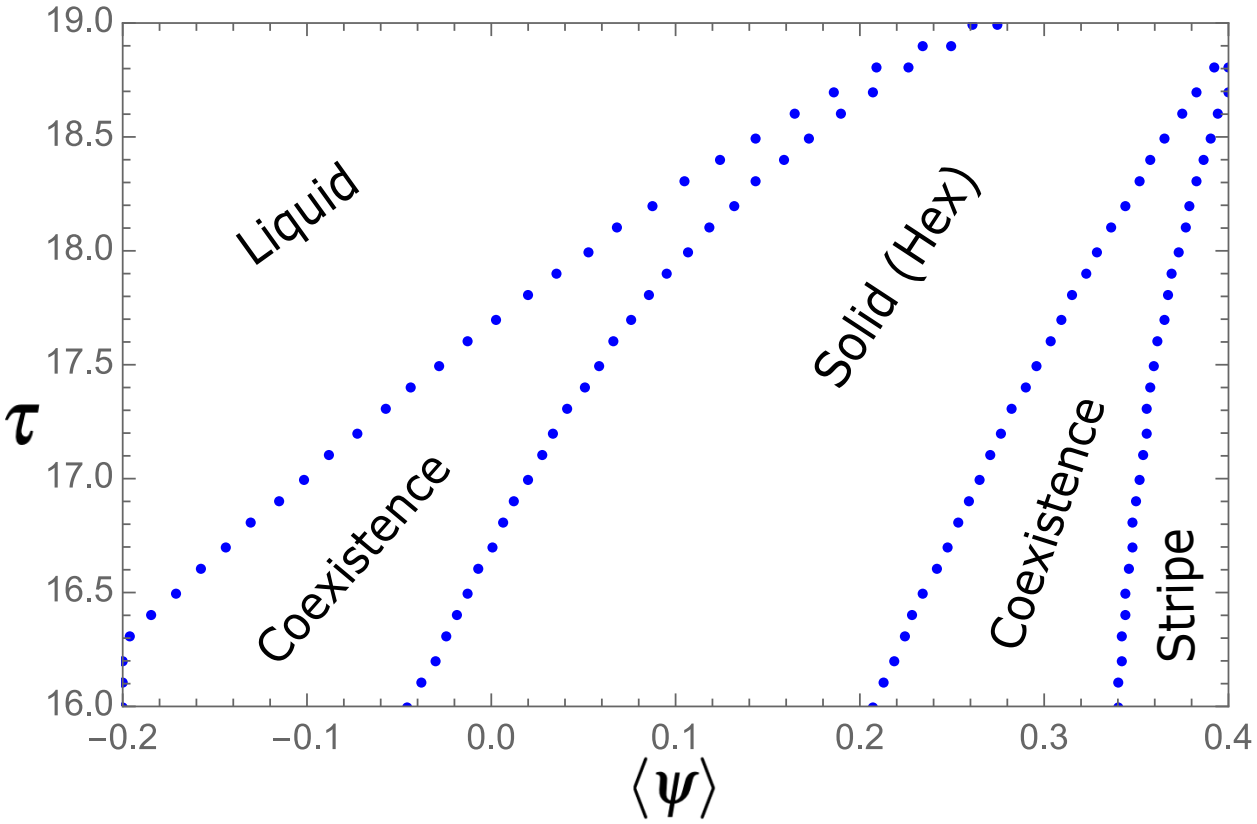

Figure 4.6: Illustrated is phase diagram with parameters as listed in Table 4.1. Simulations were performed in two-dimensions, hence necessitating the free energy minimization with all lower dimensional structures, such as the stripe phase.

Thermomechanical Components of Model

Past work on fitting the phase field crystal model parameters to experimental measures, has been largely restricted to the thermodynamics of the phase diagram [4.60, 4.61]. Such consideration is sufficient when working under an isothermal approximation, though limiting the permissible temperature range of phase diagrams. The closest attempt at addressing temperature thermodynamics has been done by Mellenthin *et al.* when fitting the phase field crystal amplitude heights to molecular dynamics simulations [4.62]. As we have alluded to earlier in this article, such comparison is tantamount to setting the temperature scaling of the solid pressure. It is noteworthy that special care must be made to ensure molecular dynamic simulations contain the proper anharmonicity behaviours [4.63]. Here, we illustrate a connection between the free energy parameters of Eq. 4.1, through the Grüneisen equation of state. Here fluctuations of the internal energy trigger corresponding pressure changes with scale set by the Grüneisen constant, γ, given by

$$\gamma = V \frac{\partial P}{\partial E}\Big|_V = \frac{\beta_T \kappa_T}{C_V \rho_{\text{ref}}(1+\psi)}, \tag{4.25}$$

where κ_T, β_T, and C_V denote the isothermal bulk modulus, volumetric thermal expansion factor, and isochoric heat capacity respectively. We note that substantial experimental data has been tabulated such thermodynamic constant [4.47, 4.64–4.66].

Through the same procedure as solving for bulk phase energies, we can solve for the bulk pressure using equation 4.7b,

$$\begin{aligned} \frac{\overline{P}}{k_b T \rho_{\text{ref}}} &= \lambda(T) - A(T) + \psi_0 B_l(T) \\ &\quad - \frac{\psi_0^2}{2}(1 - B_l(T)) - 12(1 - B_l(T) + B_x)A_{|G|}^2 \end{aligned} \tag{4.26}$$

By taking the appropriate thermodynamic derivatives, namely,

$$\kappa_T = \rho \frac{\partial P}{\partial \rho}\Big|_{T,N} = (1+\psi)\frac{\partial P}{\partial \psi}\Big|_{T,N,V}, \tag{4.27a}$$

$$\beta_T = \frac{1}{\kappa_T}\frac{\partial P}{\partial T}\Big|_{V,N}, \tag{4.27b}$$

$$C_V = -T\frac{\partial^2 F}{\partial T^2}\Big|_{T,N,V}, \tag{4.27c}$$

the associated material constants can be determined in terms of the PFC free energy.

The free energy of Eq. 4.1 is expanded around a liquidus reference density ρ_{ref} and temperature T_{ref}. Using materials-specific values for these to scale the PFC free energy parameters, and evaluating the material constants in equations 4.25 and 4.27 at the expansion point, yields the following system of equations,

$$\kappa_{T\text{ref}} = \lim_{\psi\to 0}\kappa_T = \rho_{\text{ref}} k_b \tau T_{\text{ref}} B_l(\tau), \tag{4.28a}$$

$$\beta_{T,\text{ref}} = \lim_{\psi\to 0}\beta_T = \frac{\lambda^0 - A^0 + 2(-\lambda^1 + A^1)\tau}{\tau T_{\text{ref}} B_l(\tau)}, \tag{4.28b}$$

$$C_{V,\text{ref}} = \lim_{\psi\to 0} C_V = k_b \rho_{\text{ref}} 2A^1\tau, \tag{4.28c}$$

$$\gamma_{\text{ref}} = \lim_{\psi\to 0}\gamma = \frac{\lambda^0 - A^0 + 2(-\lambda^1 + A^1)\tau}{2A^1\tau}. \tag{4.28d}$$

By direct comparison to experimental measurements, the above system of equations allows us to compute the phase field crystal model parameters that corresponds to a specific material. In accordance with our assumption of weak temperature dependence, it may be appropriate to further expand Eqs. 4.28 around the reference temperature, T_{ref}, of the model. While the above procedure defines a consistent formalism for evaluating the PFC model parameters, it is noted that the weak temperature dependence assumed throughout this paper may not be adequate to describe the complete phase diagram.

4.9.2 Reactive Stress

In this section we illustrate the connection between ϕ and the vacancy chemical potential, $\mu_c = \delta F/\delta c|_{T,\rho}$. The coefficient ϕ was alluded to in our discussion on solid hydrodynamics and is associated to the vacancy stress. Following the notation of Cohen *et al.*,

$$\phi = \frac{\delta E}{\delta u_{ij}}\Big|_{s,\rho}, \tag{4.29}$$

at fixed entropy and lattice deformation [4.34]. Thus the lack of lattice site occupancy gives rise to a stress captured through ϕ. Performing a Legendre transformation to the constant temperature ensemble followed by use of relation 4.4 connecting strain, vacancy concentration, density fluctuations yields,

$$\phi = \frac{\delta F}{\delta u_{ij}}\Big|_{T,\rho} = \left(\frac{\delta F}{\delta c}\Big|_{T,\rho}\right)\frac{\partial c}{\partial u_{ij}}. \tag{4.30}$$

We may hence interrelate the vacancy chemical potential, $\delta F/\delta c|_{T,\rho} = \mu_c$, to the vacancy stress entering the hydrodynamics encapsulated in Eqs. 4.3a-4.3d.

In our previous work, the form of the stress tensor, $\overleftrightarrow{\sigma}$, entering Eq. 4.3b had been assumed to derive the MPFC dynamics of Eq. 4.2. In particular,

$$\sigma = \frac{\delta E}{\delta u_{ij}}\Big|_{s} = \sigma_R + \chi, \tag{4.31}$$

where $\sigma_R = \delta E/\delta u_{ij}|_{s,c}$ denotes the reversible stress and $\chi = \delta E/\delta u_{ij}|_{s,\rho}$ the conditionally reversible stress. In the notation of Cohen *et al.*, $\chi = \phi$. With vanishing vacancy concentration, a reversible deformation would restore itself by solely mass diffusion. However, non-vanishing vacancy contributions would result in additional strain and strain-rate modifications to the dynamics. We note that the interrelation between χ and ϕ, implies following Eq. 4.30 that $\chi = \mu_c \frac{\partial c}{\partial u_{ij}}$. In other words, the additional stress contribution added in our previous work, amounts to the addition of a vacancy chemical potential.

4.10 Bibliography

[4.1] J. Berry and M. Grant. "Phase-field-crystal modeling of glass-forming liquids: Spanning time scales during vitrification, aging, and deformation". In: *Physical Review E* 89 (6 2014), p. 062303. DOI: 10.1103/PhysRevE.89.062303.

[4.2] D. Burns, N. Provatas, and M. Grant. "Two-dimensional phase field crystal simulation of laser-induced recrystallization: A mechanism of grain-boundary phonon scattering and softening". In: *Physical Review Materials* 7 (8 2023), p. 083402. DOI: 10.1103/PhysRevMaterials.7.083402.

[4.3] A. Karma and A. Sarkissian. "Interface dynamics and banding in rapid solidification". In: *Physical Review E* 47 (1 1993), pp. 513–533. DOI: 10.1103/PhysRevE.47.513.

[4.4] K. Ji et al. "Microstructural Pattern Formation during Far-from-Equilibrium Alloy Solidification". In: *Physical Review Letters* 130 (2 2023), p. 026203. DOI: 10.1103/PhysRevLett.130.026203.

[4.5] M. Hillert, M. Schwind, and M. Selleby. "Trapping of vacancies by rapid solidification". In: *Acta Materialia* 50.12 (2002), pp. 3285–3293. ISSN: 1359-6454. DOI: 10.1016/S1359-6454(02)00150-7.

[4.6] T. Pinomaa et al. "Multiscale analysis of crystalline defect formation in rapid solidification of pure aluminium and aluminium–copper alloys". In: *Philosophical Transactions of the Royal Society A: Mathematical, Physical and Engineering Sciences* 380.2217 (2022), p. 20200319. DOI: 10.1098/rsta.2020.0319.

[4.7] J.A. Dantzig and M. Rappaz. *Solidification: 2nd Edition - Revised & Expanded*. Engineering Sciences. CRC Press LLC, 2016. ISBN: 9782940222971.

[4.8] B. J. Alder and T. E. Wainwright. "Studies in Molecular Dynamics. I. General Method". In: *The Journal of Chemical Physics* 31.2 (2004), pp. 459–466. ISSN: 0021-9606. DOI: 10.1063/1.1730376.

[4.9] G. Caginalp. “Stefan and Hele-Shaw type models as asymptotic limits of the phase-field equations”. In: *Physical Review A* 39 (11 1989), pp. 5887–5896. DOI: 10.1103/PhysRevA.39.5887.

[4.10] R. F. Sekerka. “Morphology: from sharp interface to phase field models”. In: *Journal of Crystal Growth* 264.4 (2004). Proceedings of the Symposium - Progress in Crystal Growth, pp. 530–540. ISSN: 0022-0248. DOI: https://doi.org/10.1016/j.jcrysgro.2003.12.033.

[4.11] K. R. Elder et al. “Sharp interface limits of phase-field models”. In: *Physical Review E* 64 (2 2001), p. 021604. DOI: 10.1103/PhysRevE.64.021604.

[4.12] K. R. Elder and M. Grant. “Modeling elastic and plastic deformations in nonequilibrium processing using phase field crystals”. In: *Physical Review E* 70 (5 2004), p. 051605. DOI: 10.1103/PhysRevE.70.051605.

[4.13] P. K. Galenko et al. “Solute trapping in rapid solidification of a binary dilute system: A phase-field study”. In: *Physical Review E* 84 (4 2011), p. 041143. DOI: 10.1103/PhysRevE.84.041143.

[4.14] P. Stefanovic, M. Haataja, and N. Provatas. “Phase-Field Crystals with Elastic Interactions”. In: *Physical Review Letters* 96 (22 2006), p. 225504. DOI: 10.1103/PhysRevLett.96.225504.

[4.15] S. Majaniemi and M. Grant. “Dissipative phenomena and acoustic phonons in isothermal crystals: A density-functional theory study”. In: *Physical Review B* 75 (5 2007), p. 054301. DOI: 10.1103/PhysRevB.75.054301.

[4.16] D. Burns, N. Provatas, and M. Grant. “Time-scale investigation with the modified phase field crystal method”. In: *Modelling Simulation Material Science and Engineering* 30 (6 2022), p. 064001. DOI: 10.1088/1361-651X/ac7c83.

[4.17] R. Chen et al. “Effect of cooling rate on solidification parameters and microstructure of Al-7Si-0.3Mg-0.15Fe alloy”. In: *Transactions of Nonferrous Metals Society of China* 24.6 (2014), pp. 1645–1652.

[4.18] J. S. Langer, E. Bouchbinder, and T. Lookman. “Thermodynamic theory of dislocation-mediated plasticity”. In: *Acta Materialia* 58.10 (2010), pp. 3718–3732.

[4.19] J. S. Langer. “Thermal effects in dislocation theory”. In: *Physical Review E* 94 (6 2016), p. 063004. DOI: 10.1103/PhysRevE.94.063004.

[4.20] G. Kocher and N. Provatas. “Thermodensity coupling in phase-field-crystal-type models for the study of rapid crystallization”. In: *Physical Review Materials* 3 (5 2019), p. 053804. DOI: 10.1103/PhysRevMaterials.3.053804.

[4.21] C. Wang and M. S. Wise. “A Thermodynamically-Consistent Phase Field Crystal Model of Solidification with Heat Flux”. In: *Journal of Mathematical Study* 55.4 (2022), pp. 337–357. ISSN: 2617-8702. DOI: https://doi.org/10.4208/jms.v55n4.22.01.

[4.22] M. Punke et al. “Explicit temperature coupling in phase-field crystal models of solidification”. In: *Modelling Simulation Material Science and Engineering* 30 (6 2022), p. 074004. DOI: 10.1088/1361-651X/ac8abd.

[4.23] P. C. Hohenberg and B. I. Halperin. “Theory of dynamic critical phenomena”. In: *Review Modern Physics* 49 (3 1977), pp. 435–479. DOI: 10.1103/RevModPhys.49.435.

[4.24] “Phase Field Crystal Modeling of Pure Materials”. In: *Phase-Field Methods in Materials Science and Engineering*. John Wiley & Sons, Ltd, 2010. Chap. 8, pp. 167–208. ISBN: 9783527631520. DOI: https://doi.org/10.1002/9F783527631520.ch8.

[4.25] J. S. Langer. “Instabilities and pattern formation in crystal growth”. In: *Review Modern Physics* 52 (1 1980), pp. 1–28. DOI: 10.1103/RevModPhys.52.1.

[4.26] G. Kocher and N. Provatas. “New Density Functional Approach for Solid-Liquid-Vapor Transitions in Pure Materials”. In: *Physical Review Letters* 114 (15 2015), p. 155501. DOI: 10.1103/PhysRevLett.114.155501.

[4.27] Z. Wang et al. “Minimal phase-field crystal modeling of vapor-liquid-solid coexistence and transitions”. In: *Physical Review Materials* 4 (10 2020), p. 103802. DOI: 10.1103/PhysRevMaterials.4.103802.

[4.28] N. Ofori-Opoku et al. “Multicomponent phase-field crystal model for structural transformations in metal alloys”. In: *Physical Review B* 87 (13 2013), p. 134105. DOI: 10.1103/PhysRevB.87.134105.

[4.29] M. J. Frick, N. Ofori-Opoku, and N. Provatas. “Incorporating density jumps and species-conserving dynamics in XPFC binary alloys”. In: *Physical Review Materials* 4 (8 2020), p. 083404. DOI: 10.1103/PhysRevMaterials.4.083404.

[4.30] T. V. Ramakrishnan and M. Yussouff. “First-principles order-parameter theory of freezing”. In: *Physical Review B* 19 (5 1979), pp. 2775–2794. DOI: 10.1103/PhysRevB.19.2775.

[4.31] K. R. Elder et al. “Phase-field crystal modeling and classical density functional theory of freezing”. In: *Physical Review B* 75 (6 2007), p. 064107. DOI: 10.1103/PhysRevB.75.064107.

[4.32] M. Greenwood, N. Provatas, and J. Rottler. “Free Energy Functionals for Efficient Phase Field Crystal Modeling of Structural Phase Transformations”. In: *Physical Review Letters* 105 (4 2010), p. 045702. DOI: 10.1103/PhysRevLett.105.045702.

[4.33] J. Berry et al. “Phase field crystal modeling as a unified atomistic approach to defect dynamics”. In: *Physical Review B* 89 (21 2014), p. 214117. DOI: 10.1103/PhysRevB.89.214117.

[4.34] C. Cohen, P. D. Fleming, and J. H. Gibbs. “Hydrodynamics of amorphous solids with application to the light-scattering spectrum”. In: *Physical Review B* 13 (2 1976), pp. 866–877. DOI: 10.1103/PhysRevB.13.866.

[4.35] P. D. Fleming and C. Cohen. “Hydrodynamics of solids”. In: *Physical Review B* 13 (2 1976), pp. 500–516. DOI: 10.1103/PhysRevB.13.500.

[4.36] B. I. Halperin and David R. Nelson. “Theory of Two-Dimensional Melting”. In: *Physical Review Letters* 41 (2 1978), pp. 121–124. DOI: 10.1103/PhysRevLett.41.121.

[4.37] M. Salvalaglio and K. R. Elder. “Coarse-grained modeling of crystals by the amplitude expansion of the phase-field crystal model: an overview”. In: *Modelling Simulation Material Science and Engineering* 30 (5 2022), p. 053001. DOI: 10.1088/1361-651X/ac681e.

[4.38] C. Walz and M. Fuchs. “Displacement field and elastic constants in nonideal crystals”. In: *Physical Review B* 81 (13 2010), p. 134110. DOI: 10.1103/PhysRevB.81.134110.

[4.39] T. Koyama and Y. Tsukada. “Ludwig–Soret effect formulated from the grain-boundary-phase model”. In: *Calphad* 73 (2021), p. 102269. ISSN: 0364-5916. DOI: https://doi.org/10.1016/j.calphad.2021.102269.

[4.40] R.A Swalin and C.A Yin. “Thermal diffusion of vacancies in aluminum”. In: *Acta Metallurgica* 15.2 (1967), pp. 245–248. ISSN: 0001-6160. DOI: https://doi.org/10.1016/0001-6160(67)90198-8.

[4.41] J.P. Stark. “Vacancy concentrations in single crystal thermal diffusion experiments”. In: *Scripta Metallurgica* 5.9 (1971), pp. 727–732. ISSN: 0036-9748. DOI: https://doi.org/10.1016/0036-9748(71)90153-0.

[4.42] P. Shewmon. “Thermal Diffusion of Vacancies in Zinc”. In: *The Journal of Chemical Physics* 29.5 (2004), pp. 1032–1036. ISSN: 0021-9606. DOI: 10.1063/1.1744650.

[4.43] A. Hellouin de Menibus et al. “Formation and characterization of hydride blisters in Zircaloy-4 cladding tubes”. In: *Journal of Nuclear Materials* 449.1 (2014), pp. 132–147. ISSN: 0022-3115. DOI: https://doi.org/10.1016/j.jnucmat.2014.03.006.

[4.44] L. P. Kadanoff and P. C. Martin. “Hydrodynamic equations and correlation functions”. In: *Annals of Physics* 24 (1963), pp. 419–469. ISSN: 0003-4916. DOI: https://doi.org/10.1016/0003-4916(63)90078-2.

[4.45] N. Provatas, T. Pinomaa, and N. Ofori-Opoku. CRC Press, 2021. DOI: https://doi.org/10.1201/9781003204312.

[4.46] W. W. Mullins and R. F. Sekerka. “Stability of a Planar Interface During Solidification of a Dilute Binary Alloy”. In: *Journal of Applied Physics* 35.2 (1964), pp. 444–451. DOI: 10.1063/1.1713333.

[4.47] R.N. Singh, S. Arafin, and A.K. George. “Temperature-dependent thermo-elastic properties of s-, p- and d-block liquid metals”. In: *Physica B: Condensed Matter* 387.1 (2007), pp. 344–351. ISSN: 0921-4526. DOI: 10.1016/j.physb.2006.04.029.

[4.48] H. Emmerich et al. “Phase-field-crystal models for condensed matter dynamics on atomic length and diffusive time scales: an overview”. In: *Advances in Physics* 61.6 (2012), pp. 665–743. DOI: 10.1080/00018732.2012.737555.

[4.49] T. Pinomaa, A. Laukkanen, and N. Provatas. “Solute trapping in rapid solidification”. In: *MRS Bulletin* 45.11 (2020), 910–915. DOI: 10.1557/mrs.2020.274.

[4.50] N. Wang, K. H. Bevan, and N. Provatas. “Phase-Field-Crystal Model for Electromigration in Metal Interconnects”. In: *Physical Review Letters* 117 (15 2016), p. 155901. DOI: 10.1103/PhysRevLett.117.155901.

[4.51] J. Xu et al. “The recalescence rate of cooling curve for undercooled solidification”. In: *Scientific Reports* 10.1 (2020), p. 1380. ISSN: 2045-2322. DOI: 10.1038/s41598-019-56079-6.

[4.52] M. Golizadeh et al. “Rapid solidification and metastable phase formation during surface modifications of composite Al-Cr cathodes exposed to cathodic arc plasma”. In: *Journal of Materials Science & Technology* 94 (2021), pp. 147–163. ISSN: 1005-0302. DOI: https://doi.org/10.1016/j.jmst.2021.03.059.

[4.53] K.G. Prashanth and J. Eckert. “Formation of metastable cellular microstructures in selective laser melted alloys”. In: *Journal of Alloys and Compounds* 707 (2017). Selected papers presented at ISMANAM 2016, July 3rd-8th, Nara, Japan, pp. 27–34. ISSN: 0925-8388. DOI: https://doi.org/10.1016/j.jallcom.2016.12.209.

[4.54] J. H. Perepezko and W. J. Boettinger. “Use of Metastable Phase Diagrams in Rapid Solidification”. In: *MRS Online Proceedings Library (OPL)* 19 (1982), p. 223. DOI: 10.1557/PROC-19-223.

[4.55] H. Jones. “Splat cooling and metastable phases”. In: *Reports on Progress in Physics* 36.11 (1973), p. 1425. DOI: 10.1088/0034-4885/36/11/002.

[4.56] M.J. Konstantinović. “Internal friction study of dislocation dynamics in neutron irradiated iron, and iron–copper alloys”. In: *Journal of Nuclear Materials* 395.1 (2009), pp. 75–78. ISSN: 0022-3115. DOI: https://doi.org/10.1016/j.jnucmat.2009.09.020.

[4.57] P. Stefanovic, M. Haataja, and N. Provatas. “Phase field crystal study of deformation and plasticity in nanocrystalline materials”. In: *Physical Review E* 80 (4 2009), p. 046107. DOI: 10.1103/PhysRevE.80.046107.

[4.58] H. Tan and T. J. Ahrens. “Shock temperature measurements for metals”. In: *High Pressure Research* 2.3 (1990), pp. 159–182. DOI: 10.1080/08957959008201036.

[4.59] M. Seymour. *Study of multi-point interactions in PFC models for complex structural transformations*. McGill University (Canada), 2018.

[4.60] A. Jaatinen et al. “Thermodynamics of bcc metals in phase-field-crystal models”. In: *Physical Review E* 80 (3 2009), p. 031602. DOI: 10.1103/PhysRevE.80.031602.

[4.61] V.W.L. Chan, N. Pisutha-Arnond, and K. Thornton. “Thermodynamic relationships for homogeneous crystalline and liquid phases in the phase-field crystal model”. In: *Computational Materials Science* 135 (2017), pp. 205–213. ISSN: 0927-0256. DOI: https://doi.org/10.1016/j.commatsci.2017.04.017.

[4.62] Jesper Mellenthin, Alain Karma, and Mathis Plapp. “Phase-field crystal study of grain-boundary premelting”. In: *Physical Review B* 78 (18 2008), p. 184110. DOI: 10.1103/PhysRevB.78.184110.

[4.63] L. J. Porter, J. F. Justo, and S. Yip. “The importance of Grüneisen parameters in developing interatomic potentials”. In: *Journal of Applied Physics* 82.11 (1997), pp. 5378–5381. ISSN: 0021-8979. DOI: 10.1063/1.366305.

[4.64] J.L. Tallon and A. Wolfenden. “Temperature dependence of the elastic constants of aluminum”. In: *Journal of Physics and Chemistry of Solids* 40.11 (1979), pp. 831–837. ISSN: 0022-3697. DOI: https://doi.org/10.1016/0022-3697(79)90037-4.

[4.65] A.T. Dinsdale. “SGTE data for pure elements”. In: *Calphad* 15.4 (1991), pp. 317–425. ISSN: 0364-5916. DOI: 10.1016/0364-5916(91)90030-N.

[4.66] G. Deffrennes and B. Oudot. “A self-consistent model to describe the temperature dependence of the bulk modulus, thermal expansion and molar volume compatible with 3rd generation CALPHAD databases”. In: *Calphad* 74 (2021), p. 102291. ISSN: 0364-5916. DOI: https://doi.org/10.1016/j.calphad.2021.102291.

Chapter 5

Discussion

The investigation of chapters 2-4 documents our progression towards the overarching hypothesis of species limited energy relaxation. Particularly, phase field crystal techniques were utilized to understand the microstructural response that arises from the incorporation of additional energy carrying modes. With inspiration drawn from past binary alloy studies [91–93] and experimental measurements [79], the conservation laws of hydrodynamics are used as a template for a new class of phase field crystal approaches. Therein, mass, strain, momentum, and temperature fields propagate according to local gradients of driving forces.

In **Chapter 2** we built a foundation for the isothermal PFC study of phonon-density dynamics in terms of a single density field equation denoted (MPFC). Novel strain and dislocation mappings are used to interrelate the density, hydrostatic strain, and vacancy concentration. Herein phonon dispersion associated to thermal scattering is added, which forms a connection to more complex crystal propagation equations. In the limit of high dissipation, the model was shown capable of recovering Mullins-Sekerka interface instabilities. As the dissipation was reduced, we showed that phonon induced deviations of steady-state growth emerge. In passing, a minimal free energy term was discussed to separate strain diffusion from chemical diffusion. It was argued that such an addition may permit the separation of climb and glide time scales. The study was further supplemented by a numeric algorithm for rapid simulation.

Our first application of this latest MPFC innovation developed in chapter 2 consists of a density

dependent function, capable of extracting the hydrostatic strain map of polycrystalline materials. The detailed measurement of lattice deformation relative to an idealized packing constitutes an important metric in microstructure analysis. For example, the strain can be used to characterize dislocations and grain boundaries by their energies [94]. In the phase field crystal study of grain boundary sliding, Stefanovic *et al.* employed a thresholding and peak finding algorithm to determine the interatomic positions and thereby deduce the strain. Peak finders, which have seen use in other phase field crystal literature are however computationally taxing. In addition, the time resolved structure of the phase field crystal atomic profile has ill-defined atomic positions near grain boundaries. To alleviate these challenges, the Fourier space density structure is utilized [95–98]. Unfortunately, the requirement of well separated Bragg peaks limits the application of study to nearly idealized lattices. We noted that substantial information of the dislocation properties can be obtained through only the trace of the strain tensor. Subsequently, we drew on inspiration from powder X-ray diffraction methods, such as Warren-Averbach and Scherrer decomposition. It was noted that the asymmetry of the Bragg ring, the circle of corresponding wavevector magnitude on which the Bragg peaks sit, is indicative of the local compression and rarefaction. A phenomenological relation between hydrostatic strain and density field was subsequently developed. In passing, we also introduced a dislocation map built from the intensity of the Bragg ring. Our relations serve as tools to characterize the dislocations and grain boundaries constituting polycrystalline materials. Since the relations are phenomenological in origin, the proper scaling and proportionality remain unknown. We believe that future comparison between our relations and experimental dislocation strain energies may serve as verification and quantification of our relations.

A second application of the MPFC method developed in chapter 2 investigated a class of phenomena arising from phonon-defect interactions, we extended the modified phase crystal framework to incorporate additional strain dynamics. In diffusional phase field crystal techniques, the ballistic phonon related response is removed during the coarse graining procedure and thereby treated as instantaneous. Wave-like dynamics were thus introduced to transport stress information in the form of *quasi-phonons* [76]. This treatment permits a more detailed study of dislocation plasticity, especially in the limit of highly energetic defect structures found for example in shock

experiments or laser heating. Majaniemi *et al.* formed a theoretical connection of the two-time scale phase field crystal model to solid hydrodynamics, through vacancy and strain considerations [77]. Since no past descriptions, allowed for dynamic calculation of the strain, the strain contributions were assumed negligible. In highly deformed systems, such as polycrystals, or in systems exhibiting ballistics, strain corrections become increasingly relevant. With the strain filter introduced earlier in mind, we proceeded through an alternative derivation of two timescale approach than Majaniemi *et al.*. In particular, strain and strain rate factors were separated from chemical driving forces into a conditionally reversible stress This behaviour is akin to formulations in discrete dislocation dynamics simulations [99] and continuum dislocation models [100]. The mapping between hydrostatic strain and density, permits a single field partial differential equation capturing an additional order in the phononic response for qualitative mechanism analysis in shocked systems. In addition to the new modified phase field crystal model, we built an extension to the commonly used semi-implicit spectral method for rapid simulation.

One of the additions we made that is encapsulated in the conditionally reversible stress, is hydrostatic strain diffusion. This factor entered the free energy as the minimal strain-vacancy coupling. Such a component was argued necessary to recover the proper set of propagation modes in the hydrodynamic description of solids by Zippelius *et al.* [101]. For a lone dislocation, the hydrostatic strain points in the direction of the Burgers vector. As a consequence, we argued that mass motion emanating from hydrostatic strain diffusion, should allow differentiation between climb and glide time scales, which is a nonphysical feature of phase field crystal models [102]. In the works of Kun *et al.* that followed our publication ([1]), a similar argument was given for the time scale separation within the context of amplitude phase field crystal models [78]. It is interesting to note that climb occurs through vacancy diffusion, while glide occurs as a result of shear stress relaxation. We highlight that careful treatment of the vacancy and density couplings both thermodynamic and dynamic in origin, can correct some non-physical dislocation motion in phase field crystal models. Although this representation is minimal, one may be able to readdress the Hall-Petch and Cobble-creep phenomena for polycrystalline materials under strain.

We also described a procedure to introduce phonon dissipation into the model. Since the phase

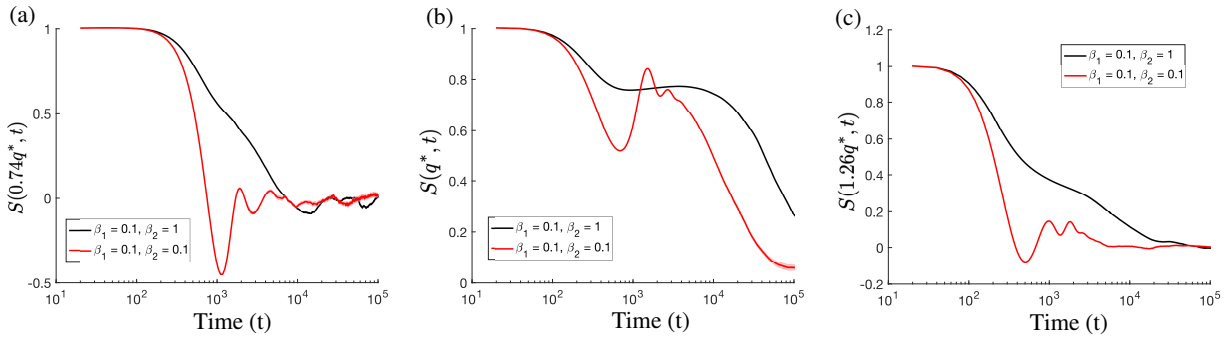

Figure 5.1: Illustrated is the autocorrelation function described in Eq. 3.3, measured for two different values of k^2 dissipation (β_2): (a) Measured at Fourier wavevector $q = 0.76q^*$. (b) Measured at the Bragg peak wavevector q^*. (c) Measured at Fourier wavevector $q = 1.26q^*$.

field crystal density represents a time averaged atomic distribution, it is expected that propagating phonons lose energy as they encounter short ranged vibrations, which are subsumed into the breadth of the atomic profiles. In addition, we note that phonons may encounter other point defect structures such as vacancies, which are captured in the atomic amplitude height. In idealized lattice, both thermal and phonon self scattering are known to scale with order $\mathcal{O}(k^2)$ [103]. Higher order corrections have also been argued when significant lattice deformation is present as in amorphous materials [104]. We subsequently performed a linear perturbative plane wave analysis, allowing analytic expression for the phonon dispersion. Due to linear dissipation, acting on all wavevector phonons, we observed the emergence of a k-gap for small wavevectors (k). This has been corroborated in recent hydrodynamic theories [105]. We further found a propagating mode cut-off at higher frequency resultant from the viscosity-like dissipation ($\mathcal{O}(k^2)$) in addition to a maxima of the phonon dispersion relation. This type of behaviour of the dispersion relation is indicative of a Van-Hove singularity, where the phonon density of states becomes singular. Such singularities are well-known to occur in crystalline materials and are indicative of sites that can store phonon energy. More complex amplitude phase field crystal models that simultaneously simulate large number of fields, have introduced viscous decay of the velocity and obtained similar dispersion relations [106]. We have thus illustrated a connection between the amplitude models and single field theories. Our analysis only considered the minimal wave dissipation order and linear response. As such, our model behaviours may deviate in disordered materials (glassy, amor-

phous, ...), which are known to have complex dispersion relations. We note that that some features may be captured in the nonlinear strain considerations described earlier.

In Fig. 5.1, the autocorrelation function is presented at three different wavevectors with different amounts of phonon viscosity (β_2). In connection with the memory formalism described in chapter 2, differing β_2 shift the decay time scale of the different wavevectors modes. As a result, the dynamics of defects, which are associated with a broad range of wavevectors can be greatly affected. A rough comparison to neutron scattering experiments that directly measure $S(q,t)$ can be performed to estimate an appropriate β_2 value. We thus treat the new thermal dissipation as a necessary and minimal approximation to study phonon-defect scattering.

The solid-liquid interface constitutes the first defect-type we investigated. For a specific set of driving conditions when phonon have sufficient relaxation time, the competition of lateral and parallel interface diffusion results in dendritic growth. The morphologies of which are greatly dependent on interface velocity, but grow with global symmetry associated with anisotropy of the atomic lattice structure. At rapid velocities, akin to splat cooling, vacancy trapping may ensue that embeds dislocations, metastable phases and vapour pockets into the growing solid [107, 108]. We thus simulated the solidification of a circular solid seed with differing phonon dissipations and temperature conditions. At slow growth rates and high dissipation, the conventional dendritic pattern was recovered. Meanwhile at rapid growth rates with decreased dissipation, the interface out sped the interfacial stress, leaving a dendritic network of dislocations fossilized into the solid structure. Furthermore, we noted the presence of additional dislocations and highly depleted regions that entered from fluctuations of the advancing interface. The trapped dislocations are in accordance with experimental observation. We believe the density depleted pools, may serve as sites of fracture or metastable phase formation in further corroboration with experiments. Such findings are likely readily available for phase field crystal models when additional phases at incorporated into the formalism. We note that the rapid growth conditions correspond to steady state interface growth in the diffusional models, which do not capture the aforementioned trapping mechanisms. Our first investigations have thus illustrated a class of phonon-defect coupling phenomena crucial for microstructure analysis in rapid solidification.

Chapter 3 constitutes further exploration of the new isothermal modified phase field crystal model introduced in chapter 2. Measurements of the density autocorrelation function revealed a two step exponential decay exhibited by polycrystals relaxing under large thermal noise strength. We illustrated that the crossover from phonon ballistics to structural relaxation was accompanied by phonon accumulation at grain-boundaries. The high local energies were shown sufficient to induce liquefaction, which would subsequently recrystallize. The character of the autocorrelation within the cross-over regime is indicative of experimentally observed boson peak which are often measured through the longitudinal phonon density of states. By means of a novel method to determine the longitudinal velocity, the longitudinal phonon density of states was shown measurable, in qualitative agreement with boson peak measurements. We further stimulated a number of polycrystalline samples by imposing an initial energy distribution. Liquefaction that was followed by subsequent recrystallization was observed. Upon increasing the imposed energy, an increase in the amount of recrystallization took place. For this scenario, we constructed a predictive relation for the maximally achieved defect fraction as a function of imposed initial energy.

Our simulations of polycrystal relaxation in the presence of large driving noise strength revealed a phonon-defect caging regime in the intermediate scattering function. That is, a multi-stage stretched exponential-like curvature, similar to binary caging reported by Berry *et al.* [91]. We note that the intermediate scattering function is also known as the density autocorrelation, which measures the self-similarity of the atomic profile. Our findings are consistent with molecular dynamic simulations of Ni polycrystals that exhibited similar two time-scale behaviour [109]. Because of the lack of phonon grain boundary scattering, we illustrated that the caging regime was missing from the relaxation of idealized lattices. One way thus to interpret the two-time response from a coarse-grained perspective, is as a departure from the self-averaging assumption of the noise correlations. In particular, this results from phonons softening and localizing their energies near defect structures; a defect limited motion of phonons. It is interesting to note that two-time scale responses are commonly exhibited by glass and amorphous materials. As a result, we suspect increasing the defect densities in polycrystalline materials, will lead to an increased resemblance to their metallic glassy counterparts. The observations we have made are mainly qualitative, requir-

ing a careful treatment of grain boundary energy to connect to any quantitative material, perhaps through the dislocation strain energies described earlier. We leave the study of how changing the polycrystal grain size and grain boundary energy affect the phonon spectrum to future works.

In addition to the glassy-like properties of polycrystals, we found that phonon-defect scattering can result in disordered pools that suppress further ballistic scattering, and coarsen after formation. Because of the phonon suppression, the disordered regions may be related to the ringing of the dynamic structure factor during the crossover from ballistic to diffusive motion. We found that a decrease in disordered pool count occurred in conjunction with an increase in phonon dissipation. While the melt pools appear to form on grain boundaries, they can also form along slip planes of the host lattice structure when two grain boundaries are close to one another. These liquid pools recrystallize on longer timescales than their formation, potentially annealing into dislocations. Defect dimensionality can have a large impact on the associated formation energy. Since our simulations are two dimensional, dislocations would have a higher energy to dissociate. Thus, in three dimensions we believe that it is more likely to relax by emission of Shockley partials. Nonetheless, if enough energy has locally accumulated, liquefaction or fracturing will ensue. The autocorrelation function is directly accessible in neutron scattering experiments. Here the two time scale response and ringing have been observed, with the latter often denoted the boson peak. There has been debate in the literature as to the cause of the boson peak. Our simulations suggest that the nature of boson peak is caused by grain boundary dissociation from phonon defect interaction. To further corroborate our findings, we sought alternative descriptors of the boson peak.

The boson peak additionally appears as a peak in the phonon density of states, measured either in inelastic neutron scattering or Raman spectroscopy. Through the use of Helmholtz decomposition, we interrelated the time derivative of the density field to the longitudinal momentum. Within the context of past single field phase field crystal models, the velocity had been unobtainable. We illustrated that this metric permits the evaluations of the system kinetic energy and longitudinal phonon density of states. Further analysis of the phonon scattering spectrum through the longitudinal phonon density of states, revealed the emergence of a boson peak. In the case of the lower dissipation, and thereby phonon density, we found additional peaks. We suspect these features

are Van-Hove singularities, which we showed were controllable through the viscous dissipation. The position of the dominant boson peak was observed to be unaffected by the wavevector of the phonon dispersion maxima, which is associated with the Van-Hove singularity. This finding corroborates the distinction between the Van-Hove singularity of the idealized lattice and the boson peak [110]. We note that our dispersion analysis was a linear approximation and did not account for the presence of grain boundaries. It remains a possibility that the grain boundary introduces additional van-hove singularities to the system. Nonetheless, in connection with our past finding, the boson peak seems to be caused by phonon accumulation at grain-boundaries. We further note that the peak may be an artifact of the approximations that went into deriving the density of states equation. As a result, further metrics to connect the high frequency peak may be necessary. In particular, low frequency shear waves may interact with the longitudinal modes. Importantly, the shape of the resonance peaks are qualitatively consistent with a maximal envelope of the experimental measurements of laser irradiated thin films, which are measuring the process at much shorted time scales [82, 111]. Waldecker *et al.* further highlight the dominant activity of the longitudinal acoustic modes, such as those we have been able to measure [82]. More intricate hydrodynamic amplitude variants of the phase field crystal model that explicitly track the velocity vector field may be able to elucidate the shear contributions.

In comparison to thermal annealing pathways for recrystallization, a material may be recrystallize as a result from a passing shock wave. The transmitted energy may have resulted from induced mechanical deformation, for example in rolling, or alternatively from laser irradiation. In the context of phase field crystals, such energy may be added near instantaneously. Thus to model the propagation of a shock wave, we make the minimal approximation, that at a given time step, a distribution of momentum is implanted in lattice. Upon relaxation, we found a similar appearance of disordered structures, followed by recrystallization. Some recent additive manufacturing experiments corroborate the shocked induced recrystallization pathway [84]. When applying an increasing amount of burst energy to a number of polycrystalline samples, we found an increase in the amount of metastable pools formed. By measuring the defect fraction, we found that over time the defects coarsened away. We then made a rate relation for the maximally achieved defect

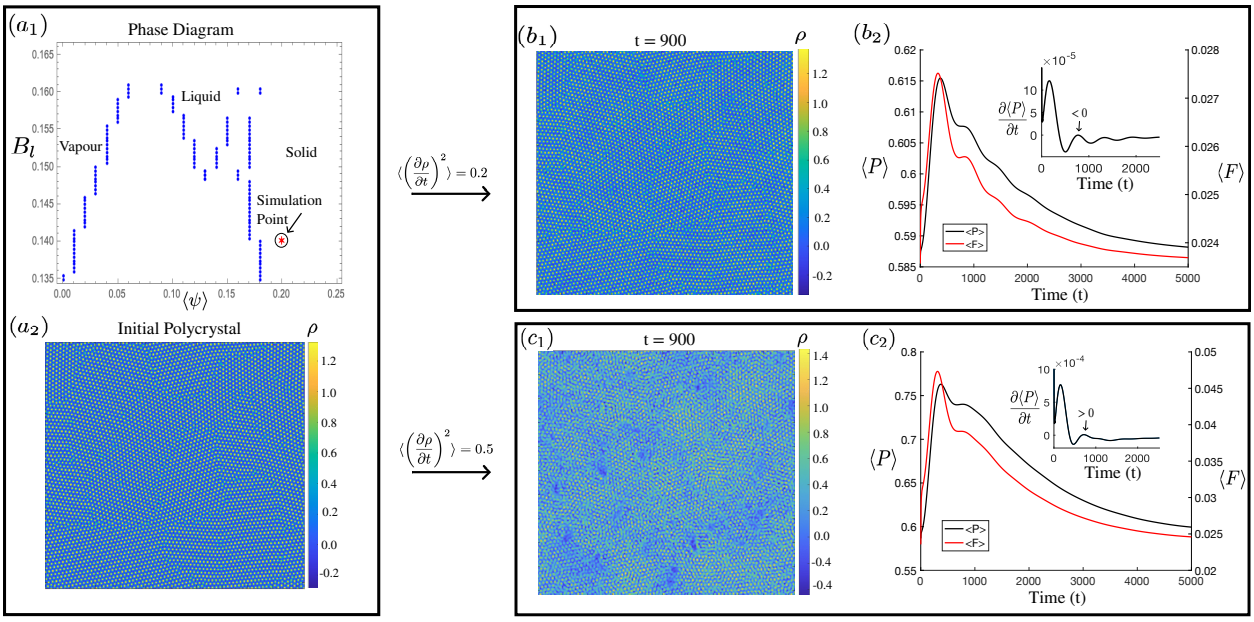

Figure 5.2: Illustrated is an example simulation of laser induced melting and voiding as studied in chapter 3. A vapour phase field crystal model is used with parameters as in figure 1 of ref. [57]. (a_1) A phase diagram is shown in terms of the effective temperature B_l and average density $\langle\psi\rangle$. (a_2). The initial polycrystalline density maps. Subpanels b_i and c_i refer to simulations with different amounts of input energy. (b_1) The density map snapshot at $t = 900$. (b_2). The temporal evolution of average pressure, $\langle P\rangle$, and average free energy, $\langle F\rangle$. (c_1). The density map snapshot at $t = 900$. (c_2) The temporal evolution of average pressure, $\langle P\rangle$, and average free energy, $\langle F\rangle$. An inset is provided for subpanels (b_2) and (c_2) illustrating the slope of the average pressure.

fraction, since this is a rough indicator of the amount of recrystallization. We found very good agreement to our simulations with our rate relation for low input energies. At extreme input energies, we believe that the phase field crystal model breaks down, because of large density jumps. It is interesting to note that our time dependent rate relation shares similarities to Oswald ripening theories [112]. Meanwhile the energy rate relation has similar qualitative form to experimental measurements of the recrystallization fraction for steel [113]. However, a more quantitative validation of our results with experiments requires the inclusion of latent heat and heat flow to extend the theory and account for consistent coarsening time-scales. In addition, multiple phases may be necessary to account for fracture or precipitate formation, both of which are parasitic to the recrystallization [114]. Nonetheless, our studies on recrystallization pathways, are indicative of phonon

defect coupling being a culprit.

In Fig. 5.2, we illustrate an example of laser induced voiding that we previously mentioned. Such fracture response can occur in highly irradiated materials. We use the model described by Kocher *et al.* for the inclusion of a vapour phase into the free energy landscape [57]. As before, an initial polycrystal is grown, which we bombarded with different amounts of kinetic energy that is input through $\langle\left(\frac{\partial\rho}{\partial t}\right)^2\rangle$. With reduced input energy, for which no vapor pockets form, phonons continually scatter of defect structures (b_1). As a result, we observe ringing in the average system pressure (b_2). As vapor pockets form in response to the induced shock (c_1), additional dissipation of the disturbance can be seen in subpanel (c_2). Furthermore, we note the presence of a peak in the average system pressure, which only appears when the polycrystal fractured. A potential explanation for this behaviour is due to the system overcoming an energy barrier to recrystallize. However we note that the simulations contained in Fig. 5.2 represent only a single instance of induced noise. Thus to further corroborate this behaviour proper statistics need to obtained for different instances of noise and polycrystalline structure. Irregardless, we illustrated the potential for the inclusion of a vapour phase for the study of fracture in laser induced irradiation.

Chapter 4 expounded upon our hydrodynamic formalism of our previous works by the inclusion of a temperature field of kinetic and entropic origins. In comparison to past thermal phase field crystal models, enthalpic latent heat release is incorporated, in addition to phonon dynamics. Upon spatial coarse-graining, it is shown that the method recovers the decay scale order of the one-dimensional analytic temperature interface profile for steady state solidification. We further illustrated that the coarse-grained density field contains information of equilibrium vacancy concentration within the modulation amplitude heights. A vacancy gradient is illustrated to be emergent from applying a fixed temperature gradient across a solid sample. Such behaviour is argued indicative of the constant volume nature of typical phase field crystal methods. The technique serves as a tool for future investigation of temperature induced plasticity evolution, or phonon generation. To this end, we illustrated heat generation from phase transitions, plastic relaxation, and phonon dissipation. Furthermore, we describe the connection between parameters entering our free energy in terms of the thermomechanical equations of state. In summary, we illustrated how

temperature flow can become slaved to mass and phonon diffusion.

Seldom are solidification and plasticity isothermal. Latent heat release and ambient heating can greatly shift a material temperatures. Temperature gradients can induce vacancy flow [115] or can be tailored to control solidification rates [116]. Additionally, grain boundary morphologies may differ as a result of the heating route of an experimental apparatus. If heating is hyper localized, a different local thermodynamics may be sampled, allowing metastable phase formation. Thus it is imperative both on qualitative and quantitative grounds to incorporate temperature effects. Langer *et al.* have in past mentioned the importance of a model that can incorporate temperature effects in addition to phonons and plasticity [100, 117]. We have hence built a framework that extends the phononic phase field crystal model, incorporating temperature dynamics that obey energy conservation. We note that energy can be stored at faster and smaller scales than our simulation resolution, which through noise can lead to a breaking of the symmetry. As far as we are aware, temperature field crystal represents the first coupling between the two time scale models and temperature. This allows a new paradigm of investigations of the aforementioned experiments. During the inception, care was taken to include all temperature dependent contributions entering the free energy from classical density functional theory. In addition, an added enthalpic heat contribution was required to conform to Clausius-Clapeyron relation. We note that earlier class of temperature phase field crystal models do not abide to the thermodynamic constraints, and as such suffer from an ill defined latent heat [118–120]. We showed that a rough agreement could be made between analytic temperature profiles encountered in sharp-interface limits for steady state solidification. It remains as an interesting question to compare the temperature profiles obtained in finer scale models to our results. Nonetheless, this technique lays a foundation for many future avenues of exploration. In particular, we are interesting in the applying our methods to describe additive manufacturing experiments, which we leave for future work.

There has been evidence suggesting residual thermal stress, associate to thermal expansion, during solidification may be cause for significant number of failure mechanisms in metal manufacturing. Thermal expansion is generally interpreted as a change of lattice length, in order to conform to the constant environmental pressure. Previous attempts introduce thermal expansion explicitly

into phase field crystal free energy, with equilibrium lattice length that changes as a function of temperature [120]. However, we illustrated that phase field crystal energies already contain thermal expansion characteristics. Namely, they need to be interpreted as isochoric, with fixed number of lattice site positions. Under this interpretation, changes in the amplitude magnitudes, which represent an increase in localized vibrations can be related to vacancy flow. Applying a fixed thermal gradient across an idealized lattice results in an opposing gradient in amplitude height. This is in qualitative agreement with vacancy flow experiments which have been performed on a number of materials [115]. We have thus addressed where thermal stress is buried in phase field crystal models. In passing, we described how different model parameters are related to thermomechanical variables used in experiments in terms of the Gruneisen equation of state theory. Future work may expand on these relations to fit the phase field crystal free energy through databases such as that tabulated by Dinsdale [121]. We mention that this process is not dissimilar from the quantification of molecular dynamics through shock-Hugoniot response [122]. We note that constant pressure ensembles should exhibit thermal expansion characteristics provided sufficiently small numeric grid spacing [123]. It remains to perform a quantitative comparison of amplitude temperature dependence to the equilibrium vacancy concentration.

As a liquid transitions to the solid state, there is a corresponding release of entropic heat. It stands to reason that any metastable state relaxing towards equilibrium should also release a corresponding heat, perhaps negligible relative to the full solidification. We hypothesis this behaviour as a time scale coupling phenomena, since heat production is being limited by internal stress relaxation. Recently, the recalescence cooling curve has been argued as a metric to assess the critical nucleus size during nucleation [124]. However the recalescence curve can be connected to time-temperature-transformation (TTT) and dislocation-dynamics diagrams often used for metallurgical dislocation analysis. With the new TFC formulation, we simulated the constant uniform cooling of a liquid past the transition temperature. A characteristic recalescence profile was recovered. In addition, we highlighted asymmetry present within the slope of the average system temperature as a function of time. We then showed that heat release can be caused by two additional sources in the solid-state, namely dislocation annihilation and phonon scattering. To illustrate dislocation heat

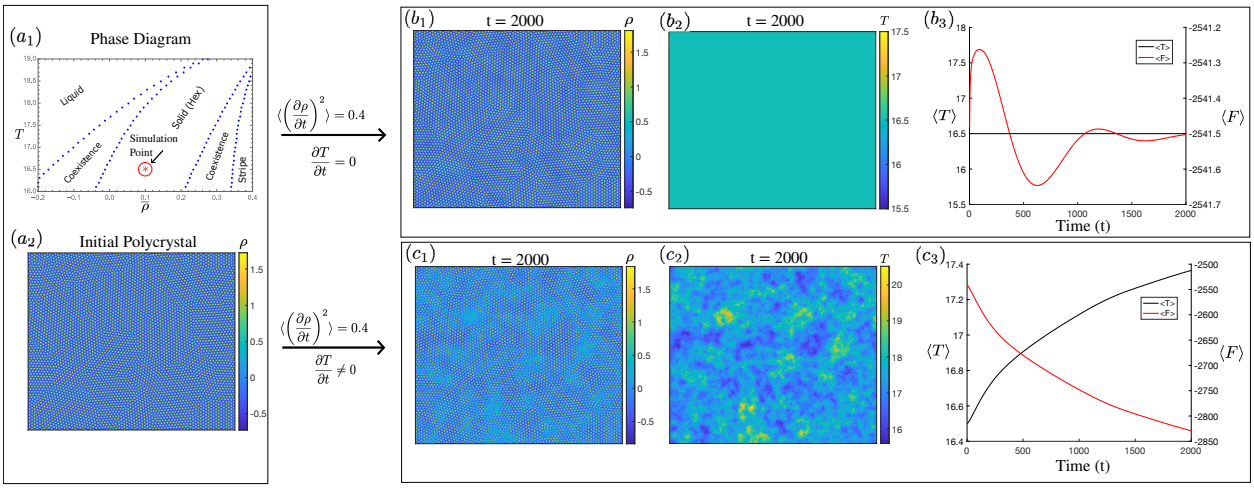

Figure 5.3: Illustrated is a comparison of the laser irradiation mechanisms with (c_i) and without (b_i) the evolution of a thermal field. The model parameters used are as listed for in table 4.1 for figure 4.3 with $S(x,t) = 0$, and $\alpha_T = 2000$. (a_1) The phase diagram computed with a one mode expansion formulation. (a_2) The initial polycrystalline sample prepared at uniform temperature and average density as denoted by the simulation point in subpanel (a_1). (b_1) The density map at $t = 2000$. (b_2) The temperature map at $t = 2000$. (b_3) The temporal evolution of average temperature, $\langle T \rangle$, and average free energy, $\langle F \rangle$. (c_1) The density map at $t = 2000$. (c_2) The temperature map at $t = 2000$. (c_3) The temporal evolution of average temperature, $\langle T \rangle$, and average free energy, $\langle F \rangle$.

generation, we simulated the annealing of a polycrystalline solid with an initial uniform temperature distribution. Here we observed temperature increase that was congruent to free energy drops associated with the dislocation motion and grain boundary coarsening. Our findings suggests that the asymmetry of the heat generation may be caused by the dislocation relaxation following grain impingement. The slope of the recalescence curve may thus be a non-invasive method of obtaining the dislocation density following solidification. In addition, we illustrated that during rapid melting of a polycrystalline solid, the reverse recalescence curve can be split into two time-scale regimes, where one is dominated by transformative heat generation, and the other by phonon scattering within the remaining solid islets.

With the addition of temperature, we may now, return to the study of laser induced irradiation. In comparison to existing two-temperature models [125], the thermal framework that we have de-

veloped can be used to observe when changes of crystalline order ensue. As we have argued, our framework further allows a description of induced thermal pressure. To this end, we simulated the response of a polycrystal to the input of kinetic energy with and without temperature dynamics. The simulation is captured in Fig. 5.3, but only represents a minimal example. For isothermal response, the input kinetic energy is dissipated into the lattice by modulations of amplitude height as seen in subpanel (b_1). However, when the thermal field is allowed to evolve, the input kinetic energy is transferred into modulations of temperature. Such behaviour can be observed in subpanels (c_1) and (c_2). In certain places in the lattice the temperature can exceed the melting point and liquidation follows. The absorption of heat for the transformation results in sudden decrease in the rate of average temperature increase (c_3). We note that the average temperature exceeds the liquidus line along our average density. Our simulations are representative of an isolated two dimensional polycrystal. To compare against experiments we must additional incorporate heat loss, which is possible through $S(t)$. Such considerations are necessary, but not used in our minimal example simulation. Once sufficient heat has been lost to the surrounding environment, recrystallization may follow. We note that our simulation has only considered the case of low latent heat barrier for transformation. Thus it remains to investigate the response when the phase transformation barrier is larger. We expect that the temperature dynamics may have reduced importance. It may be of further interest to measure the recrystallization fraction as a function of the cooling rate considered.

Our studies of temperature, vacancy, and density dynamics has only highlighted a select number of phenomena that could arise. Throughout this discussion, we have documented a number of future applications and improvements that can extend our specific formalism. However, we have only described the tip of an iceberg. What occurs when additional phases or alternative species are introduced into the system remains unknown. How short scale interaction play a role on the solidification and plasticity is a further question of interest, perhaps requiring a careful treatment of noise. Further investigation may add non-linear advection to describe a whole new class of response. Additional information of time scale coupling characteristics may perhaps lie in measuring cross correlation functions, such as between density and temperature. System outside of

metallics may additionally exhibit multi-time scale related phenomena. In multiferroic materials for example, propagating magnetization and polarization interfaces become limited in the presence of defect structure. Alternatively, complex polymer crystallization, in food science, plastics, biological systems, or electronics may also exhibit a complex temporal evolution.

Chapter 6

Conclusion

Through our studies of hydrodynamic extensions of the phase field crystal models, a number of improvements and measurements of time coupling phenomena have been explored. We have built frameworks, and numeric methods to delve into the cross correlated dynamics of vacancy, temperature, and density. In passing, we have also introduced a number of novel metrics to connect our simulations with experimental measurements. Thereby, we have provided explanation for structural evolution mechanisms and posited new systems for future experimental exploration.

A number of research avenues are readily accessible for future analysis. The repetition of the noise induced shock performed in Ch. 4 over a range of different material conditions represents one direction to explore. This is of particular relevance, since the characterization of the recrystallization fraction as a function of the system average temperature, pressure, and density is of industrial importance. One may further expand on the description by incoporating an additional solute species, which may affect the recrystallization, and potentially precipitate out of the host lattice. Such behaviour would be in accordance with recrystallization experiments [114], but additional correlations between the phenomenon and material properties may be drawn. Supplemented by heat transfer kinetics, the effect of thermal expansion stress on nano- and microstructure in the presence of precipitates may also be assessed. An alternative class of work falls under hysteretic response, where the reaction of the system lags behind the induced stimulus. As in quenching experiments, suppose the system temperature is gradually modified. Depending on the rate of tem-

perature change, the material may exhibit a structural frustration. In the future, a characterization of this behaviour can be analyzed through the frameworks discussed in this thesis. A similar hysteresis response would be found in the magnetization as a function of the externally applied field. In addition to rate dependence, there can be sources of frustrated evolution as the magnetization response encounters dislocations and grain boundaries. An analysis of this Barkhausen noise effect through a magnetization and polarization extension of the phase field crystal model may allow correlating the effect with the material defect density. Lastly, we shall mention the possibility of investigating high spatial resolution periodic surface patterns produced as the polarization of a stimulating laser couples to the magnetization and polarization of the material. As in the earlier description, one may employ a multi-ferroic phase field crystal extension coupled to an external laser source in order to characterize the patterns on a solid-liquid interface.

In summary, we have illustrated the difficulty in studying structural transformations due to the many competing time scales. Our work emphasizes that time scale competition can not only lead to new phenomena, but is at the heart of a significant number of challenges in the manufactory of materials. Some such behaviour may be subject of future study with industrial applications. At the scale of our investigations, it seems that the essence of this class of behaviours, lies in how energy is transferred through atomic interactions, further emphasizing the necessity to examine the dance of atoms innumerable at time and length scales beyond our vision, *i.e.,* the atomic scale shuffle.

Bibliography

[1] D. Burns, N. Provatas, and M. Grant. “Time-scale investigation with the modified phase field crystal method”. In: *Modelling Simulation Material Science and Engineering* 30 (6 2022), p. 064001. DOI: 10.1088/1361-651X/ac7c83.

[2] D. Burns, N. Provatas, and M. Grant. “Two-dimensional phase field crystal simulation of laser-induced recrystallization: A mechanism of grain-boundary phonon scattering and softening”. In: *Physical Review Materials* 7 (8 2023), p. 083402. DOI: 10.1103/PhysRevMaterials.7.083402.

[3] J. R. MacDonald. “Some Simple Isothermal Equations of State”. In: *Review Modern Physics* 38 (4 1966), pp. 669–679. DOI: 10.1103/RevModPhys.38.669.

[4] M. Hillert. *Phase Equilibria, Phase Diagrams and Phase Transformations: Their Thermodynamic Basis*. Phase Equilibria, Phase Diagrams, and Phase Transformations: Their Thermodynamic Basis. Cambridge University Press, 1998. ISBN: 9780521565844.

[5] J. R. MacDonald. “Review of Some Experimental and Analytical Equations of State”. In: *Review Modern Physics* 41 (2 1969), pp. 316–349. DOI: 10.1103/RevModPhys.41.316.

[6] J. J. Gilvarry. “The Lindemann and Grüneisen Laws”. In: *Physical Review* 102 (2 1956), pp. 308–316. DOI: 10.1103/PhysRev.102.308.

[7] J. J. Gilvarry. “Grüneisen Parameter for a Solid under Finite Strain”. In: *Physical Review* 102 (2 1956), pp. 331–340. DOI: 10.1103/PhysRev.102.331.

[8] J. J. Gilvarry. “Temperature-Dependent Equations of State of Solids”. In: *Journal of Applied Physics* 28.11 (2004), pp. 1253–1261. ISSN: 0021-8979. DOI: 10.1063/1.1722628.

[9] O. L. Anderson. “Equation for thermal expansivity in planetary interiors”. In: *Journal of Geophysical Research (1896-1977)* 72.14 (1967), pp. 3661–3668. DOI: https://doi.org/10.1029/JZ072i014p03661.

[10] L. Knopoff and J. N. Shapiro. “Comments on the interrelationships between Grüneisen’s parameter and shock and isothermal equations of state”. In: *Journal of Geophysical Research (1896-1977)* 74.6 (1969), pp. 1439–1450. DOI: https://doi.org/10.1029/JB074i006p01439.

[11] N. Saunders and A. P. Miodownik. *CALPHAD (Calculation of Phase Diagrams): A Comprehensive Guide*. ISSN. Elsevier Science, 1998. ISBN: 9780080528434.

[12] A. van de Walle, C. Nataraj, and Z. Liu. “The Thermodynamic Database Database”. In: *Calphad* 61 (2018), pp. 173–178. ISSN: 0364-5916. DOI: https://doi.org/10.1016/j.calphad.2018.04.003.

[13] B. J. Alder and T. E. Wainwright. “Studies in Molecular Dynamics. I. General Method”. In: *The Journal of Chemical Physics* 31.2 (2004), pp. 459–466. ISSN: 0021-9606. DOI: 10.1063/1.1730376.

[14] M. Karplus and J. A. McCammon. “Molecular dynamics simulations of biomolecules”. In: *Nature Structural Biology* 9.9 (2002), pp. 646–652. DOI: 10.1038/nsb0902-646.

[15] J.J. Hoyt, Z.T. Trautt, and M. Upmanyu. “Fluctuations in molecular dynamics simulations”. In: *Mathematics and Computers in Simulation* 80.7 (2010). Multiscale modeling of moving interfaces in materials, pp. 1382–1392. ISSN: 0378-4754. DOI: https://doi.org/10.1016/j.matcom.2009.03.012.

[16] S. Yin et al. “Atomistic simulations of dislocation mobility in refractory high-entropy alloys and the effect of chemical short-range order”. In: *Nature Communications* 12.1 (2021), p. 4873.

[17] M. J. Field, P. A. Bash, and M. Karplus. “A combined quantum mechanical and molecular mechanical potential for molecular dynamics simulations”. In: *Journal of Computational Chemistry* 11.6 (1990), pp. 700–733. DOI: https://doi.org/10.1002/jcc.540110605.

[18] L. J. Porter, J. F. Justo, and S. Yip. “The importance of Grüneisen parameters in developing interatomic potentials”. In: *Journal of Applied Physics* 82.11 (1997), pp. 5378–5381. ISSN: 0021-8979. DOI: 10.1063/1.366305.

[19] P. Seleson et al. “Peridynamics as an Upscaling of Molecular Dynamics”. In: *Multiscale Modeling & Simulation* 8.1 (2009), pp. 204–227.

[20] J. P. Hansen and I. R. McDonald. *Theory of Simple Liquids*. Elsevier Science, 2006. ISBN: 9780080455075.

[21] R. Zwanzig. “Memory Effects in Irreversible Thermodynamics”. In: *Physical Review* 124 (4 1961), pp. 983–992. DOI: 10.1103/PhysRev.124.983.

[22] H. Mori. “Transport, Collective Motion, and Brownian Motion*)”. In: *Progress of Theoretical Physics* 33.3 (1965), pp. 423–455. ISSN: 0033-068X. DOI: 10.1143/PTP.33.423.

[23] L. P. Kadanoff and P. C. Martin. “Hydrodynamic equations and correlation functions”. In: *Annals of Physics* 24 (1963), pp. 419–469. ISSN: 0003-4916. DOI: https://doi.org/10.1016/0003-4916(63)90078-2.

[24] P. C. Martin, O. Parodi, and P. S. Pershan. “Unified Hydrodynamic Theory for Crystals, Liquid Crystals, and Normal Fluids”. In: *Physical Review A* 6 (6 1972), pp. 2401–2420. DOI: 10.1103/PhysRevA.6.2401.

[25] P. D. Fleming and C. Cohen. “Hydrodynamics of solids”. In: *Physical Review B* 13 (2 1976), pp. 500–516. DOI: 10.1103/PhysRevB.13.500.

[26] G. Szamel and M. H. Ernst. “Slow modes in crystals: A method to study elastic constants”. In: *Physical Review B* 48 (1 1993), pp. 112–118. DOI: 10.1103/PhysRevB.48.112.

[27] C. Walz and M. Fuchs. “Displacement field and elastic constants in nonideal crystals”. In: *Physical Review B* 81 (13 2010), p. 134110. DOI: 10.1103/PhysRevB.81.134110.

[28] J. P. Boon and S. Yip. *Molecular Hydrodynamics*. Dover books on physics. Dover Publications, 1991. ISBN: 9780486669496.

[29] M. J. Shelley and T. Ueda. “The Stokesian hydrodynamics of flexing, stretching filaments”. In: *Physica D: Nonlinear Phenomena* 146.1 (2000), pp. 221–245. ISSN: 0167-2789. DOI: https://doi.org/10.1016/S0167-2789(00)00131-7.

[30] J. Frenkel. *Kinetic Theory of Liquids*. Peter Smith Publisher, Incorporated, 1984. ISBN: 9780844620947.

[31] T. J. Yoon et al. ““Two-Phase”Thermodynamics of the Frenkel Line”. In: *The Journal of Physical Chemistry Letters* 9.16 (2018), pp. 4550–4554.

[32] P.M. Chaikin and T.C. Lubensky. *Principles of Condensed Matter Physics*. Cambridge University Press, 2000. ISBN: 9780521794503.

[33] R. Kubo. “The fluctuation-dissipation theorem”. In: *Reports on Progress in Physics* 29 (1966), pp. 255–284.

[34] P. C. Hohenberg and B. I. Halperin. “Theory of dynamic critical phenomena”. In: *Review Modern Physics* 49 (3 1977), pp. 435–479. DOI: 10.1103/RevModPhys.49.435.

[35] P. G. Saffman and G. I. Taylor. “The penetration of a fluid into a porous medium or Hele-Shaw cell containing a more viscous liquid”. In: *Proceedings of the Royal Society of London. Series A. Mathematical and Physical Sciences* 245.1242 (1958), pp. 312–329.

[36] W. W. Mullins and R. F. Sekerka. “Stability of a Planar Interface During Solidification of a Dilute Binary Alloy”. In: *Journal of Applied Physics* 35.2 (1964), pp. 444–451. DOI: 10.1063/1.1713333.

[37] M. A. Grinfeld. “The stress driven instability in elastic crystals: Mathematical models and physical manifestations”. In: *Journal of Nonlinear Science* 3.1 (1993), pp. 35–83.

[38] I. Cantat et al. “Directional solidification under stress”. In: *Physical Review E* 58 (5 1998), pp. 6027–6040. DOI: 10.1103/PhysRevE.58.6027.

[39] K. R. Elder and M. Grant. “Modeling elastic and plastic deformations in nonequilibrium processing using phase field crystals”. In: *Physical Review E* 70 (5 2004), p. 051605. DOI: 10.1103/PhysRevE.70.051605.

[40] T. V. Ramakrishnan and M. Yussouff. “First-principles order-parameter theory of freezing”. In: *Physical Review B* 19 (5 1979), pp. 2775–2794. DOI: 10.1103/PhysRevB.19.2775.

[41] R. Evans. “The nature of the liquid-vapour interface and other topics in the statistical mechanics of non-uniform, classical fluids”. In: *Advances in Physics* 28.2 (1979), pp. 143–200.

[42] Y. Singh. “Density-functional theory of freezing and properties of the ordered phase”. In: *Physics Reports* 207.6 (1991), pp. 351–444. ISSN: 0370-1573. DOI: 10.1016/0370-1573(91)90097-6.

[43] A. J. Archer et al. “Deriving phase field crystal theory from dynamical density functional theory: Consequences of the approximations”. In: *Physical Review E* 100 (2 2019), p. 022140. DOI: 10.1103/PhysRevE.100.022140.

[44] J. K. Percus and G. J. Yevick. “Analysis of Classical Statistical Mechanics by Means of Collective Coordinates”. In: *Physical Review* 110 (1 1958), pp. 1–13. DOI: 10.1103/PhysRev.110.1.

[45] P. Tarazona. “A density functional theory of melting”. In: *Molecular Physics* 52.1 (1984), pp. 81–96.

[46] R. Roth. “Fundamental measure theory for hard-sphere mixtures: a review”. In: *Journal of Physics: Condensed Matter* 22.6 (2010), p. 063102.

[47] M. Oettel et al. “Description of hard-sphere crystals and crystal-fluid interfaces: A comparison between density functional approaches and a phase-field crystal model”. In: *Physical Review E* 86 (2 2012), p. 021404. DOI: 10.1103/PhysRevE.86.021404.

[48] K. Wu, A. Adland, and A. Karma. “Phase-field-crystal model for fcc ordering”. In: *Physical Review E* 81 (6 2010), p. 061601.

[49] A. Jaatinen and T. Ala-Nissila. “Eighth-order phase-field-crystal model for two-dimensional crystallization”. In: *Physical Review E* 82 (6 2010), p. 061602. DOI: 10.1103/PhysRevE.82.061602.

[50] Z. Wang, Z. Liu, and Z. Huang. “Angle-adjustable density field formulation for the modeling of crystalline microstructure”. In: *Physical Review B* 97 (18 2018), p. 180102.

[51] Z. Wang et al. “Control of phase ordering and elastic properties in phase field crystals through three-point direct correlation”. In: *Physical Review E* 105 (4 2022), p. 044802. DOI: 10.1103/PhysRevE.105.044802.

[52] M. Greenwood, N. Provatas, and J. Rottler. “Free Energy Functionals for Efficient Phase Field Crystal Modeling of Structural Phase Transformations”. In: *Physical Review Letters* 105 (4 2010), p. 045702. DOI: 10.1103/PhysRevLett.105.045702.

[53] M. Seymour. *Study of multi-point interactions in PFC models for complex structural transformations*. McGill University (Canada), 2018.

[54] A. Jaatinen et al. “Thermodynamics of bcc metals in phase-field-crystal models”. In: *Physical Review E* 80 (3 2009), p. 031602. DOI: 10.1103/PhysRevE.80.031602.

[55] V.W.L. Chan, N. Pisutha-Arnond, and K. Thornton. “Thermodynamic relationships for homogeneous crystalline and liquid phases in the phase-field crystal model”. In: *Computational Materials Science* 135 (2017), pp. 205–213. ISSN: 0927-0256. DOI: https://doi.org/10.1016/j.commatsci.2017.04.017.

[56] Jesper Mellenthin, Alain Karma, and Mathis Plapp. “Phase-field crystal study of grain-boundary premelting”. In: *Physical Review B* 78 (18 2008), p. 184110. DOI: 10.1103/PhysRevB.78.184110.

[57] G. Kocher and N. Provatas. “New Density Functional Approach for Solid-Liquid-Vapor Transitions in Pure Materials”. In: *Physical Review Letters* 114 (15 2015), p. 155501. DOI: 10.1103/PhysRevLett.114.155501.

[58] M. J. Frick, E. Wilson, and N. Provatas. “Consistent representation of vapor phases in phase field crystal dynamics”. In: *Physical Review Materials* 7 (2 2023), p. 023405. DOI: 10.1103/PhysRevMaterials.7.023405.

[59] J. S. Langer. “Instabilities and pattern formation in crystal growth”. In: *Review Modern Physics* 52 (1 1980), pp. 1–28. DOI: 10.1103/RevModPhys.52.1.

[60] L. Q. Chen. “Phase-Field Models for Microstructure Evolution”. In: *Annual Review of Materials Research* 32.1 (2002), pp. 113–140.

[61] Author Torquato S. and HW. Jr. Haslach. “Random Heterogeneous Materials: Microstructure and Macroscopic Properties”. In: *Applied Mechanics Reviews* 55.4 (2002), B62–B63. ISSN: 0003-6900. DOI: 10.1115/1.1483342.

[62] A. J. Clarke et al. “Microstructure selection in thin-sample directional solidification of an Al-Cu alloy: In situ X-ray imaging and phase-field simulations”. In: *Acta Materialia* 129.C (2017), pp. 203–216.

[63] S. V. Rodriguez et al. “Phase-field modeling of austenitic steels used in turbines”. In: *IOP Conference Series: Materials Science and Engineering* 1281.1 (2023), p. 012047.

[64] K. Ji et al. “Microstructural Pattern Formation during Far-from-Equilibrium Alloy Solidification”. In: *Physical Review Letters* 130 (2 2023), p. 026203. DOI: 10.1103/PhysRevLett.130.026203.

[65] L. Gránásy et al. “Phase-field modeling of crystal nucleation in undercooled liquids – A review”. In: *Progress in Materials Science* 106 (2019), p. 100569.

[66] L. Gránásy et al. “Phase-field crystal modelling of crystal nucleation, heteroepitaxy and patterning”. In: *Philosophical Magazine* 91.1 (2011), pp. 123–149.

[67] P. Jreidini, G. Kocher, and N. Provatas. “Classical nucleation theory in the phase-field crystal model”. In: *Physical Review E* 97 (4 2018), p. 042802.

[68] G. I. Tóth et al. “Polymorphism, crystal nucleation and growth in the phase-field crystal model in 2D and 3D”. In: *Journal of Physics: Condensed Matter* 22.36 (2010), p. 364101. DOI: 10.1088/0953-8984/22/36/364101.

[69] F. Podmaniczky and L. Gránásy. “Molecular scale hydrodynamic theory of crystal nucleation and polycrystalline growth”. In: *Journal of Crystal Growth* 597 (2022), p. 126854.

[70] A. Mamaev and N. Provatas. “Analysis of the Self-Consistency of Nucleation in the Diffuse Interface Limit of Phase Field Models”. In: *Modelling Simulation Material Science Engineering* (in press).

[71] K. R. Elder et al. “Phase-field crystal modeling and classical density functional theory of freezing”. In: *Physical Review B* 75 (6 2007), p. 064107. DOI: 10.1103/PhysRevB.75.064107.

[72] K. Wu and P. W. Voorhees. “Phase field crystal simulations of nanocrystalline grain growth in two dimensions”. In: *Acta Materialia* 60.1 (2012), pp. 407–419.

[73] V. Skogvoll, M. Salvalaglio, and L. Angheluta. “Hydrodynamic phase field crystal approach to interfaces, dislocations, and multi-grain networks”. In: *Modelling Simulation Material Science and Engineering* 30 (8 2022), p. 084002. DOI: 10.1088/1361-651X/ac9493.

[74] J. Berry, M. Grant, and K. R. Elder. “Diffusive atomistic dynamics of edge dislocations in two dimensions”. In: *Physical Review E* 73 (3 2006), p. 031609. DOI: 10.1103/PhysRevE.73.031609.

[75] J. Berry et al. “Defect stability in phase-field crystal models: Stacking faults and partial dislocations”. In: *Physical Review B* 86 (22 2012), p. 224112. DOI: 10.1103/PhysRevB.86.224112.

[76] P. Stefanovic, M. Haataja, and N. Provatas. “Phase-Field Crystals with Elastic Interactions”. In: *Physical Review Letters* 96 (22 2006), p. 225504. DOI: 10.1103/PhysRevLett.96.225504.

[77] S. Majaniemi and M. Grant. “Dissipative phenomena and acoustic phonons in isothermal crystals: A density-functional theory study”. In: *Physical Review B* 75 (5 2007), p. 054301. DOI: 10.1103/PhysRevB.75.054301.

[78] K. Wang et al. “Exploring atomic mechanisms of microstructure evolutions in crystals under vacancy super- or undersaturation states by a kinetic amplitude-expanded phase-field-crystal approach”. In: *International Journal of Plasticity* 157 (2022), p. 103386. ISSN: 0749-6419. DOI: 10.1016/j.ijplas.2022.103386.

[79] H. Jones. “Splat cooling and metastable phases”. In: *Reports on Progress in Physics* 36.11 (1973), p. 1425. DOI: 10.1088/0034-4885/36/11/002.

[80] K. Gabrysiak et al. “Development and characterization of a metastable Al-Mn-Ce alloy produced by laser powder bed fusion”. In: *Additive Manufacturing Letters* 1 (2021), p. 100017. ISSN: 2772-3690. DOI: 10.1016/j.addlet.2021.100017.

[81] B. J. Siwick et al. “An atomic-level view of melting using femtosecond electron diffraction”. en. In: *Science* 302.5649 (2003), pp. 1382–1385.

[82] L. Waldecker et al. “Electron-Phonon Coupling and Energy Flow in a Simple Metal beyond the Two-Temperature Approximation”. In: *Physical Review X* 6 (2 2016), p. 021003. DOI: 10.1103/PhysRevX.6.021003.

[83] V. Zhakhovsky et al. “Shock-induced melting and crystallization in titanium irradiated by ultrashort laser pulse”. In: *arXiv preprint arXiv:2306.09100* (2023).

[84] M. M. Budzevich et al. “Evolution of Shock-Induced Orientation-Dependent Metastable States in Crystalline Aluminum”. In: *Physical Review Letters* 109 (12 2012), p. 125505. DOI: 10.1103/PhysRevLett.109.125505.

[85] P. P. Shukla, P. T. Swanson, and C. J. Page. “Laser shock peening and mechanical shot peening processes applicable for the surface treatment of technical grade ceramics: A review”. In: *Proceedings of the Institution of Mechanical Engineers, Part B: Journal of Engineering Manufacture* 228.5 (2014), pp. 639–652.

[86] B. Dhakal and S. Swaroop. “Effect of laser shock peening on mechanical and microstructural aspects of 6061-T6 aluminum alloy”. In: *Journal of Materials Processing Technology* 282 (2020), p. 116640.

[87] X. Pan et al. “Plastic deformation behavior of titanium alloy by warm laser shock peening: Microstructure evolution and mechanical properties”. In: *Surface and Coatings Technology* 405 (2021), p. 126670.

[88] Y. F. Ye et al. “High-entropy alloy: challenges and prospects”. In: *Materials Today* 19.6 (2016), pp. 349–362.

[89] E. P. George, D. Raabe, and R. O. Ritchie. “High-entropy alloys”. In: *Nature Reviews Materials* 4.8 (2019), pp. 515–534.

[90] N. Ofori-Opoku et al. “Multicomponent phase-field crystal model for structural transformations in metal alloys”. In: *Physical Review B* 87 (13 2013), p. 134105. DOI: 10.1103/PhysRevB.87.134105.

[91] J. Berry and M. Grant. “Phase-field-crystal modeling of glass-forming liquids: Spanning time scales during vitrification, aging, and deformation”. In: *Physical Review E* 89 (6 2014), p. 062303. DOI: 10.1103/PhysRevE.89.062303.

[92] V. Fallah et al. “Phase-field crystal modeling of early stage clustering and precipitation in metal alloys”. In: *Physical Review B* 86 (13 2012), p. 134112.

[93] V. Fallah et al. “Simulation of early-stage clustering in ternary metal alloys using the phase-field crystal method”. In: *Acta Materialia* 61.10 (2013), pp. 3653–3666.

[94] A. P. Sutton and R. W. Balluffi. *Interfaces in Crystalline Materials*. Monographs on the physics and chemistry of materials. Clarendon Press, 1995. ISBN: 9780198513858.

[95] A. Skaugen, L. Angheluta, and J. Viñals. “Separation of Elastic and Plastic Timescales in a Phase Field Crystal Model”. In: *Physical Review Letters* 121 (25 2018), p. 255501.

[96] Y. Guo et al. “Strain mapping in nanocrystalline grains simulated by phase field crystal model”. In: *Philosophical Magazine* 95.9 (2015), pp. 973–984.

[97] Z.Y. Liu et al. “A nanoscale study of nucleation and propagation of Zener types cracks at dislocations: Phase field crystal model”. In: *Computational Materials Science* 179 (2020), p. 109640.

[98] H. Hallberg and K. Hult Blixt. “Evaluation of Nanoscale Deformation Fields from Phase Field Crystal Simulations”. In: *Metals* 12.10 (2022), p. 1630.

[99] H. Fan et al. “Strain rate dependency of dislocation plasticity”. In: *Nature Communications* 12.1 (2021), p. 1845.

[100] J. S. Langer, E. Bouchbinder, and T. Lookman. “Thermodynamic theory of dislocation-mediated plasticity”. In: *Acta Materialia* 58.10 (2010), pp. 3718–3732.

[101] A. Zippelius, B. I. Halperin, and D. R. Nelson. “Dynamics of two-dimensional melting”. In: *Physical Review B* 22 (5 1980), pp. 2514–2541.

[102] J. Berry et al. “Phase field crystal modeling as a unified atomistic approach to defect dynamics”. In: *Physical Review B* 89 (21 2014), p. 214117. DOI: 10.1103/PhysRevB.89.214117.

[103] D. G. Cahill et al. “Nanoscale thermal transport”. In: *Journal of Applied Physics* 93.2 (2002), pp. 793–818. ISSN: 0021-8979. DOI: 10.1063/1.1524305.

[104] S. Gelin, H. Tanaka, and A. Lemaître. “Anomalous phonon scattering and elastic correlations in amorphous solids”. In: *Nature Materials* 15.11 (2016), pp. 1177–1181.

[105] M. Baggioli and A. Zaccone. "Unified theory of vibrational spectra in hard amorphous materials". In: *Physical Review Research* 2 (1 2020), p. 013267. DOI: 10.1103/PhysRevResearch.2.013267.

[106] V. Heinonen et al. "Consistent Hydrodynamics for Phase Field Crystals". In: *Physical Review Letters* 116 (2 2016), p. 024303.

[107] M. Hillert, M. Schwind, and M. Selleby. "Trapping of vacancies by rapid solidification". In: *Acta Materialia* 50.12 (2002), pp. 3285–3293. ISSN: 1359-6454. DOI: 10.1016/S1359-6454(02)00150-7.

[108] T. Pinomaa et al. "Multiscale analysis of crystalline defect formation in rapid solidification of pure aluminium and aluminium–copper alloys". In: *Philosophical Transactions of the Royal Society A: Mathematical, Physical and Engineering Sciences* 380.2217 (2022), p. 20200319. DOI: 10.1098/rsta.2020.0319.

[109] H. Zhang et al. "Grain boundaries exhibit the dynamics of glass-forming liquids". In: *Proceedings of the National Academy of Sciences of the United States of America* 106 (16 2009), p. 77357740. DOI: 10.1073/pnas.0900227106.

[110] Y. Wang et al. "Disentangling boson peaks and Van Hove singularities in a model glass". In: *Physical Review B* 98 (17 2018), p. 174207. DOI: 10.1103/PhysRevB.98.174207.

[111] L. Waldecker, R. Bertoni, and R. Ernstorfer. "Compact femtosecond electron diffractometer with 100 keV electron bunches approaching the single-electron pulse duration limit". In: *Journal of Applied Physics* 117.4 (2015), p. 044903. ISSN: 0021-8979. DOI: 10.1063/1.4906786.

[112] C. Sagui, D. S. O'Gorman, and M. Grant. "Nucleation and growth: Decay of a metastable state". In: *Physical Review E* 56 (1 1997), R21–R24. DOI: 10.1103/PhysRevE.56.R21.

[113] S. Gao et al. “Recrystallization-based grain boundary engineering of 316L stainless steel produced via selective laser melting”. In: *Acta Materialia* 200 (2020), pp. 366–377. ISSN: 1359-6454. DOI: 10.1016/j.actamat.2020.09.015.

[114] S. F. Medina. “Determination of precipitation–time–temperature (PTT) diagrams for Nb, Ti or V micro-alloyed steels”. In: *Journal of Materials Science* 32.6 (1997), pp. 1487–1492. ISSN: 1573-4803. DOI: 10.1023/A:1018562202876.

[115] P. Shewmon. “Thermal Diffusion of Vacancies in Zinc”. In: *The Journal of Chemical Physics* 29.5 (2004), pp. 1032–1036. ISSN: 0021-9606. DOI: 10.1063/1.1744650.

[116] R. Chen et al. “Effect of cooling rate on solidification parameters and microstructure of Al-7Si-0.3Mg-0.15Fe alloy”. In: *Transactions of Nonferrous Metals Society of China* 24.6 (2014), pp. 1645–1652.

[117] J. S. Langer. “Thermal effects in dislocation theory”. In: *Physical Review E* 94 (6 2016), p. 063004. DOI: 10.1103/PhysRevE.94.063004.

[118] G. Kocher and N. Provatas. “Thermodensity coupling in phase-field-crystal-type models for the study of rapid crystallization”. In: *Physical Review Materials* 3 (5 2019), p. 053804. DOI: 10.1103/PhysRevMaterials.3.053804.

[119] C. Wang and M. S. Wise. “A Thermodynamically-Consistent Phase Field Crystal Model of Solidification with Heat Flux”. In: *Journal of Mathematical Study* 55.4 (2022), pp. 337–357. ISSN: 2617-8702. DOI: https://doi.org/10.4208/jms.v55n4.22.01.

[120] M. Punke et al. “Explicit temperature coupling in phase-field crystal models of solidification”. In: *Modelling Simulation Material Science and Engineering* 30 (6 2022), p. 074004. DOI: 10.1088/1361-651X/ac8abd.

[121] A.T. Dinsdale. “SGTE data for pure elements”. In: *Calphad* 15.4 (1991), pp. 317–425. ISSN: 0364-5916. DOI: 10.1016/0364-5916(91)90030-N.

[122] R. Ravelo et al. “Shock-induced plasticity in tantalum single crystals: Interatomic potentials and large-scale molecular-dynamics simulations”. In: *Physical Review B* 88 (13 2013), p. 134101. DOI: 10.1103/PhysRevB.88.134101.

[123] M. J. Frick, N. Ofori-Opoku, and N. Provatas. “Incorporating density jumps and species-conserving dynamics in XPFC binary alloys”. In: *Physical Review Materials* 4 (8 2020), p. 083404. DOI: 10.1103/PhysRevMaterials.4.083404.

[124] J. Xu et al. “The recalescence rate of cooling curve for undercooled solidification”. In: *Scientific Reports* 10.1 (2020), p. 1380. ISSN: 2045-2322. DOI: 10.1038/s41598-019-56079-6.

[125] B. H. Christensen, K. Vestentoft, and P. Balling. “Short-pulse ablation rates and the two-temperature model”. In: *Applied Surface Science* 253.15 (2007), pp. 6347–6352.

[126] Z. Chen et al. “Phase-field crystal simulation facet and branch crystal growth”. In: *Applied Physics A* 124.5 (2018), p. 385. ISSN: 1432-0630. DOI: 10.1007/s00339-018-1800-5.

[127] Z. Wang et al. “Minimal phase-field crystal modeling of vapor-liquid-solid coexistence and transitions”. In: *Physical Review Materials* 4 (10 2020), p. 103802. DOI: 10.1103/PhysRevMaterials.4.103802.

[128] P. Stefanovic, M. Haataja, and N. Provatas. “Phase field crystal study of deformation and plasticity in nanocrystalline materials”. In: *Physical Review E* 80 (4 2009), p. 046107. DOI: 10.1103/PhysRevE.80.046107.

[129] S. Abdalla et al. “Thermodynamics, formation dynamics, and structural correlations in the bulk amorphous phase of the phase-field crystal model”. In: *The Journal of Chemical Physics* 157.16 (2022). 164502. ISSN: 0021-9606. DOI: 10.1063/5.0114705.

[130] M. Vasin and V. Ankudinov. “Competition of glass and crystal: Phase-field model”. In: *Mathematical Methods in the Applied Sciences* n/a.n/a (2023). DOI: https://doi.org/10.1002/mma.9207.

[131] J. Berry, K. R. Elder, and M. Grant. “Melting at dislocations and grain boundaries: A phase field crystal study”. In: *Physical Review B* 77 (22 2008), p. 224114. DOI: 10.1103/PhysRevB.77.224114.

[132] J. Berry and M. Grant. “Modeling Multiple Time Scales during Glass Formation with Phase-Field Crystals”. In: *Physical Review Letters* 106 (17 2011), p. 175702. DOI: 10.1103/PhysRevLett.106.175702.

[133] D Ponge and G. Gottstein. “Necklace formation during dynamic recrystallization: mechanisms and impact on flow behavior”. In: *Acta Materialia* 46.1 (1998), pp. 69–80. ISSN: 1359-6454. DOI: https://doi.org/10.1016/S1359-6454(97)00233-4.

[134] B. Golding and J. E. Graebner. “Echo Phenomena in Disordered Solids”. In: *Phonon Scattering in Condensed Matter*. Ed. by H. J. Maris. Boston, MA: Springer US, 1980, pp. 11–20. ISBN: 978-1-4613-3063-9. DOI: 10.1007/978-1-4613-3063-9_2.

[135] N. Ofori-Opoku et al. “Multicomponent phase-field crystal model for structural transformations in metal alloys”. In: *Physical Review B* 87 (13 2013), p. 134105. DOI: 10.1103/PhysRevB.87.134105.

[136] “Phase Field Crystal Modeling of Pure Materials”. In: *Phase-Field Methods in Materials Science and Engineering*. John Wiley & Sons, Ltd, 2010. Chap. 8, pp. 167–208. ISBN: 9783527631520. DOI: https://doi.org/10.1002/9F783527631520.ch8.

[137] “Phase Field Crystal Modeling of Binary Alloys”. In: *Phase-Field Methods in Materials Science and Engineering*. John Wiley & Sons, Ltd, 2010. Chap. 9, pp. 209–222. ISBN: 9783527631520. DOI: https://doi.org/10.1002/9783527631520.ch9.

[138] X. Pan et al. “Effect of dynamic recrystallization on texture orientation and grain refinement of Ti6Al4V titanium alloy subjected to laser shock peening”. In: *Journal of Alloys and Compounds* 850 (2021), p. 156672. ISSN: 0925-8388. DOI: 10.1016/j.jallcom.2020.156672.

[139] K.N. Amato et al. “Microstructures and mechanical behavior of Inconel 718 fabricated by selective laser melting”. In: *Acta Materialia* 60.5 (2012), pp. 2229–2239. ISSN: 1359-6454. DOI: 10.1016/j.actamat.2011.12.032.

[140] C. M. Sellars and J. A. Whiteman. “Recrystallization and grain growth in hot rolling”. In: *Metal Science* 13.3-4 (1979), pp. 187–194. DOI: 10.1179/msc.1979.13.3-4.187.

[141] D. Wang et al. “Cracking in laser additively manufactured W: Initiation mechanism and a suppression approach by alloying”. In: *Materials & Design* 162 (2019), pp. 384–393. ISSN: 0264-1275. DOI: 10.1016/j.matdes.2018.12.010.

[142] F. C. Pinto et al. “Recrystallization in non-conventional microstructures of 316L stainless steel produced via laser powder-bed fusion: effect of particle coarsening kinetics”. In: *Journal of Materials Science* 57 (27 2022), pp. 9576–9598. ISSN: 1573-4803. DOI: 10.1007/s10853-021-06859-1.

[143] S. Ren et al. “Boson-peak-like anomaly caused by transverse phonon softening in strain glass”. In: *Nature Communications* 12 (1 2021). ISSN: 2041-1723. DOI: 10.1038/s41467-021-26029-w.

[144] C. A. Angell et al. “Relaxation in glassforming liquids and amorphous solids”. In: *Journal of Applied Physics* 88.6 (2000), pp. 3113–3157. ISSN: 0021-8979. DOI: 10.1063/1.1286035.

[145] A. Zaccone and M. Baggioli. “Erratum: Unified theory of vibrational spectra in hard amorphous materials [Phys. Rev. Research 2, 013267 (2020)]”. In: *Physical Review Research* 4 (2 2022), 029001(E). DOI: 10.1103/PhysRevResearch.4.029001.

[146] S. L. Seyler and C. E. Seyler. “Molecular hydrodynamic theory of the velocity autocorrelation function”. In: *The Journal of Chemical Physics* 159.5 (2023), p. 054108. ISSN: 0021-9606. DOI: 10.1063/5.0153649.

[147] S. N. Taraskin et al. “Origin of the Boson Peak in Systems with Lattice Disorder”. In: *Physical Review Letters* 86 (7 2001), pp. 1255–1258. DOI: 10.1103/PhysRevLett.86.1255.

[148] M. González-Jiménez et al. “Understanding the emergence of the boson peak in molecular glasses”. In: *Nature Communications* 14.1 (2023), p. 215. ISSN: 2041-1723. DOI: 10.1038/s41467-023-35878-6.

[149] F.J. Humphreys and M. Hatherly. “Chapter 4 - The Structure and Energy of Grain Boundaries”. In: *Recrystallization and Related Annealing Phenomena (Second Edition)*. Ed. by F.J. Humphreys and M. Hatherly. Second Edition. Oxford: Elsevier, 2004, pp. 91–119. ISBN: 978-0-08-044164-1. DOI: 10.1016/B978-008044164-1/50008-6.

[150] J. Narayan et al. “Explosive recrystallization during pulsed laser irradiation”. In: *Journal of Vacuum Science & Technology A* 2.4 (1984), pp. 1495–1497. DOI: 10.1116/1.572390.

[151] F. Demmel. “Slow structural relaxation process facilitates solidification in liquid gallium”. In: *Physical Review B* 101 (1 2020), p. 014207. DOI: 10.1103/PhysRevB.101.014207.

[152] U. Andrade et al. “Dynamic recrystallization in high-strain, high-strain-rate plastic deformation of copper”. In: *Acta Metallurgica et Materialia* 42.9 (1994), pp. 3183–3195. ISSN: 0956-7151. DOI: 10.1016/0956-7151(94)90417-0.

[153] M. I. Arefev, M. V. Shugaev, and L. V. Zhigilei. “Kinetics of laser-induced melting of thin gold film: How slow can it get?” In: *Science Advances* 8.38 (2022), eabo2621. DOI: 10.1126/sciadv.abo2621.

[154] Y. M. Beltukov et al. “Boson peak and Ioffe-Regel criterion in amorphous siliconlike materials: The effect of bond directionality”. In: *Physical Review E* 93 (2 2016), p. 023006. DOI: 10.1103/PhysRevE.93.023006.

[155] See Supplemental Material at Supplemental for a set of simulation videos.

[156] R.N. Singh, S. Arafin, and A.K. George. “Temperature-dependent thermo-elastic properties of s-, p- and d-block liquid metals”. In: *Physica B: Condensed Matter* 387.1 (2007), pp. 344–351. ISSN: 0921-4526. DOI: 10.1016/j.physb.2006.04.029.

[157] Y. Kraftmakher. “Equilibrium vacancies and thermophysical properties of metals”. In: *Physics Reports* 299.2 (1998), pp. 79–188. ISSN: 0370-1573. DOI: 10.1016/S0370-1573(97)00082-3.

[158] A. Karma and A. Sarkissian. “Interface dynamics and banding in rapid solidification”. In: *Physical Review E* 47 (1 1993), pp. 513–533. DOI: 10.1103/PhysRevE.47.513.

[159] T. Pinomaa, A. Laukkanen, and N. Provatas. “Solute trapping in rapid solidification”. In: *MRS Bulletin* 45.11 (2020), 910–915. DOI: 10.1557/mrs.2020.274.

[160] K. R. Elder et al. “Sharp interface limits of phase-field models”. In: *Physical Review E* 64 (2 2001), p. 021604. DOI: 10.1103/PhysRevE.64.021604.

[161] R. F. Sekerka. “Morphology: from sharp interface to phase field models”. In: *Journal of Crystal Growth* 264.4 (2004). Proceedings of the Symposium - Progress in Crystal Growth, pp. 530–540. ISSN: 0022-0248. DOI: https://doi.org/10.1016/j.jcrysgro.2003.12.033.

[162] P. K. Galenko et al. “Solute trapping in rapid solidification of a binary dilute system: A phase-field study”. In: *Physical Review E* 84 (4 2011), p. 041143. DOI: 10.1103/PhysRevE.84.041143.

[163] B. I. Halperin and David R. Nelson. “Theory of Two-Dimensional Melting”. In: *Physical Review Letters* 41 (2 1978), pp. 121–124. DOI: 10.1103/PhysRevLett.41.121.

[164] R.A Swalin and C.A Yin. “Thermal diffusion of vacancies in aluminum”. In: *Acta Metallurgica* 15.2 (1967), pp. 245–248. ISSN: 0001-6160. DOI: https://doi.org/10.1016/0001-6160(67)90198-8.

[165] C. Cohen, P. D. Fleming, and J. H. Gibbs. “Hydrodynamics of amorphous solids with application to the light-scattering spectrum”. In: *Physical Review B* 13 (2 1976), pp. 866–877. DOI: 10.1103/PhysRevB.13.866.

[166] "Phase Field Crystal Modeling of Pure Materials". In: *Phase-Field Methods in Materials Science and Engineering*. John Wiley & Sons, Ltd, 2010. Chap. 8, pp. 167–208. ISBN: 9783527631520. DOI: https://doi.org/10.1002/9783527631520.ch8.

[167] "Phase Field Crystal Modeling of Binary Alloys". In: *Phase-Field Methods in Materials Science and Engineering*. John Wiley & Sons, Ltd, 2010. Chap. 9, pp. 209–222. ISBN: 9783527631520. DOI: https://doi.org/10.1002/9783527631520.ch9. eprint: https://onlinelibrary.wiley.com/doi/pdf/10.1002/9783527631520.ch9.

[168] "Appendix B: Basic Numerical Algorithms for Phase Field Equations". In: *Phase-Field Methods in Materials Science and Engineering*. John Wiley & Sons, Ltd, 2010, pp. 261–285. ISBN: 9783527631520. DOI: https://doi.org/10.1002/9783527631520.app2.

[169] N. Provatas, T. Pinomaa, and N. Ofori-Opoku. CRC Press, 2021. DOI: https://doi.org/10.1201/9781003204312.

[170] L. Yang et al. "Role of Remelting in Grain Refinement of Undercooled Single-Phase Alloys". In: *Metallurgical and Materials Transactions A* 53.8 (2022), pp. 3100–3109. ISSN: 1543-1940. DOI: 10.1007/s11661-022-06730-1.

[171] J.A. Dantzig and M. Rappaz. *Solidification: 2nd Edition - Revised & Expanded*. Engineering Sciences. CRC Press LLC, 2016. ISBN: 9782940222971.

[172] J.P. Stark. "Vacancy concentrations in single crystal thermal diffusion experiments". In: *Scripta Metallurgica* 5.9 (1971), pp. 727–732. ISSN: 0036-9748. DOI: https://doi.org/10.1016/0036-9748(71)90153-0.

[173] T. Koyama and Y. Tsukada. "Ludwig–Soret effect formulated from the grain-boundary-phase model". In: *Calphad* 73 (2021), p. 102269. ISSN: 0364-5916. DOI: https://doi.org/10.1016/j.calphad.2021.102269.

[174] A. Hellouin de Menibus et al. “Formation and characterization of hydride blisters in Zircaloy-4 cladding tubes”. In: *Journal of Nuclear Materials* 449.1 (2014), pp. 132–147. ISSN: 0022-3115. DOI: https://doi.org/10.1016/j.jnucmat.2014.03.006.

[175] M. Salvalaglio and K. R. Elder. “Coarse-grained modeling of crystals by the amplitude expansion of the phase-field crystal model: an overview”. In: *Modelling Simulation Material Science and Engineering* 30 (5 2022), p. 053001. DOI: 10.1088/1361-651X/ac681e.

[176] H. Emmerich et al. “Phase-field-crystal models for condensed matter dynamics on atomic length and diffusive time scales: an overview”. In: *Advances in Physics* 61.6 (2012), pp. 665–743. DOI: 10.1080/00018732.2012.737555.

[177] G. Deffrennes and B. Oudot. “A self-consistent model to describe the temperature dependence of the bulk modulus, thermal expansion and molar volume compatible with 3rd generation CALPHAD databases”. In: *Calphad* 74 (2021), p. 102291. ISSN: 0364-5916. DOI: https://doi.org/10.1016/j.calphad.2021.102291.

[178] J.L. Tallon and A. Wolfenden. “Temperature dependence of the elastic constants of aluminum”. In: *Journal of Physics and Chemistry of Solids* 40.11 (1979), pp. 831–837. ISSN: 0022-3697. DOI: https://doi.org/10.1016/0022-3697(79)90037-4.

[179] J. H. Perepezko and W. J. Boettinger. “Use of Metastable Phase Diagrams in Rapid Solidification”. In: *MRS Online Proceedings Library (OPL)* 19 (1982), p. 223. DOI: 10.1557/PROC-19-223.

[180] M. Golizadeh et al. “Rapid solidification and metastable phase formation during surface modifications of composite Al-Cr cathodes exposed to cathodic arc plasma”. In: *Journal of Materials Science & Technology* 94 (2021), pp. 147–163. ISSN: 1005-0302. DOI: https://doi.org/10.1016/j.jmst.2021.03.059.

[181] K.G. Prashanth and J. Eckert. “Formation of metastable cellular microstructures in selective laser melted alloys”. In: *Journal of Alloys and Compounds* 707 (2017). Selected papers presented at ISMANAM 2016, July 3rd-8th, Nara, Japan, pp. 27–34. ISSN: 0925-8388. DOI: https://doi.org/10.1016/j.jallcom.2016.12.209.

[182] M.J. Konstantinović. “Internal friction study of dislocation dynamics in neutron irradiated iron, and iron–copper alloys”. In: *Journal of Nuclear Materials* 395.1 (2009), pp. 75–78. ISSN: 0022-3115. DOI: https://doi.org/10.1016/j.jnucmat.2009.09.020.

[183] H. Tan and T. J. Ahrens. “Shock temperature measurements for metals”. In: *High Pressure Research* 2.3 (1990), pp. 159–182. DOI: 10.1080/08957959008201036.

[184] E. Gruneisen. “Theorie des festen Zustandes einatomiger Elemente”. In: *Annalen der Physik* 344.12 (1912), pp. 257–306. DOI: https://doi.org/10.1002/andp.19123441202. eprint: https://onlinelibrary.wiley.com/doi/pdf/10.1002/andp.19123441202.

[185] J. J. Gilvarry. “Temperature-Dependent Equations of State of Solids”. In: *Journal of Applied Physics* 28.11 (2004), pp. 1253–1261. ISSN: 0021-8979. DOI: 10.1063/1.1722628.

[186] V. Skogvoll et al. In: ().

[187] J. P. Hansen and L. Verlet. “Phase Transitions of the Lennard-Jones System”. In: *Physical Review* 184 (1 1969), pp. 151–161.

[188] A. Yamanaka, K. McReynolds, and P. W. Voorhees. “Phase field crystal simulation of grain boundary motion, grain rotation and dislocation reactions in a BCC bicrystal”. In: *Acta Materialia* 133 (2017), pp. 160–171.

[189] S. Fujii et al. “Quantitative prediction of grain boundary thermal conductivities from local atomic environments”. In: *Nature Communications* 11.1 (2020), p. 1854.

[190] S. Chandra, M. K. Samal, and V.M. Chavan. “Dislocation nucleation from damaged grain boundaries in face centered cubic metals – An atomistic study”. In: *Materialia* 8 (2019), p. 100497.

[191] T. Zhu et al. “Temperature and Strain-Rate Dependence of Surface Dislocation Nucleation”. In: *Physical Review Letters* 100 (2 2008), p. 025502.

[192] A. M. Lindenberg et al. “Time-Resolved X-Ray Diffraction from Coherent Phonons during a Laser-Induced Phase Transition”. In: *Physical Review Letters* 84 (1 2000), pp. 111–114.

[193] J. Em-Udom and N. Pisutha-Arnond. “Prediction of mechanical-hysteresis behavior and complex moduli using the phase field crystal method with modified pressure controlled dynamic equation”. In: *Materials Research Express* 7.1 (2020), p. 015326. DOI: 10.1088/2053-1591/ab611f.

[194] A. Skaugen, L. Angheluta, and J. Viñals. “Dislocation dynamics and crystal plasticity in the phase-field crystal model”. In: *Physical Review B* 97 (5 2018), p. 054113.

[195] J Bueno et al. “Three dimensional structures predicted by the modified phase field crystal equation”. In: *Computational Materials Science* 111 (2016), pp. 310–312.

[196] M. Salvalaglio et al. In: ().

[197] C. L. Kelchner, S. J. Plimpton, and J. C. Hamilton. “Dislocation nucleation and defect structure during surface indentation”. In: *Physical Review B* 58 (17 1998), pp. 11085–11088.

[198] R. E. Rudd and J. F. Belak. “Void nucleation and associated plasticity in dynamic fracture of polycrystalline copper: an atomistic simulation”. In: *Computational Materials Science* 24.1 (2002), pp. 148–153.

[199] X. Li and S. Lee. “Role of hydrodynamic viscosity on phonon transport in suspended graphene”. In: *Physical Review B* 97 (9 2018), p. 094309.

[200] K. R. Elder, Z. Huang, and N. Provatas. “Amplitude expansion of the binary phase-field-crystal model”. In: *Physical Review E* 81 (1 2010), p. 011602.

[201] S. Chandrasekhar. “Stochastic Problems in Physics and Astronomy”. In: *Review Modern Physics* 15 (1 1943), pp. 1–89.

[202] G. Kocher and N. Provatas. “New Density Functional Approach for Solid-Liquid-Vapor Transitions in Pure Materials”. In: *Physical Review Letters* 114 (15 2015), p. 155501.

[203] M. Seymour and N. Provatas. “Structural phase field crystal approach for modeling graphene and other two-dimensional structures”. In: *Physical Review B* 93 (3 2016), p. 035447.

[204] S. Kim et al. “Phonon scattering during dislocation motion inducing stress-drop in cubic metals”. In: *Acta Materialia* 115 (2016), pp. 143–154.

[205] D. Tanguy et al. “Dislocation nucleation induced by a shock wave in a perfect crystal: Molecular dynamics simulations and elastic calculations”. In: *Physical Review B* 68 (14 2003), p. 144111.

[206] C. E. Wehrenberg et al. “In situ X-ray diffraction measurement of shock-wave-driven twinning and lattice dynamics”. In: *Nature* 550.7677 (2017), pp. 496–499.

[207] G. E. Duvall and R. A. Graham. “Phase transitions under shock-wave loading”. In: *Review Modern Physics* 49 (3 1977), pp. 523–579.

[208] J. M. Häring et al. “Coarse-grained density and compressibility of nonideal crystals: General theory and an application to cluster crystals”. In: *Physical Review B* 92 (18 2015), p. 184103.

[209] S. Majaniemi, M. Nonomura, and M. Grant. “First-principles and phenomenological theories of hydrodynamics of solids”. In: *The European Physical Journal B* 66.3 (2008), pp. 329–335.

[210] C. Zener and J. H. Hollomon. “Effect of Strain Rate Upon Plastic Flow of Steel”. In: *Journal of Applied Physics* 15.1 (2004), pp. 22–32. ISSN: 0021-8979. DOI: 10.1063/1.1707363.

[211] A. Akhiezer. “On the Absorption of Sound in Solids”. In: *Journal of Physics (Moscow)* 1.1 (1939), pp. 277–287.

[212] W. P. Mason. “Phonon Viscosity and Its Effect on Acoustic Wave Attenuation and Dislocation Motion”. In: *The Journal of the Acoustical Society of America* 32.4 (2005), pp. 458–472. ISSN: 0001-4966. DOI: 10.1121/1.1908099.

[213] A. Moriel et al. “Wave attenuation in glasses: Rayleigh and generalized-Rayleigh scattering scaling”. In: *The Journal of Chemical Physics* 151.10 (2019), p. 104503. ISSN: 0021-9606. DOI: 10.1063/1.5111192.

[214] M. J. Hÿtch, E. Snoeck, and R. Kilaas. “Quantitative measurement of displacement and strain fields from HREM micrographs”. In: *Ultramicroscopy* 74.3 (1998), pp. 131–146.

[215] J.L. Rouvière and E. Sarigiannidou. “Theoretical discussions on the geometrical phase analysis”. In: *Ultramicroscopy* 106.1 (2005), pp. 1–17.

[216] T. Ungár. “Microstructural parameters from X-ray diffraction peak broadening”. In: *Scripta Materialia* 51.8 (2004), pp. 777–781.

[217] I. Groma, T. Ungár, and M. Wilkens. “Asymmetric X-ray line broadening of plastically deformed crystals. I. Theory”. In: *Journal of Applied Crystallography* 21.1 (1988), pp. 47–54. DOI: https://doi.org/10.1107/S0021889887009178.

[218] I. Groma and G. Monnet. “Analysis of asymmetric broadening of X-ray diffraction peak profiles caused by randomly distributed polarized dislocation dipoles and dislocation walls”. In: *Journal of Applied Crystallography* 35.5 (2002), pp. 589–593. DOI: https://doi.org/10.1107/S0021889802010695.

[219] B.E. Warren. “X-ray studies of deformed metals”. In: *Progress in Metal Physics* 8 (1959), pp. 147–202.

[220] P. Galenko, D. Danilov, and V. Lebedev. “Phase-field-crystal and Swift-Hohenberg equations with fast dynamics”. In: *Physical Review E* 79 (5 2009), p. 051110.

[221] V. Ankudinov et al. “Correlated noise effect on the structure formation in the phase-field crystal model”. In: *Mathematical Methods in the Applied Sciences* 44.16 (2021), pp. 12185–12193. DOI: https://doi.org/10.1002/mma.6887.

[222] M. Baggioli et al. “Gapped momentum states”. In: *Physics Reports* 865 (2020), pp. 1–44.

[223] W. W. Pang et al. “Dislocation creation and void nucleation in FCC ductile metals under tensile loading: A general microscopic picture”. In: *Scientific Reports* 4.1 (2014), p. 6981.

[224] R. M. Khusnutdinoff et al. “Collective modes and gapped momentum states in liquid Ga: Experiment, theory, and simulation”. In: *Physical Review B* 101 (21 2020), p. 214312.

[225] L. Jörgenson et al. “Early-time regime for interfacial instabilities in a kinetic Ising model”. In: *Physical Review E* 48 (6 1993), pp. 4592–4598.

[226] P. K. Galenko et al. “Thermodynamics of rapid solidification and crystal growth kinetics in glass-forming alloys”. In: *Philosophical Transactions of the Royal Society A: Mathematical, Physical and Engineering Sciences* 377.2143 (2019), p. 20180205.

[227] F. Hadadifard, S. Malhi, and Z. Xiao. “A class of Finite difference Methods for solving inhomogeneous damped wave equations”. In: *arXiv preprint arXiv:2008.08043* (2020).

[228] C. Moler and C. Van Loan. “Nineteen dubious ways to compute the exponential of a matrix, twenty-five years later”. In: *SIAM review* 45.1 (2003), pp. 3–49.

[229] A. H. Al-Mohy and N. J. Higham. “Computing the action of the matrix exponential, with an application to exponential integrators”. In: *SIAM journal on scientific computing* 33.2 (2011), pp. 488–511.

[230] L. Q. Chen and J. Shen. “Applications of semi-implicit Fourier-spectral method to phase field equations”. In: *Computer Physics Communications* 108.2-3 (1998), pp. 147–158.

[231] W. Zhou et al. “Mechanical relaxation and fracture of phase field crystals”. In: *Physical Review E* 99.1 (2019), p. 013302.

[232] P. C. Hohenberg and B. I. Halperin. “Theory of dynamic critical phenomena”. In: *Review Modern Physics* 49 (3 1977), pp. 435–479. DOI: 10.1103/RevModPhys.49.435.

[233] G. Caginalp. “Stefan and Hele-Shaw type models as asymptotic limits of the phase-field equations”. In: *Physical Review A* 39 (11 1989), pp. 5887–5896. DOI: 10.1103/PhysRevA.39.5887.

[234] P. Jreidini et al. “Orientation Gradients in Rapidly Solidified Pure Aluminum Thin Films: Comparison of Experiments and Phase-Field Crystal Simulations”. In: *Physical Review Letters* 127 (20 2021), p. 205701. DOI: 10.1103/PhysRevLett.127.205701.

[235] G. Caginalp and X. Chen. “Convergence of the phase field model to its sharp interface limits”. In: *European Journal of Applied Mathematics* 9.4 (1998), 417–445. DOI: 10.1017/S0956792598003520.

[236] N. Wang, K. H. Bevan, and N. Provatas. “Phase-Field-Crystal Model for Electromigration in Metal Interconnects”. In: *Physical Review Letters* 117 (15 2016), p. 155901. DOI: 10.1103/PhysRevLett.117.155901.